

**Investigation of Cherenkov emission with applications in  
dosimetry, image guidance and intensity modulation in  
radiation therapy**

Yana Zlateva

Degree of Master of Science in Medical Physics

Medical Physics Unit - Department of Oncology - Faculty of Medicine

McGill University

Montreal, Quebec, Canada

December 2013

A thesis submitted to McGill University in partial fulfillment of the requirements  
of the degree of Master of Science in Medical Physics

© Yana Zlateva 2013



*To my best friend, Andrew Ward*

## ACKNOWLEDGEMENTS

This work has been made possible with the help and support of many of my colleagues, fellow researchers and friends. I would like to take this opportunity to thank everyone who has contributed to the success of my M.Sc. thesis.

First and foremost, I would like to thank my supervisor, Dr. Issam El Naqa, whose unconditional encouragement and optimism, patience, and continued support made this work a success.

I would also like to express my utmost gratitude to Dr. Nathaniel Quitariano of the McGill University Department of Mining and Materials Engineering for his collaboration on this project and for providing me with much needed materials engineering knowledge so critical to my success.

I would like to express my gratitude to Joe Larkin of the McGill University Health Centre (MUHC) for offering invaluable support and advice during the construction and testing of the optical measurement setup and for constructing and providing many parts of the setup, to Michael Evans of the MUHC and the McGill University Medical Physics Unit (MPU) for training me and helping with experiments, to Dr. Norma Ybarra of the MPU for training me in biomedical lab techniques and for participating in phantom and quantum dot preparation, to Dr. Lawrence Chen of the McGill University Department of Electrical and Computer Engineering for teaching me about optical signal detection and instrumentation, to Daniel Grozdanov and fellow classmates Martin Vallières and Piotr Pater for advice on the abstract and for the French version of the abstract, to Dr. Arman Sarfehnia of the MUHC for training me in ion chamber measurements, to Jun Wang of the McGill University Department of Mining and Materials Engineering for providing the quantum dots.

Many thanks to Sylvain Bossé of Delta Photonics for support with the optical instrumentation and to Michael Cate of NN-Labs for information about the quantum dots.

My sincere appreciation goes to Margery Knewstubb and Tatjana Nisic, the MPU research and administrative coordinators, for their wonderful work in taking care of administrative matters.

I would like to acknowledge NSERC and McGill University for their support in funding this work and making it possible.

I am immensely grateful to all the staff, clinical physicists, instructors, as well as all my fellow students at the McGill University Medical Physics Unit for their precious help, support and contribution to this work.

Last but not least, a very special thank you to my parents, Zlatko and Diana, my brother, Ogy, and my friends for their unconditional love, support and encouragement, and to Andrew Ward for helping me with measurements, for listening, and for helping me work through so many of the issues and obstacles I have encountered in my research and in my graduate training as a whole.

## ABSTRACT

The aims of this work are to validate the potential application of Cherenkov emission (CE) in radiotherapy dosimetry, online imaging and beam modulation by analysis of its correlation with radiation dose and by a spectral shift to the near-infrared (NIR) window of biological tissue in order to maximize its detection. This work makes an original contribution to scientific knowledge by effectively correlating radiation dose and CE in two dimensions, using an optical fiber and grating spectrometer, without need for a computer-generated spatially variant conversion factor or a fluorescent dye, and by successfully shifting CE to the NIR in a tissue-simulating phantom with the use of quantum dots (QDs), whose advantages over other fluorescent probes are the straightforward tunability of their physical and biochemical properties, photostability, narrow distinctive emission profile, and compatibility of their absorption profile with the CE spectrum.

Radiation dose was correlated with CE via both computer simulation and experimental measurements using clinical 6-18 MeV electron beams. A Monte Carlo (MC) CE simulator was designed using the Geant4 simulation toolkit. In order to maximize the signal, beam incidence angle was optimized through simulation and experiment and the feasibility of two-fiber detection was assessed. Phantoms used in the experiments were a water tank and a tissue-simulating phantom composed of water, Intralipid® and beef blood. The optical detection system consisted of a multi-mode step-index fiber optic cable (numerical aperture = 0.22 for dose versus Cherenkov studies), positioned out of the beam and connected to a single-channel diffraction grating spectrometer incorporating a front-illuminated or back-illuminated charge-coupled device (CCD). A cylindrical ionization chamber was used for dose measurements. CdSe/ZnS core-shell QDs, emitting at  $(650 \pm 10)$  nm, were used to achieve a NIR shift of the Cherenkov signal.

A preliminary software analysis indicated a strong correlation between radiation dose and CE with a Pearson correlation coefficient larger than 0.99. A beam incidence angle of  $50^\circ$  relative to the surface normal produced a CE

maximum along the horizontal fiber. An angle of  $47^\circ$  (corresponding to more than 80% of the maximum signal) was adopted in order to maximize the scan depth by avoiding beam perturbation due to setup components and fiber protrusion into the field. Dose versus CE correlation was investigated via water phantom ion chamber scans along the beam central axis and optical fiber scans with the fiber tip positioned at the field edge. With all data sets normalized to 1, the effective point of measurement of the optical system for 18, 12 and 6 MeV clinical electron beams was found to be at depths of approximately 1.7, 0.8, and 0.1 cm, respectively, downstream from the fiber axis, with a Pearson correlation coefficient for all (simulated and experimental) data larger than 0.99. CE by an 18 MeV electron beam was successfully shifted towards 650 nm in a water tank, confirming its capacity to stimulate CdSe/ZnS photoluminescence, and in a tissue-simulating phantom. Smaller field sizes and larger QD depths resulted in a lower signal, though a shift was still apparent for a 1 cm depth of the QDs. Statistical data analysis indicated no noise bias and that radiation might have impacted the spectrometer electronics.

The results of this work validate the potential for application of CE in radiotherapy dosimetry, online imaging and intensity modulation based on tumor microenvironment information, such as oxygenation, since CE is intrinsic to the beam, non-ionizing and can be detected outside the beam, and the QDs used for the experiments are photostable, tunable, and can be modified to incorporate molecular reporters. Future work involves the use of a multi-channel spectrometer for simultaneous collection of main, reference and background signals, incorporation of a lens or a single-mode fiber to reduce the sensitive volume, as well as development of better spectral data extraction techniques. It is expected that the proposed technique will be applicable to 3D dose mapping by means of diffuse optical tomography, online CE imaging and localization during radiotherapy, and beam modulation based on tumor microenvironment information.

## RÉSUMÉ

Les objectifs de cette étude sont de valider la potentielle application de l'émission Cherenkov (EC) pour la dosimétrie en radiothérapie, pour l'imagerie en temps réel et pour la modulation des faisceaux par l'analyse de sa corrélation avec la dose de rayonnement et par un décalage spectral vers la fenêtre infrarouge proche (FIP) des tissus biologiques afin de maximiser sa détection. Ce travail apporte une contribution originale aux travaux antérieurs en corrélant efficacement, d'une part, la dose de rayonnement et l'EC en 2 dimensions à l'aide d'une fibre optique et d'un spectromètre à réseau, et ce, sans l'aide d'un facteur de conversion variant spatialement et généré par ordinateur ou d'un colorant fluorescent, et d'autre part, en effectuant avec succès le déplacement de l'EC à la FIP dans un fantôme simulant les tissus biologiques grâce à l'utilisation de points quantiques (PQs). Les avantages par rapport à d'autres sondes fluorescentes sont les possibilités de réglages simples de leurs propriétés physiques et biochimiques, la photostabilité, un profil d'émission distinctif et étroit, et la compatibilité de leur profil d'absorption avec le spectre d'EC.

La dose de rayonnement a été corrélée avec l'EC à la fois par simulation informatique et par mesures expérimentales utilisant des faisceaux d'électrons cliniques de 6-18 MeV. Un simulateur Monte Carlo (MC) de l'EC a été conçu en utilisant la plateforme de simulation Geant4. Afin de maximiser le signal, l'angle d'incidence a été optimisé grâce à la simulation et aux procédures expérimentales, et la faisabilité de la détection par 2 fibres a été évaluée. Les fantômes utilisés dans les expériences consistaient d'un réservoir d'eau et d'un fantôme simulant les tissus biologiques composés d'eau, d'Intralipid® et de sang de boeuf. Le système de détection optique est composé d'un câble de fibre optique multi-mode à saut d'indice (ouverture numérique = 0.22 pour l'étude de corrélation de la dose avec l'EC), placé hors du faisceau d'électron et relié à un spectromètre à réseau de diffraction à canal unique comprenant un dispositif à couplage de charge éclairé par l'avant ou l'arrière. Une chambre d'ionisation cylindrique a été utilisée pour

les mesures de dose. Des points quantiques CdSe/ZnS, émettant à  $(650 \pm 10)$  nm, ont été utilisés afin de réaliser un décalage du signal Cherenkov vers la FIP.

Une analyse préliminaire a indiqué une forte corrélation entre la dose de rayonnement et de l'EC avec un coefficient de corrélation de Pearson supérieur à 0.99. Un angle d'incidence du faisceau de  $50^\circ$  par rapport à la normale à la surface a produit une EC maximale le long de la fibre horizontale. Un angle de  $47^\circ$  (correspondant à plus de 80% du signal maximal) a été adopté dans le but de maximiser la profondeur du scan en évitant la perturbation du faisceau par les composantes d'installation et l'avancée des fibres dans le champ. La corrélation de la dose en fonction de l'EC a été étudiée via des scans de la chambre d'ionisation dans le fantôme d'eau le long de l'axe central du faisceau ainsi que par des scans de fibre optique avec la pointe de la fibre positionnée sur le bord du champ du faisceau. Après normalisation, le point effectif de mesure du système optique des faisceaux d'électrons cliniques de 18, 12 et 6 MeV, s'est révélé être situé à des profondeurs respectives de 1.7, 0.8 et 0.1 cm, et ce, en aval de l'axe de la fibre, avec un coefficient de corrélation Pearson pour toutes les données (simulées et expérimentales) de plus de 0.99. La fenêtre d'EC d'un faisceau d'électrons de 18 MeV a été décalée avec succès vers 650 nm dans le réservoir d'eau, confirmant sa capacité à stimuler la photoluminescence de CdSe/ZnS, et dans le fantôme simulant les tissus biologiques. La diminution de la taille des champs ainsi que l'augmentation de la profondeur des PQs ont eu pour effet de diminuer le signal, quoiqu'un décalage du signal était encore apparent à 1 cm de profondeur. L'analyse statistique des données nous a confirmé que le bruit n'a pas d'impact significatif sur le signal, mais que le rayonnement peut avoir un impact sur les composantes électroniques du spectromètre.

Les résultats de ce travail confirment le potentiel d'application de l'EC pour la dosimétrie en radiothérapie, pour l'imagerie en temps réel et pour la modulation d'intensité des faisceaux en fonction des informations relatives au microenvironnement des tumeurs, comme l'oxygénation. En effet, l'EC est intrinsèque au faisceau d'électrons, est non-ionisante et peut être détectée en

dehors du faisceau. De plus, les PQs utilisés dans nos expériences sont photostables et peuvent être modifiés afin d'intégrer des molécules pouvant nous informer sur la microbiologie des tumeurs. Les futurs travaux impliqueront l'utilisation d'un spectromètre multi-canal pour la collecte simultanée des signaux principaux, des signaux de référence et des signaux de fond, l'incorporation d'une lentille ou d'une fibre monomode pour réduire le volume sensible, ainsi que le développement de meilleures techniques d'extraction des données spectrales. Il est prévu que la technique proposée sera applicable à la cartographie de dose en 3D au moyen de la tomographie optique diffuse, à l'imagerie par EC en temps réel et la localisation spatiale durant la radiothérapie, ainsi qu'à la modulation du faisceau en fonction du microenvironnement de la tumeur.

# TABLE OF CONTENTS

<b>ABSTRACT .....</b>	<b>1</b>
<b>RÉSUMÉ .....</b>	<b>3</b>
<b>LIST OF FIGURES AND TABLES .....</b>	<b>8</b>
<b>INTRODUCTION.....</b>	<b>10</b>
1.1 Radiation therapy .....	10
1.1.1 Cancer and radiation therapy .....	10
1.1.2 Radiation dosimetry .....	13
1.1.3 Image guidance .....	15
1.2 Cherenkov radiation.....	16
1.2.1 History.....	16
1.2.2 Overview.....	16
1.2.3 Cherenkov emission imaging in radiotherapy .....	18
1.3 Optical imaging of tissue .....	23
1.4 Optical detection instrumentation.....	24
1.4.1 Optical spectrometers.....	24
1.4.2 Optical detectors .....	28
1.4.3 Fiber optics.....	31
1.5 Thesis – motivation, objectives, organization .....	35
1.5.1 Dosimetry.....	35
1.5.2 Imaging .....	36
1.5.3 Thesis organization .....	37
<b>RELEVANT THEORY AND BACKGROUND .....</b>	<b>38</b>
2.1 Cherenkov radiation.....	38
2.2 Ionization chambers.....	39
2.3 Quantum dots.....	42
2.4 Monte Carlo technique.....	46
2.5 Statistical data analysis .....	50
2.5.1 Mean, median, mode and standard deviation.....	50
2.5.2 The normal probability distribution .....	51
2.5.3 Quantile-quantile plots.....	52
2.5.4 Pearson and Spearman correlation coefficients .....	53
<b>MATERIALS AND METHODS .....</b>	<b>55</b>
3.1 Computer simulation.....	55
3.1.1 Simulations .....	55
3.1.2 Geant4 Cherenkov simulator design .....	57
3.2 Phantoms.....	60
3.3 Detector system and setup .....	61
3.3.1 Dose measurement setup.....	62
3.3.2 Optical measurement setup .....	63
3.3.3 Fiber positioning .....	65
3.4 Quantum dots.....	67
3.5 Digital signal processing.....	68
3.6 Noise studies.....	68

<b>RESULTS AND DISCUSSION .....</b>	<b>70</b>
4.1 Radiation dose versus Cherenkov emission correlation analysis .....	70
4.1.1 Preliminary evaluation .....	70
4.1.2 Angular sensitivity analysis .....	71
4.1.3 Correlation between radiation dose and Cherenkov emission .....	73
4.1.4 Two-fiber dependence.....	80
4.2 Spectral shift experiments.....	81
4.3 Noise studies .....	86
<b>CONCLUSION .....</b>	<b>91</b>
<b>List of Abbreviations .....</b>	<b>95</b>
<b>Bibliography .....</b>	<b>97</b>

## LIST OF FIGURES AND TABLES

<b>Figure 1.1:</b>	Schematic drawing of a medical linac (adapted from Ref. 6).....	13
<b>Figure 1.2:</b>	Simplified drawing of a charged particle (point P) traveling at a speed (a) lower and (b) faster than the phase speed of light in a medium, causing, respectively (a) symmetric and (b) asymmetric polarization in the medium (adapted from Ref. 16).	17
<b>Figure 1.3:</b>	Absorption coefficient distributions of water (H <sub>2</sub> O), hemoglobin (Hb), and oxygenated hemoglobin (HbO <sub>2</sub> ) (adapted from Ref. 44).....	23
<b>Figure 1.4:</b>	Reflective diffraction grating – basic components and model of wavelength splitting (adapted from Ref. 45).	25
<b>Figure 1.5:</b>	Simplified schematic of a Michelson interferometer (adapted from Ref. 47).	27
<b>Figure 1.6:</b>	Bucket brigade analogy of CCD detection process (adapted from Ref. 49).....	29
<b>Figure 1.7:</b>	General structure of a cylindrical glass-based fiber optic cable (adapted from Ref. 51).	31
<b>Figure 1.8:</b>	Diagrams of the process of (a) reflection and refraction and (b) total internal reflection.	32
<b>Figure 1.9:</b>	Schematic of a fiber optic cable – acceptance angle and cone (adapted from Ref. 51).	33
<b>Figure 2.1:</b>	Huygens’ principle description of the Cherenkov effect (adapted from Ref. 16).....	38
<b>Figure 2.2:</b>	Basic design of a typical cylindrical ionization chamber for radiation dosimetry (adapted from Ref. 6).	40
<b>Figure 2.3:</b>	Typical electron and photon beam PDDs in water for varying nominal beam energies at standard field size and SSD (adapted from Ref. 6).....	41
<b>Figure 2.4:</b>	Energy level diagram of molecules, quantum dots, and bulk semiconductors (adapted from Ref. 54).....	43
<b>Figure 2.5:</b>	Simplified drawing of (a) a quantum dot surface-modified with an organic ligand, (b) a typical core-shell quantum dot, and (c) an energy level diagram of a typical core-shell quantum dot (adapted from Ref. 38).	44
<b>Figure 2.6:</b>	Diagram of band gap versus lattice constant for a number of semiconductors (adapted from Ref. 55).	45
<b>Figure 2.7:</b>	Geant4 simulation of 5 18 MeV positrons incident on a 4×4×4 cm <sup>3</sup> block of water. Blue, red and green correspond to positive, negative and neutral particles. The OpenGL driver was used for visualization.	49
<b>Figure 2.8:</b>	The normal probability distribution (adapted from Ref. 65).	51
<b>Table 1:</b>	Setup parameters used in Simulations 3 and 4.....	56
<b>Figure 3.1:</b>	Slices of dose distribution scored in Geant4 with a 10×10×10 cm <sup>3</sup> scoring mesh of 0.5×0.5×0.5 cm <sup>3</sup> bins, deposited by a simulated 18 MeV electron beam (made up of 200 particles) of field size 6×6 cm <sup>2</sup> at 100 cm SSD, incident on a 10×10×10 cm <sup>3</sup> block of water. The OpenGL driver was used for visualization.	58
<b>Figure 3.2:</b>	Jar of beef blood (top left) used in preparation of tissue-simulating phantoms and a representative image of a tissue-simulating phantom used in the Cherenkov NIR shift experiments.	61
<b>Table 2:</b>	Experimental setup parameters.	62
<b>Figure 3.3:</b>	Optical acquisition setup for (a) dose versus Cherenkov and (b) tissue-simulating phantom experiments. The spectrometer, which is inside (dose-Cherenkov and first part of NIR shift studies) or outside (second part of NIR shift studies) of the treatment room, is connected to a computer on the outside of the room via a USB connection (top left). A fiber optic cable is attached to the spectrometer (top right) and positioned (a) in the water or (b) on the outside of the tissue-simulating phantom.	64
<b>Figure 3.4:</b>	Diagram of fiber acquisition geometry for dose versus Cherenkov studies. As depth z was varied, the distance x from the field edge was adjusted accordingly (based on z and the beam angle) to ensure the fiber was positioned at the field edge. An image of the angled accelerator is shown to facilitate understanding of the acquisition geometry. Diagram is not drawn to scale.	66

<b>Figure 3.5:</b> Representative (a) absorption and (b) emission spectra of CdSe/ZnS core-shell quantum dots in water (courtesy of NN-Labs, LLC). .....	67
<b>Figure 4.1:</b> Percent depth dose (PDD) and percent depth Cherenkov emission (PDCE) photons acquired by simulating 4,000,000 events via Monte Carlo simulation in Geant4 of an 18 MeV electron beam incident on a block of water. ....	70
<b>Figure 4.2:</b> Photo of a wedged 18 MV photon beam incident on a water tank. ....	71
<b>Figure 4.3:</b> Simulated Cherenkov emission (CE) versus radiation dose deposited by an 18 MeV electron beam, incident on a $10 \times 10 \times 10$ cm <sup>3</sup> block of water, scored in $0.5 \times 0.5 \times 0.5$ cm <sup>3</sup> voxels. This data represents the simulation of 4,000,000 events in Geant4. ....	71
<b>Figure 4.4:</b> Angular distribution of (a) simulated (10,000 events) Cherenkov signal by an 18 MeV electron beam incident on a block of water at 53° to the surface normal and (b) Cherenkov signal by an 18 MeV linac electron beam, acquired with a horizontal fiber with varying gantry angle. All angles are defined relative to the surface normal. Error bars designate the 90% confidence interval. ....	72
<b>Figure 4.5:</b> Cherenkov emission (CE) simulation results (5,000,000 events) and experimental beam-axis dose and CE measurements, all normalized to 1 at the point of maximum signal, acquired with a 18 MeV electron beam and 47° incidence angle. Error bars designate the 90% confidence interval. ....	74
<b>Figure 4.6:</b> Cherenkov emission (CE) simulation results (5,000,000 events) and experimental CE measurements, normalized to 1 at a 2 cm depth, acquired with a 18 MeV electron beam and 47° incidence angle. Error bars designate the 90% confidence interval. ..	76
<b>Figure 4.7:</b> Cherenkov emission (CE) simulation results (5,000,000 events), shifted downstream by 1.7 cm, and experimental beam-axis dose measurements, all normalized to 1 at the point of maximum signal, acquired with a 18 MeV electron beam and 47° incidence angle. ....	77
<b>Figure 4.8:</b> Cherenkov emission (CE) simulation results (5,000,000 events), shifted downstream by 0.1 cm, and experimental beam-axis dose measurements, all normalized to 1 at the point of maximum signal, acquired with a 6 MeV electron beam and 47° incidence angle. ....	78
<b>Figure 4.9:</b> Cherenkov simulation results normalized to 1 at the point of maximum signal for an 18 MeV beam of incidence angle 47°, detected with a fiber centered or offset by 1 cm relative to the beam axis. ....	80
<b>Figure 4.10:</b> Water tank Cherenkov spectra acquired with the Avantes setup. Spectra were acquired with an 18 MeV electron beam, with and without CdSe/ZnS core-shell quantum dots (QDs) positioned in front of the fiber in water, with field sizes of $5 \times 5$ and $5 \times 3$ cm <sup>2</sup> . Circled area designates the spectral shift region. ....	82
<b>Figure 4.11:</b> Tissue phantom Cherenkov spectra acquired with the Avantes setup. Spectra were acquired with an 18 MeV electron beam, with and without CdSe/ZnS core-shell quantum dots placed in front of the fiber in a tissue-simulating phantom at depths of 0 and 1 cm. Circled area designates the spectral shift region. ....	83
<b>Figure 4.12:</b> Cherenkov spectra acquired with an 18 MeV electron beam incident on water or on a tissue-simulating phantom. ....	84
<b>Figure 4.13:</b> Water tank Cherenkov spectra acquired with the Acton-PIXIS setup. Spectra were acquired with an 18 MeV electron beam, with and without CdSe/ZnS core-shell quantum dots (QDs) positioned in front of the fiber in water. ....	85
<b>Figure 4.14:</b> Tissue phantom Cherenkov spectra acquired with the Acton-PIXIS setup. Spectra were acquired with an 18 MeV electron beam, with and without CdSe/ZnS core-shell quantum dots placed in front of the fiber in a tissue-simulating phantom at a depth of 0.5 cm. ....	86
<b>Figure 4.15:</b> Sample Q-Q plot of beam-off distribution of pixel values over all pixels. ....	88
<b>Figure 4.16:</b> Sample Q-Q plot of center few 100 beam-off values from the sorted distribution for all pixels. ....	88
<b>Figure 4.17:</b> Sample Q-Q plot of beam-on signal distribution of one pixel. ....	89

# *Chapter 1*

## INTRODUCTION

---

### **1.1 Radiation therapy**

#### 1.1.1 Cancer and radiation therapy

Cancer is a broad class of malignant diseases involving abnormal unregulated cell proliferation, which can result in invasion of and interference with the normal functioning of nearby tissues, as well as distant metastasis.<sup>1</sup> In their 2011 article “The Hallmarks of Cancer: The Next Generation” published in *Cell*,<sup>2</sup> Douglas Hanahan and Robert Weinberg proposed 4 common characteristics associated with all cancers: (1) abnormal metabolic pathways; (2) immune system evasion; (3) chromosome abnormalities and unstable deoxyribonucleic acid (DNA); and (4) inflammation. The term ‘cancer’ was created by the Greek physician Hippocrates (460-370 BC), who used the terms *carcinoma* and *carcinoma* to designate non-ulcer and ulcer forming tumors, respectively.<sup>1</sup> The meaning of these words refers to a crab possibly due to the crab-like appearance of tumors. One of the earliest written mentions of cancer is thought to date back to 3000 BC and is found in an Egyptian medical textbook called the *Edwin Smith Papyrus*.

Cancer prevention and treatment are issues of extreme importance because cancer is a leading cause of death on national and international scales. The risk of dying from cancer before age 75 was 11% worldwide in 2008<sup>3</sup> and it accounted for 30% of all deaths in Canada in 2009.<sup>4</sup> In contrast, the trend in mortality rates has been stable or declining for decades, which may be at least partially attributed to advancements in prevention and treatment techniques. Conventional treatment methods include surgical removal of the affected tissue, chemotherapy via administration of cancer-targeting drugs, radiation therapy where high-energy ionizing radiation is used for treatment, or a combination of these methods.<sup>5</sup> The number one goal of any treatment strategy is to maximize tumor control while minimizing damage to surrounding healthy tissue.

The therapeutic use of ionizing radiation, known as **radiation therapy**, constitutes one of the major modalities in cancer treatment. The quantity that represents the amount of radiation used in a given treatment is **absorbed dose**, which is defined as the amount of energy absorbed by the patient per unit mass. The SI unit of dose is the Gray (Gy for short, 1 Gy = 1 J/kg).<sup>6</sup> Radiation may be administered internally, by placing the source at the target site (called brachytherapy), or externally, by directing a radiation beam produced by an external source (such as a linear accelerator) at the treatment site. Ionizing radiation is composed of charged (electrons/protons) or uncharged (photons/neutrons) particles with sufficient kinetic energy to result in the eventual release of an electron from an atom or molecule (most often caused by a secondary particle, such as bremsstrahlung photons, positrons, secondary electrons, etc.), producing a much more reactive ion pair (electron + positive ion). This ion pair's reaction potential is often high enough to result in damage to important biomolecules in the living cell, such as DNA, the role of which is to carry the genetic recipe for development and functioning of all known living organisms with the exception of some viruses.<sup>7</sup> The aim of radiation therapy is to administer a sufficient dose of ionizing radiation to the target in order to damage its DNA beyond the cell's capacity for repair and, as a result, cause cell death. In the case of photons, DNA damage occurs in two ways:<sup>8</sup> by **direct action** of ejected (secondary) electrons on DNA, causing single, double strand breaks and other aberrations, and by **indirect action** on DNA by highly reactive free radicals (hydrogen, hydroxyl and hydroperoxyl) produced by the interaction of secondary electrons with water molecules (radiolysis).

In external beam radiotherapy, beams are composed of high-energy **directly ionizing** charged particles (electrons or protons) or **indirectly ionizing** uncharged particles (photons or neutrons). Directly ionizing radiation deposits energy via Coulombic (electrostatic) interactions, resulting in atomic excitations and ionizations, while indirectly ionizing radiation deposits energy by ejecting electrons from atoms or molecules, which in turn deposit energy via Coulombic interactions.<sup>8</sup> Photon or electron beams, externally produced by specialized

equipment, are most commonly used for treatment. Electron beams are generated by clinical linear accelerators (**linacs**) while the source of photons may be X-ray tubes, Cobalt-60, or linacs.<sup>6</sup> Cobalt-60 teletherapy units – some of the oldest radiotherapy machines developed – employ photons (gamma rays) emitted by nuclear decay of radioactive Cobalt-60. Though Cobalt-60 teletherapy machines are still in use today, medical linacs are a much more common means of photon beam generation in developed countries. X-ray tubes, which have been around since the late 19th century, accelerate electrons from a cathode filament towards a decelerating high atomic number anode (target) via a high external voltage applied across the tube. The Coulomb interactions between the accelerated electrons and the anode's nuclei produce kilovoltage (kV) energy X-rays in the form of what is termed **bremsstrahlung** radiation.<sup>6</sup> These relatively low energies result in low penetration depths in tissue, which makes them useful for treatment of superficial tumors. Linacs produce radiation beams by an analogous method, however, the difference lies in the linacs capacity for producing electron beams and in the beam energies involved – which in the case of linacs fall in the megavoltage (MV) range – and thus in the corresponding application. Linac generated photon beams can be used for deep-seated sites, while electron beams are used for treating superficial sites and are produced by removing the X-ray target. A flattening filter or scattering foil is placed in the beam path in the case of photon or electron beams, respectively, in order to make the intensity spectrum as uniform as possible across the field.<sup>6</sup> A collimator is used to limit the field size to the size of the treatment area. The beam generating and beam forming components of a linac, including those mentioned here, are shown in Figure 1.1.

Whether the particular motive for administering radiotherapy is to cure the disease (curative) or to simply alleviate discomfort due to symptoms (palliative), since ionizing radiation is damaging to all tissue, it is of utmost importance to ensure that damage to the surrounding healthy tissue is minimized while a dose of adequate magnitude is delivered to the target in order to control it. This is often challenging due to many factors, some of which include the non-conventional shapes of tumors, variations in tumor position and shape between and during

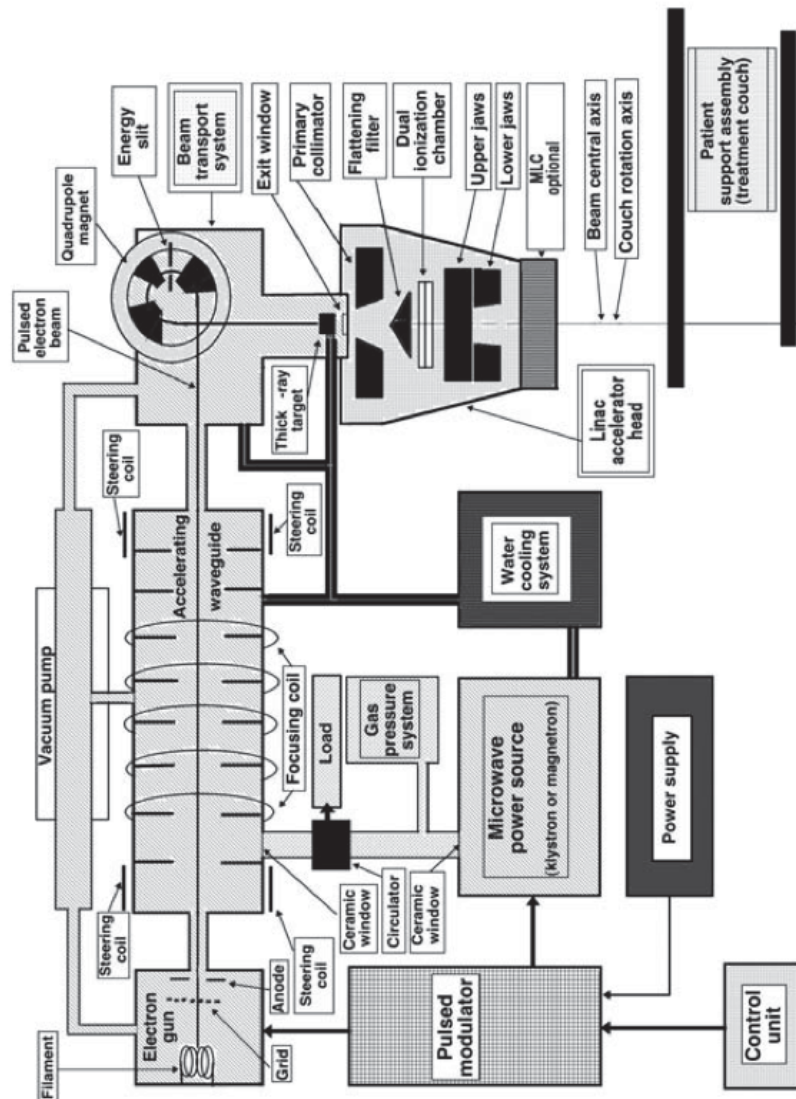


**Figure 1.1:** Schematic drawing of a medical linac (adapted from Ref. 6).

treatments as a result of various factors, such as breathing, and proximity of the target to highly radiosensitive organs, such as the spine. Therefore, various tumor-targeting techniques are often employed to further increase the tumor control probability (TCP) and decrease the normal tissue complication probability (NTCP). Two such techniques are image-guided radiotherapy (IGRT) and intensity-modulated radiotherapy (IMRT).<sup>9</sup>

### 1.1.2 Radiation dosimetry

**Dosimetry** (or dose measurement) protocols are vital for ensuring the treatment plan is accurately delivered to the patient in practice. The radiation detectors used

for this purpose are referred to as radiation dosimeters. Since water is the most prevalent substance in the human body, the behavior of most tissues when exposed to ionizing radiation is in large determined by the properties of water.<sup>8</sup> Therefore, dosimetry protocols conventionally involve a water tank or a solid material radiologically equivalent to water, such as polymethyl methacrylate (PMMA), polystyrene or epoxy resin based Solid Water™.<sup>6</sup> In the radiation therapy community, these are all commonly referred to as phantoms.

Clinical dosimetry procedures fall in two categories: reference and relative dosimetry.<sup>6</sup> Reference dosimetry measures dose delivered by a clinical machine at a reference point under reference conditions. Relative dosimetry entails measurement of dose at non-reference points and/or conditions. Generally, the output of a linac is measured in **monitor units (MUs)**.<sup>6</sup> Linacs incorporate monitor chambers (dosimeters), which are calibrated such that 1 MU is equivalent to 1 cGy (centi-Gray) at the depth of maximum dose in water for the same nominal beam energy, with a field size of 10×10 cm<sup>2</sup> at 100 cm from the source. Dosimeters used for reference dosimetry must be calibrated in water against a source of known output. This is called absolute dosimetry and is carried out in primary standards laboratories with a Cobalt-60 source and an absolute dosimeter (i.e. one that requires no calibration in a known radiation field, such as in the case of calorimetry).<sup>6</sup> The report of Task Group 51 (TG-51) of the American Association of Physicists in Medicine (AAPM) is one of the most commonly employed clinical reference dosimetry protocols.<sup>10</sup>

The accuracy of the delivered dose is affected by the following sources of uncertainty:<sup>11</sup> reference dosimetry, relative dosimetry, patient-specific treatment plan dose calculations, and treatment setup and delivery. An uncertainty limit in the delivered dose of ±5% is recommended and widely observed.<sup>12,13</sup>

Radiation dosimeters include ionization chambers, film, luminescence dosimeters, solid-state dosimeters, scintillators, and diamond dosimeters. A few things to consider when choosing a dosimeter for a particular application are: linearity, dose-rate dependence, energy dependence, directional dependence,

spatial resolution and dependence on environmental variables, such as temperature, pressure and humidity. There is no single dosimeter suited for all applications; different applications warrant different dosimeters. In all cases, correction factors must be applied to dosimeter readings to correct for issues such as radiation field perturbation caused by the difference in dosimeter and phantom materials and presence of the dosimeter active area in the field.

### 1.1.3 Image guidance

In addition to images acquired before treatment and used for treatment planning, image guidance can be used immediately before or during treatment to localize a target in a process called image-guided radiation therapy (IGRT).<sup>14</sup> IGRT techniques can be 2- (2D), 3- (3D) and 4-dimensional (4D), the last of which includes time as a variable to accommodate for breathing motion among other time dependencies, and include, but are not limited to, fluoroscopy, conventional computed tomography (CT), cone-beam computed tomography (CBCT), kV X-ray planar imaging, MV imaging, optical tracking, and ultrasound.

Though spatial resolution on the order of millimetres has been achieved with some of these modalities,<sup>14</sup> as in any medical research field there is still potential for improvement. The majority of these methods oblige the use of ionizing radiation in the form of kV or MV photons, which contributes to patient dose. Other methods, such as ultrasound and optical tracking, where an external or implanted reference system of fiducial optical markers are tracked by cameras to construct an image, do not involve ionizing radiation, but have drawbacks of their own, such as low resolution in the former case and no actual tumor shape or positioning information in the latter.<sup>14</sup> An alternative to these approaches is to use intrinsic characteristics of the radiation beam for guidance as proposed here.

## 1.2 Cherenkov radiation

### 1.2.1 History

In the autumn of 1933 at the P.N. Lebedev Physical Institute in Leningrad, USSR, Pavel Alekseyevich Cherenkov (1904-1990), a peasant's son and Soviet physicist, was working on his dissertation on the effects of radioactivity in liquids under the supervision of Sergey Ivanovich Vavilov (1891-1951) when he noticed a faint unexplained glow by a sample of sulfuric acid exposed to the gamma radiation of radium.<sup>15</sup> This is the story of the discovery of what was later termed **Vavilov-Cherenkov radiation (Cherenkov for short)** in honor of its discoverers. A theory of this phenomenon was published in 1937 by Ilya Mikhailovich Frank (1908-1990) – another of Vavilov's students – and by Igor Yevgenyevich Tamm (1895-1971), also from the P.N. Lebedev Physical Institute. All three researchers shared the Nobel Prize in Physics in 1958 “for the discovery and the interpretation of the Cherenkov effect.”<sup>15</sup>

### 1.2.2 Overview

Cherenkov emission is an effect of asymmetrical polarization of a dielectric (poorly conducting) medium by a charged particle traveling faster than the phase speed of light in the medium (Figure 1.2b).<sup>16</sup> The phase speed of a particle in a medium is defined as the speed at which the phase of a wave propagates, where the phase is an arbitrary position in time and/or space of a fixed point on a waveform.<sup>17</sup> The phase speed is determined by the speed of interactions between light photons and atoms/molecules. Though the speed of light in vacuum  $c = 2.998 \times 10^8$  m/s cannot be surpassed, in materials of index of refraction lower than 1, the phase speed of light is lower than  $c$  and can therefore be exceeded by a particle traversing the medium with sufficient kinetic energy. Individual photons still travel at a velocity  $c$ , however the rate at which they are absorbed and re-emitted by the medium determines the speed of their combined propagation, i.e. the phase speed.<sup>17</sup>

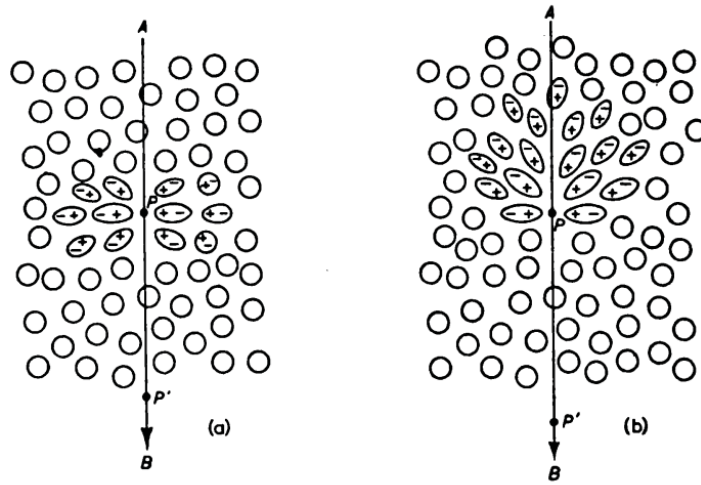


**Figure 1.2:** Simplified drawing of a charged particle (point P) traveling at a speed (a) lower and (b) faster than the phase speed of light in a medium, causing, respectively (a) symmetric and (b) asymmetric polarization in the medium (adapted from Ref. 16).

When a charged particle traverses a dielectric medium, it polarizes the medium (causes partial separation of positive and negative charge) along its track by photon transfer to the surrounding atoms/molecules (Coulombic interactions). Subsequently, the electric dipoles (polarized atoms/molecules) created in the medium de-excite by photon emission. If the speed of the particle is lower than the phase speed of light in the medium, this polarization is symmetric (Figure 1.2a) because the photon exchange between the propagating particle and its surroundings and the subsequent dipole de-excitation is on average uniform with direction. If the particle speed is larger than the phase speed of light (Figure 1.2b), the polarization becomes asymmetric along the particle track because dipoles de-excite more slowly than they are created. This asymmetry and directional de-excitation amounts to a coherent radiation field apparent at a distance from the electron track. This field is **Cherenkov radiation**.<sup>16</sup> The threshold condition for the Cherenkov effect is therefore

$$\frac{v_{cp}}{v} > 1, \quad (1.1)$$

where  $v_{cp}$  is the charged particle velocity and  $v$  is the phase velocity of light in the medium, which can be expressed as

$$\beta n > 1, \quad (1.2)$$

where  $\beta$  is the particle speed normalized to  $c$  and  $n$  is the medium **index of refraction** defined as<sup>17</sup>

$$n = \frac{c}{v}. \quad (1.3)$$

By the nature of its origin, the Cherenkov spectrum is continuous. It appears blue because it is most intense near the blue region of the electromagnetic spectrum and gradually decreases for longer wavelengths. A quantitative account of the Cherenkov effect is provided in Section 2.1 and Ref. 16.

### 1.2.3 Cherenkov emission imaging in radiotherapy

Though famous for its manifestation as the characteristic blue glow of nuclear reactors and for its numerous applications in particle physics and astrophysics, the Cherenkov effect can also be observed in radiotherapy when charged particles of energies satisfying the threshold are involved. To satisfy the Cherenkov threshold, according to Equation 1.2, the normalized velocity  $\beta$  of a particle traveling in a medium of refractive index 1.3, as in the case of water at optical wavelengths,<sup>18</sup> must be equal to or greater than 0.77, which in the case of an electron or positron corresponds to a kinetic energy  $E_k$  of 290 keV calculated according to<sup>6</sup>

$$E_k = m_0 c^2 \left( \frac{1}{\sqrt{1 - \beta^2}} - 1 \right), \quad (1.4)$$

where  $m_0 c^2 = 511$  keV is the rest energy of the electron/positron. Medical linacs accelerate electrons to 4 to 25 MeV energies,<sup>6</sup> which is significantly higher than the 290 keV threshold in water. In addition, decay products of some radioactive isotopes (also termed radionuclides or radioisotopes) commonly used for internal radiotherapy, such as Bi-212 and Y-90, and medical imaging radioisotopes, such as Cu-64 and F-18, often satisfy this threshold.<sup>19</sup>

Perhaps due to immense improvements in optical detection technology, recently much effort has been put towards investigation of Cherenkov emission

for applications in cancer diagnosis and treatment. Cherenkov emission by nearly all radioisotopes of interest for medical applications (diagnostic and therapeutic) has been investigated at this time.<sup>20-22</sup> Based on energy and number of decay electrons, the number of Cherenkov photons per radioactive decay for commonly used medical radionuclides obeys the following trend (in order of decreasing number of photons): Y-90 > Ga-68 > O-15 > C-11 > I-124 > Zr-89 > F-18 > Cu-64.

Diagnostic radionuclides are generally imaged via positron emission tomography (PET) or single-photon emission computed tomography (SPECT), which are three-dimensional imaging modalities utilizing high-energy photons produced by positron-emitting or by gamma-emitting radionuclides, respectively.<sup>23</sup> Despite challenges, such as lower penetration depth and spatial resolution, Cherenkov imaging of diagnostic radionuclides has a number of advantages over radioactive decay emission imaging (PET and SPECT). For example, in small animal PET imaging for pre-clinical studies only 1 or 2 animals can be imaged at a given time, while Cherenkov emission imaging allows for the simultaneous scanning of up to 5 animals using a considerably cheaper bioluminescent imaging unit, which also entails lower service costs.<sup>24</sup> In addition, radioisotope imaging only provides functional (metabolic) information and no anatomical information about the subject, because radioisotopes are concentrated at the site of interest via attachment of a biologically active molecule, such as fluorodeoxyglucose (FDG), the uptake of which, and resulting radioactive emission, only represents functional information at a given site of radionuclide localization. On the other hand, an additional white light image can be acquired during Cherenkov emission imaging, providing an anatomical context. Furthermore, Cherenkov imaging can be used in conjunction with PET or SPECT, as for example demonstrated in the Cherenkov-guided surgery experiments of Holland et al.<sup>25</sup> Recently (since August 2012), clinical trials have commenced for imaging Cherenkov emission in patients undergoing a PET scan with 18F-FDG (FDG as a targeting biologically active glucose-analog molecule, substituted with the F-18 radioisotope for detection with PET). The trials are conducted under the

direction of Jan Grimm, MD, PhD, at the Memorial Sloan-Kettering Cancer Center in New York, in collaboration with National Institutes of Health, and are scheduled to be completed in August 2014 with an estimated 120 participants.

Cherenkov emission imaging of therapeutic radionuclide distributions is also of interest and has been studied. In order to only treat locally and thus minimize irradiation of healthy tissue, it is desirable that radionuclides used for therapeutic purposes decay mainly via products of low tissue penetrability, such as alpha particles and electrons. The decay chains of most therapeutic radionuclides also include enough positron or photon products, making them suitable for imaging by PET or SPECT.<sup>23</sup> However, the best radionuclides are those that involve as little highly penetrating products as possible in order to minimize radiation exposure of healthy tissue. This challenges their detection by standard imaging techniques.

In order to overcome the low tissue penetrability of Cherenkov emission, resulting from the predominance of highly attenuated blue wavelengths in its spectral distribution, its use for excitation of various fluorescent probes absorbing at short wavelengths and emitting at a longer wavelength has been studied. In particular, Cherenkov-induced fluorescence has been successfully demonstrated with quantum dot nanoparticles,<sup>26, 27</sup> DMNP-luciferin<sup>28</sup> and protoporphyrin IX<sup>29</sup> among other fluorescent probes.

Cherenkov radiation produced by clinical linacs has also recently been studied for applications in both imaging and dosimetry by Axelsson et al.,<sup>29, 30</sup> Glaser et al.,<sup>31-34</sup> Zhang et al.<sup>35, 36</sup> and Demers et al.,<sup>37</sup> whose findings motivated the present work. Cherenkov signal, detected with a CCD camera (see Section 1.4.2), and deposited dose were spatially correlated in two dimensions in a water tank with the use of a Cherenkov-to-dose conversion factor determined through computer simulation, necessary to account for the angular anisotropy of Cherenkov emission, and varying with position,<sup>32</sup> and with the use of a fluorescent dye introduced into the water tank in order to ensure angular isotropy of the signal and remove the need for a conversion factor.<sup>33</sup> This method was

found to be linear with dose and independent of dose rate and was extended to three dimensions by tomographic acquisition and reconstruction of two-dimensional projection images of Cherenkov emission in a water tank.<sup>34</sup> Motivated by these findings, the present work demonstrates a new method for correlation between dose and Cherenkov without the use of a computer-generated spatially dependent conversion factor and without introduction of a fluorescent dye.

Cherenkov emission has also been studied for imaging applications in radiotherapy. It was shown that Cherenkov emission can be produced by both photon and electron beams in a medium that simulates the radiological and optical properties of tissue (**tissue-simulating phantom, or tissue phantom for short**) and can excite protoporphyrin IX, a NIR-emitting fluorophore,<sup>29</sup> or platinum(II)-G4 (PtG4), an oxygen-sensitive NIR-emitting phosphorescent probe,<sup>35</sup> when either is dissolved in the phantom. From this it can be concluded that monitoring of external beam irradiation via Cherenkov excitation of molecular fluorescence is feasible. Computer simulation results show that Cherenkov emission and Cherenkov-excited phosphorescence of PtG4 may both be detected at depths up to 2-3 centimeters in tissue.<sup>35</sup> In addition, oxygenation (expressed either as hemoglobin oxygen saturation or oxygen partial pressure), which plays an important role in radio-sensitization,<sup>8</sup> was successfully characterized in a tissue-simulating phantom through a spectral fit of the signal to a theoretical light transport model based on optical diffusion theory,<sup>30, 35</sup> and through phosphorescence lifetime analyses of the oxygen-sensitive PtG4 probe.<sup>35</sup> In order to maximize the **signal-to-noise ratio (SNR)** achievable in a routine clinical setting, effective implementation of a method involving beam pulse matching of the acquisition time profile was demonstrated for signal acquisition in oxygenated and deoxygenated tissue phantoms in the presence of ambient lighting.<sup>31</sup> Three-dimensional tomographic reconstruction has also been carried out for the case of a tissue-simulating phantom incorporating an anomaly with a fluorescent probe (Cyto500LSS),<sup>37</sup> and of oxygen partial pressure in a tissue phantom containing the probe PtG4 as an oxygen-sensitive reporter.<sup>36</sup> The present work builds on

these findings by demonstrating a new approach based on a NIR-shift of the Cherenkov signal from a linac-generated treatment beam incident upon a tissue-simulating phantom using zero-dimensional semiconductor nanoparticles known as quantum dots (see Section 2.3).<sup>38</sup> Quantum dots possess a great advantage over other luminescent probes with biomedical applications since their physical and biochemical properties are tunable and in general much more easily controlled. This is particularly useful for targeting and localization and for tumor microenvironment sensing in radiotherapy. Quantum dots are very well-suited for excitation by Cherenkov radiation since their absorption profile, as the Cherenkov emission profile, is continuous and decreases from short to long emission wavelengths. In addition, they are photostable and possess narrow distinctive emission peaks.<sup>39, 40</sup> By modifying their surface chemistry to incorporate oxygen reporters, wavelength-shifting quantum dots can be developed for Cherenkov-stimulated oxygenation sensing and beam modulation in radiotherapy.

Despite numerous unique advantages of Cherenkov emission imaging, implementation of the method also faces some challenges. Three main issues with the use of radioisotopes as a light source are:<sup>24</sup>

1. Dependence of Cherenkov emission on radioisotope decay and thus necessity for radioisotopes with a long half-life (time required for the initial amount to decrease by a half);
2. Relatively low intensity as compared to conventional methods, such as bioluminescence imaging<sup>41</sup> and the necessary removal of all other sources of light;
3. Tissue attenuation, which is strongest towards the blue region of the electromagnetic spectrum, resulting in signal loss due to the predominantly blue-weighted Cherenkov spectrum intensity.

Issue 1 can be resolved by choosing long half-life radioisotopes, such as Zr-89. Issue 2 is partially countered by the lack of a non-specific background signal, such as the excitation source required by fluorescent compounds, and can be

compensated for by increasing acquisition times for all but the shortest-lived radioisotopes. As described above, spectral shifting techniques are under study as a partial solution to Issue 3. In addition, applications of the technique may focus on imaging of superficial tumors or of organs with high radionuclide uptake, such as the kidneys, spleen and thymus.<sup>24</sup>

### 1.3 Optical imaging of tissue

Tissue optical imaging has great potential for medical applications<sup>42</sup> due the fact that it can probe both functional and structural information; it is non-invasive, non-ionizing and real-time; it requires portable and low-cost equipment; and it can provide both microscopic (with the aid of microscopes) and macroscopic information, body cavity information with the aid of endoscopes, and quantitative information. The major limiting factor for the application of optical imaging in medicine is penetration depth in tissue. The optical properties of biological tissues are primarily governed by the presence of water, blood and lipids.<sup>43</sup> Scattering and absorption properties of a tissue type are defined mainly by its lipid content and by its water and blood content respectively. Biological tissues are characterized by strong scattering and absorption of optical wavelengths, particularly in regions of the electromagnetic spectrum outside of the **near-infrared (NIR) window** (Figure 1.3), where tissues are most transmissive.<sup>44</sup> The

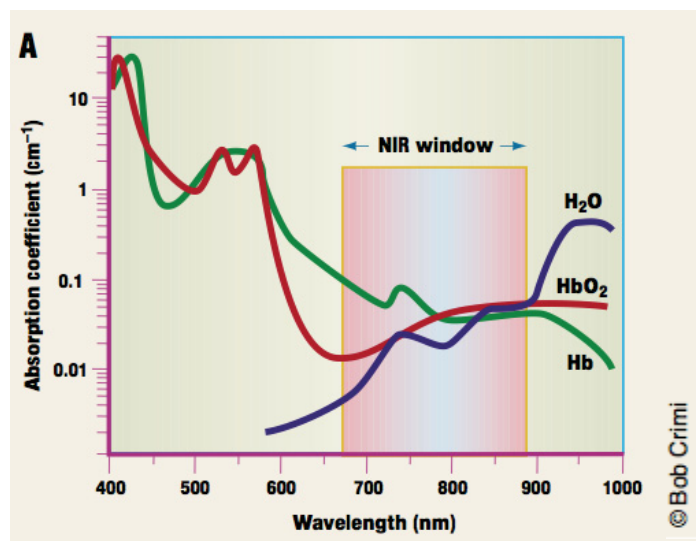


**Figure 1.3:** Absorption coefficient distributions of water (H<sub>2</sub>O), hemoglobin (Hb), and oxygenated hemoglobin (HbO<sub>2</sub>) (adapted from Ref. 44).

NIR window depends on tissue type but generally encompasses wavelengths in the region of 650 to 900 nm. Penetration depths of a few centimeters have nevertheless become achievable due to advancements in optical instrumentation and mathematical modeling of light propagation in tissues.<sup>42</sup>

## 1.4 Optical detection instrumentation

### 1.4.1 Optical spectrometers

Optical spectrometers are analytic instruments used to separate and quantify the component wavelengths of an input light source based on wavelength-dependent factors, such as index of refraction or interference.<sup>45, 46</sup> The result is called a **spectrum**, which is a graph of intensity, or a related quantity, such as detector counts, versus wavelength. From this graph, different types of information can be inferred, such as the attenuation properties of a sample illuminated with white light, information about the source of light (ex: Cherenkov emission), or emission properties of a photoluminescent sample. Many types of spectrometers have been developed for various applications, some of the most ubiquitous of which include dispersive instruments, such as prism and grating spectrometers, and non-dispersive instruments, such as Michelson and Fabry-Pérot interferometer.<sup>45, 46</sup>

Prism spectrometers employ a prism, usually made of a type of glass, to split light into its component wavelengths based on the wavelength dependence of the index of refraction of the prism material.<sup>17</sup> The resolution of these types of spectrometers is limited by the size of the prism – the larger is the distance that light has to travel through a medium, the higher is the splitting effect of the wavelength-dependent index of refraction – and is proportional to the base length (the length of the side on which there is no incident or outgoing light). Since prism size is limited for practical applications, the resolution is generally low. Furthermore, the resolution varies with wavelength since it is dependent on the variable refractive index. Commercial prism spectrometers generally use lenses and/or mirrors to collimate incoming light onto a prism and focus outgoing light onto the detector.<sup>46</sup>

Grating spectrometers (used in this work) split light into its component wavelengths based on diffraction and interference.<sup>17</sup> **Diffraction** is the bending and spreading of light as it encounters a small obstacle, such as an opening in or an edge of a material of different refractive index. **Interference** is defined most concisely as the spatial interaction of one or more waveforms to form a resultant waveform, the amplitude of which at each location and each point in time equals the sum of the constituent waveform amplitudes at that location and point in time. Constructive interference occurs when the components have amplitudes of equal magnitude and sign and therefore the resultant amplitude equals double the component magnitude. Destructive interference occurs when the magnitudes and sign of the component amplitudes are not equal. From this it is evident that two waveforms of different wavelengths (such as red and blue) cannot interfere constructively since their waveforms cannot align.

The main components of a diffraction grating spectrometer are an entrance slit, a diffraction grating and an optical detector.<sup>46, 47</sup> A **diffraction grating** (Figure 1.4) is a surface made of regularly spaced transmitting or reflecting elements with a separation distance on the order of an optical wavelength (hundreds of nanometers). A beam incident on the grating experiences diffraction

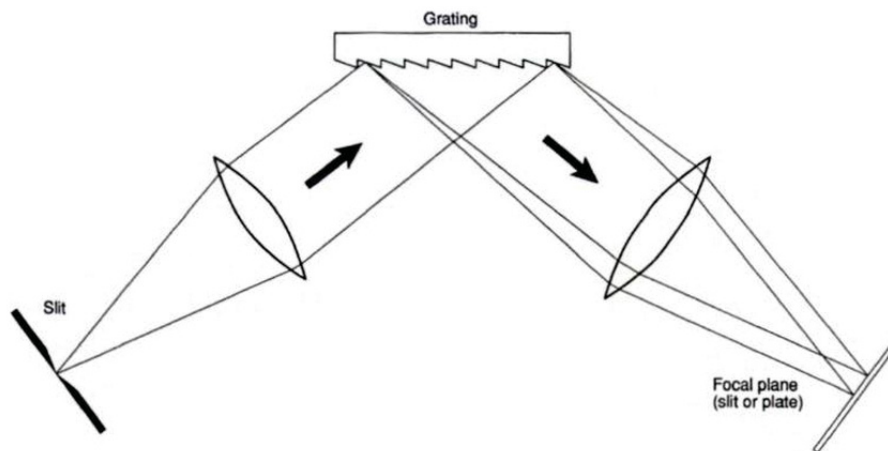


**Figure 1.4:** Reflective diffraction grating – basic components and model of wavelength splitting (adapted from Ref. 45).

at each grating element. The element spacing is made such that, for each wavelength, the path length difference along a particular angle for waves

diffracted from different elements is equal to an integer number of wavelengths, resulting in constructive interference for that wavelength and at that angle. Because this angle depends on wavelength, different wavelengths experience constructive interference in different directions and so the incoming source is split into its component wavelengths by the grating. Grating spectrometers generally incorporate carefully machined entrance slits in order to control the size and direction of the beam. The entrance slit ensures that only a small area of the source beam is directed towards the spectrometer optics and the grating and that light waves are approximately parallel to ensure alignment with the internal optics and minimize stray light. The size of the entrance slit affects the spectrometer's spectral resolution. Some issues with grating spectrometers are the stray light resulting from surface imperfections and the necessary compromise between total wavelength coverage and spectral resolution, both of which are determined by the groove frequency, which is generally expressed in lines per millimeter (ln/mm). Unlike prisms, reflective gratings do not depend on the transparency of the grating material.

Figure 1.5 gives a schematic diagram of a basic setup of a Michelson interferometer spectrometer.<sup>48</sup> It consists of two mirrors perpendicular to each other and a beamsplitter at the center at  $45^\circ$  with respect to the mirrors. Light incident upon the beamsplitter from a source is divided into two beams via transmission and reflection, which subsequently reflect from the mirrors, and after an additional transmission and reflection at the beamsplitter, recombine as they reach the detector. One of the mirrors is fixed, while the other is movable. By moving one mirror, the optical path difference between the two beams is varied, which varies their time of travel. When the optical path difference is set to an integer multiple of a given wavelength, the beam components with that wavelength interfere constructively at the detector. A temporal scan is performed by moving one mirror (at constant velocity or by stepping it between equally spaced points) and measuring the variation in intensity at the detector as a function of path difference. This is termed an interferogram. The spectrum (intensity versus wavelength distribution) can be obtained by performing a well-

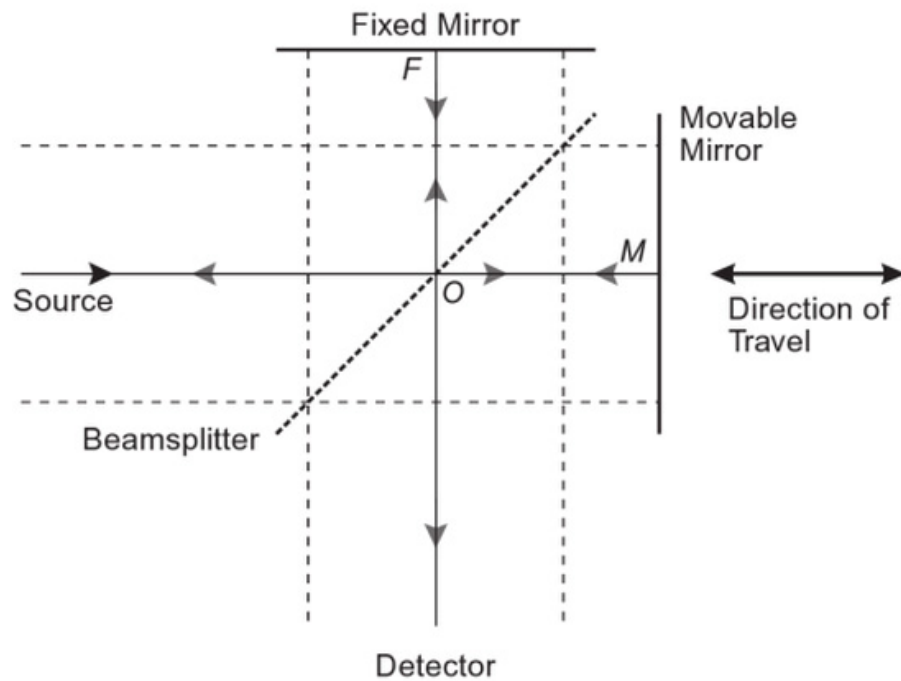


**Figure 1.5:** Simplified schematic of a Michelson interferometer (adapted from Ref. 47).

characterized mathematical operation called a Fourier transform on the interferogram. Fourier transforms are routinely used to transform functions of time into functions of frequency, or in this case wavelength. Michelson spectrometers have a sensitivity advantage over dispersive spectral detection techniques in that they take less time to obtain the same SNR and do not require a slit. On the other hand, they are bulky, complex and expensive and are therefore not necessary for many simpler applications. In addition, a large portion of the source light is lost due to the partial transmission/reflection of the beam splitter, which results in transmission/reflection towards the source instead of the detector.

An improvement over the Michelson interferometer is the Fabry-Perot interferometer,<sup>45</sup> which operates on the same principles as the Michelson interferometer. It incorporates 2 parallel lenses for collimating and focusing incoming and outgoing light respectively and 2 almost (in order to avoid undesired interference artifacts) parallel partially reflecting plates, between which light is partially reflected multiple times resulting in splitting of the source light into many parallel components. Because the Fabry-Perot interferometer uses

multiple beam interference, it is able to produce defined interference peaks. In comparison, Michelson interferometers record the interference pattern of only two beams. Therefore, Fabry-Perot interferometers entail very strict conditions for constructive interference, which can result in very high resolution, generally much higher than with a Michelson interferometer. A spectrometer of this resolution capacity is generally only required for resolving sources with narrowly separated wavelengths.

In the present study, a compact low-loss spectrometer is needed in order to detect the relatively low-intensity Cherenkov emission produced by radiotherapy treatment beams in water. Therefore, the optical detector of choice was a diffraction grating spectrometer.

#### 1.4.2 Optical detectors

An optical detector is an instrument that collects incident light and converts it to a quantifiable signal. This is generally carried out by absorption of optical photons to create electron-hole pairs resulting in an electrical signal that is detected. Most currently used optical detectors are based on semiconductor technology. Spectrometers have traditionally made use of photographic film; however the capacity of semiconductor-array detectors to directly produce a digital signal and their excellent linearity, among numerous other advantages, has made them most common in current scientific optical detection applications.<sup>49</sup> A semiconductor is a material whose electrical conductivity (ability to transfer electrons) can be directional and controlled by applying an electric potential across it. It is generally made of a semiconducting material, such as silicon, doped with a very small amount of an impurity, such as boron, which has an excess of charge carriers (electrons or positive ‘holes’, i.e. lack of electrons). One of the most common examples of optical semiconductor-array detectors is the **charge-coupled device (CCD)**.

A CCD array is made of a silicon semiconductor substrate doped with impurities to provide the charge carriers necessary for electrical conductivity,

covered by a silicon dioxide insulator, on top of which is positioned an array of conducting metal elements (pixels).<sup>49</sup> CCD operation can be divided in two steps: photon collection and charge readout. Electric connections at each pixel provide electric potentials necessary to keep charge inside pixels during photon collection and transfer charge between pixels during readout. During the collection stage, incident optical photons interact with the silicon to excite electrons into a conduction energy band, producing an electron-hole pair. The number of electron-hole pairs produced is directly proportional to the photon intensity. After photon collection is complete, a timed sequence of electric potentials is applied across pixels in order to transfer the collected charge, called a charge packet, to neighboring pixels on the same row towards the last column, called the serial register. The register is reserved for charge packet readout and not used for photon detection. After each time the register is filled with charge packets from the preceding pixels, its charge packets are discharged and read one at a time through an output amplifier. An analogous ‘bucket brigade’ situation is illustrated in Figure 1.6. Based on their principle of operation, two-dimensional arrays are used for imaging applications in interferometers and by multi-channel (prism and grating) dispersive spectrometers, while single-channel spectrometers only require one-dimensional arrays (1 row of pixels). Multi-channel spectrometers measure multiple spectra simultaneously (ex: background and signal or at different positions/angles) while single-channel spectrometers can only measure one spectrum at a given time.

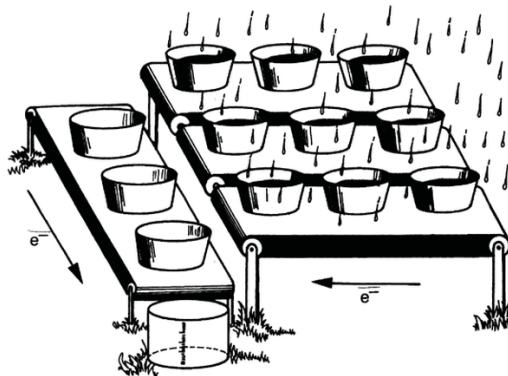


**Figure 1.6:** Bucket brigade analogy of CCD detection process (adapted from Ref. 49).

There are 3 primary sources of noise in CCD detection – shot, CCD, and readout noise.<sup>50</sup> Noise is the random fluctuation in signal, resulting from statistical variability of measured parameters, device composition, environmental conditions, and other factors. Shot or photon noise results from the fact that, while a source of constant intensity emits a constant number of photons on average, the actual number emitted and collected at the CCD during a finite acquisition period obeys a Poisson distribution, a discrete probability function, due to the discrete nature of light. This is true for any discrete variable. For a realistic (not too small) number of photons, the Poisson distribution approaches a normal distribution with a standard deviation equal to the square root of the mean (see Section 2.5 for definitions). Therefore, shot noise  $\sigma_{shot}$ , expressed as the standard deviation of the number of collected photons, is<sup>50</sup>

$$\sigma_{shot} = \sqrt{\overline{N_{photon}}} = \sqrt{\frac{I}{h\nu} t A \eta}, \quad (1.5)$$

where  $\overline{N_{photon}}$  is the average number of photons collected by the CCD,  $I$  is source irradiance at the CCD in units of  $W/m^2$ ,  $h = 6.62606896 \times 10^{-34}$  Js is Planck's constant,  $\nu$  is photon frequency,  $t$  is exposure time,  $A$  is the area of a pixel, and  $\eta$  is the quantum efficiency. Quantum efficiency of a detector is a quantity representing the capacity of the detector to convert input signal into output signal. For a CCD detector, it is equal to the ratio of the number of optical photons incident on the CCD to the number of electron-hole pairs produced. For red wavelengths (~630 nm), its value is in the range 0.4-0.8 for many CCD detectors. The second type of noise, CCD sensor noise, is mainly due to dark current caused by thermal fluctuations in the amount of charge carriers, transfer noise from fluctuations in the amount of charge carriers caused by their transfer between pixels, and fixed pattern noise due to spatial differences in CCD noise behavior/sensitivity. Finally, readout noise results from CCD signal readout and amplification steps. Since these noise sources are uncorrelated, the total noise  $\sigma_{noise}$ , expressed as the standard deviation of the signal, equals the root mean square of all contributions as follows:<sup>50</sup>

$$\sigma_{noise} = \sqrt{\sigma_{shot}^2 + \sigma_{CCD}^2 + \sigma_{readout}^2}, \quad (1.6)$$

where  $\sigma_{CCD}$  and  $\sigma_{readout}$  represent CCD and readout noise respectively. The signal-to-noise ratio  $SNR$  for a CCD detector is equal to the average number of photons collected  $\overline{N_{photon}}$  divided by the total noise  $\sigma_{noise}$ . From Equations 1.5 and 1.6,

$$SNR = \frac{\overline{N_{photon}}}{\sigma_{noise}} = \frac{\overline{N_{photon}}}{\sqrt{\overline{N_{photon}} + \sigma_{CCD}^2 + \sigma_{readout}^2}}. \quad (1.7)$$

Therefore for sufficiently high intensities or long acquisition times, the SNR is mainly governed by the number of collected photons and is approximately equal to the square root of the number of photons.

#### 1.4.3 Fiber optics

In many applications, the source light cannot be fed directly into the spectrometer, but must be transferred from the source to the spectrometer by means of an optical

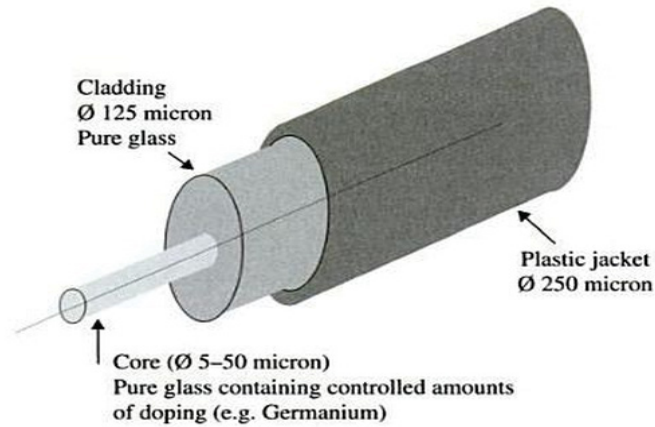


**Figure 1.7:** General structure of a cylindrical glass-based fiber optic cable (adapted from Ref. 51).

waveguide. Optical waveguides are characterized in terms of their geometry, material, mode (explained below), and refractive index properties. Today, some of the most commonly used optical waveguides, specifically in medical and telecommunication applications, are optical fibers.

The main components of most optical fibers include a cylindrical core, cladding and jacket (Figure 1.7).<sup>51</sup> The core and cladding are made of glass (most commonly fused silica) or plastic and define the light-guiding properties of the fiber. The purpose of the jacket, usually made of some type of plastic, is to absorb improperly guided light and provide strength and protection. The light guiding properties of optical fibers are based on the principle of total internal reflection.<sup>17</sup> When light traveling through a medium of a given index of refraction  $n_1$  is incident on a medium of a different index of refraction  $n_2$ , it experiences reflection and refraction (transmission through the boundary with a change in direction) at the boundary (Figure 1.8a). The angle  $\theta_{r2}$  of the refracted ray relative to the surface can be related to the incidence angle  $\theta_i$ , also relative to the surface, via Snell's law (in terms of sine):<sup>17</sup>

$$n_1 \sin(90^\circ - \theta_i) = n_2 \sin(90^\circ - \theta_{r2}), \quad (1.8a)$$

which in terms of cosine becomes

$$n_1 \cos \theta_i = n_2 \cos \theta_{r2}. \quad (1.8b)$$

Here, angles are defined relative to the surface, instead of the surface normal, and

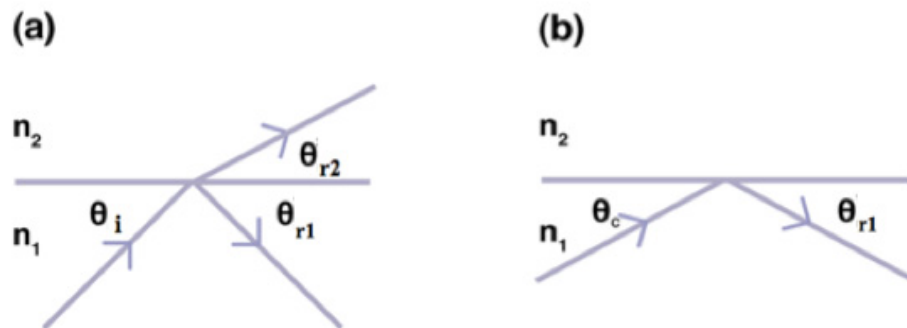


**Figure 1.8:** Diagrams of the process of (a) reflection and refraction and (b) total internal reflection.

Snell's law is expressed in terms of cosines for the sake of continuity in the discussion and derivation. For this expression to hold, it is evident that  $\theta_{r2}$  decreases with  $\theta_i$  and if  $n_2$  is smaller than  $n_1$ , then  $\theta_{r2}$  is smaller than  $\theta_i$ . Therefore, a critical incidence angle  $\theta_c$  exists such that  $\theta_{r2}$  equals  $0^\circ$ , meaning the refracted ray is parallel to the boundary surface. For incidence angles smaller than  $\theta_c$ , all light incident on the boundary is reflected back into the initial medium (Figure 1.8b). This phenomenon is called **total internal reflection**.<sup>17</sup> The index of refraction  $n_{clad}$  of an optical fiber cladding is made smaller than that of the core  $n_{core}$  in order to guide light through the fiber via total internal reflection (Figure 1.9). An important descriptor for optical fibers based on the critical angle is the fiber's **numerical aperture (NA)**, defined as the sine of the angle  $\theta_c^{air}$  with respect to the surface normal (i.e. the fiber axis) of a light ray incident on the end of the fiber in air, which would be refracted such that it experiences total internal reflection at an angle exactly equal to the fiber's critical angle.<sup>51</sup> The NA can be expressed in terms of the fiber's refractive indices  $n_{clad}$  and  $n_{core}$  and in terms of  $\theta_c$  as follows:

$$NA = \sin \theta_c^{air} = \sqrt{n_{core}^2 - n_{clad}^2} = n_{core} \sin \theta_c. \quad (1.9)$$

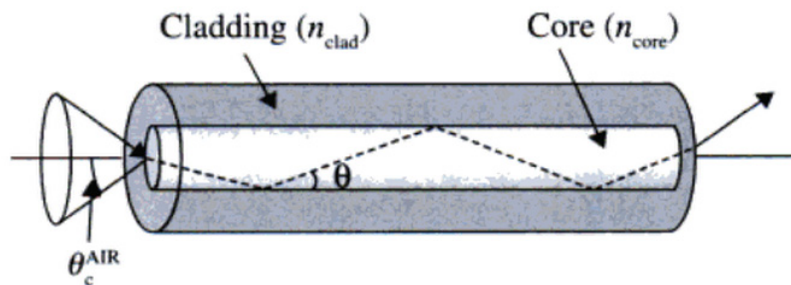


**Figure 1.9:** Schematic of a fiber optic cable – acceptance angle and cone (adapted from Ref. 51).

Light rays incident on the end of the fiber in air at angles smaller than  $\theta_c^{air}$  with respect to the fiber axis will experience total internal reflection and will be guided by the fiber to the spectrometer to be detected. Light rays incident with angles larger than  $\theta_c^{air}$  will be attenuated as they pass through the fiber since at every

core-cladding interface a fraction of the ray will be refracted towards the jacket. This angle  $\theta_c^{air}$  is the **acceptance angle** of the fiber in air and the cone defined by all angles smaller than  $\theta_c^{air}$  with axis along the fiber axis is the **acceptance cone** of the fiber in air. According to Snell's law (Equation 1.8) and the definition of NA (Equation 1.9), for an open-ended fiber in a surrounding medium of refractive index  $n_m$ ,

$$NA = n_{core} \sin \theta_c = n_m \sin \theta_c^m, \quad (1.10)$$

where  $\theta_c^m$  is the acceptance angle of the surrounding medium. Therefore, since the NA has a fixed value based on the fiber composition, the acceptance angle varies for fibers operating in different media of different refractive index. An increase in refractive index of the surrounding medium corresponds to a decrease in the acceptance angle. The NA of a fiber is controlled by precisely doping the core and cladding slightly differently with impurities in order to control their refractive indices  $n_{core}$  and  $n_{clad}$ .<sup>51</sup>

Optical fibers are classified as single- versus multi-mode and step versus graded index. The difference between single-mode and multi-mode fibers is in the core diameter, which for single-mode fibers is about an order of magnitude larger than the wavelength of the detected light (typically 7-10  $\mu\text{m}$ ), while for multi-mode fibers it is much larger than the wavelength (typically on the order of tens or hundreds of micrometers).<sup>52</sup> This difference in core diameter translates to lower number of reflections and thus shorter path length for light traveling in single-mode fibers, which results in lower attenuation losses (due to absorption and scattering) and higher speed.<sup>51</sup> These properties are especially useful in telecommunications where longer transmission distances are involved. The larger diameter of multi-mode optical fibers on the other hand allows for more light to be collected, making these fibers more useful for short transmission distance applications and where higher SNR is required.

Optical fibers can also be classified in terms of the refractive index distribution in their composition as step index versus graded index.<sup>51</sup> The core and

cladding of step index fibers have uniform indices of refraction. The distance traveled by light rays traversing a step-index fiber at different angles relative to its axis is different, causing them to reach the receiving end of the fiber at different times in what is called modal dispersion. For telecommunication applications, this is an issue since a data pulse is spread out, requiring shorter pulses or lower pulse repetition rate (bandwidth) in order to avoid overlap between consecutive pulses. Graded index fibers, for which there is a negative gradient in the refractive index of the core from the fiber axis radially towards the cladding, eliminate this issue by modulating the speed of rays traversing the core at different angles to the axis (a smaller angle results in lower speed and vice versa). For spectrometry applications where pulse repetition rate is irrelevant, cheaper step index fibers may be used.

## **1.5 Thesis – motivation, objectives, organization**

### **1.5.1 Dosimetry**

All dosimeters currently employed for external beam radiation dosimetry must be directly irradiated by the beam. This results in two main issues:

- Perturbation of the radiation field by the presence of the detector in the field and
- Averaging of the reading over the finite volume of the detector.

The first issue deems necessary a conversion between the measured value and the actual dose at a measurement point in the reference material (phantom), which is achieved by applying conversion factors and measurement position shifts. Uncertainties in these conversion parameters affect the final dose value. To alleviate the second issue, dosimeters with small sensitive volumes must be used and areas of high dose gradients avoided when necessary. The size of detector volumes can be decreased only to a limit and high dose gradients are often inevitable, such as in measurements of electron beam PDDs (see Section 2.2 for definition), at the edges of lateral dose profiles (penumbrae), and in the many

cases involving treatment with small fields, such as in the case of stereotactic radiosurgery (SRS for short, a technique using many small beams focused on a small area) and IMRT. By developing a dosimeter which can be placed outside of the field, these issues can be minimized and potentially avoided altogether. Therefore, one aim of this work is to examine, by means of Monte Carlo simulation (see Section 2.4) and experimental measurements, the relationship between dose and Cherenkov emission produced by radiation beams in a reference medium (in this case water), and assess the potential application of Cherenkov emission in dosimetry.

Recent work has demonstrated correlation between Cherenkov emission and dose using a Monte Carlo generated spatially variant conversion factor to account for the angular anisotropy of the signal,<sup>32</sup> introducing a fluorescent dye into the phantom to resolve the angular anisotropy issue,<sup>33</sup> and through three-dimensional tomographic reconstruction of the dose distribution using a telecentric lens.<sup>34</sup> Further to these findings, this thesis investigates the dose versus Cherenkov correlation in depth through detailed Monte Carlo analysis and unveils a new method for two-dimensional correlation between dose and Cherenkov, using a fiber optic cable and a spectrometer and renouncing the need for a fluorescent dye or a conversion factor.

### 1.5.2 Imaging

As previously noted, most current techniques for tumor targeting and localization require the use of ionizing radiation, which increases patient radiation exposure. In addition, intensity modulation based on tumor microenvironment status (such as oxygenation information), in order to increase the tumor control probability, has not been implemented. The second goal of this work is, therefore, to demonstrate the feasibility of a new method based on spectral shifting of the Cherenkov emission produced by a radiotherapy treatment beam in a tissue-simulating phantom with the use of quantum dots (described in Section 2.3), and thus confirm its utility for the development of a new optical imaging modality for image guidance in radiotherapy. By modifying the surface specificity of the

wavelength-shifting species to incorporate tumor microenvironment reporters, such as oxygenation probes, ultimately online intensity-modulation can be implemented in radiotherapy based on tumor microenvironment information.

Thus far, fluorescent biomolecular probes, such as protoporphyrin IX,<sup>29</sup> PtG4<sup>35, 36</sup> and Cyto500LSS,<sup>37</sup> have been used to spectrally shift the blue-dominated Cherenkov emission from external radiotherapy treatment beams towards longer wavelengths in order to maximize tissue transmission and improve the potential tissue application of this effect to imaging during radiotherapy. This work proposes an alternative spectral shifting method using NIR-emitting zero-dimensional semiconductor nanostructures termed quantum dots (see Section 2.3).<sup>38</sup> The proposed method is successfully demonstrated via a NIR-shift of the Cherenkov signal from a clinical linac generated electron beam incident upon a tissue-simulating phantom using relatively inexpensive and ubiquitous CdSe-based core-shell quantum dots. For applications in biomedicine, a great advantage of quantum dots over alternative fluorescent probes is the opportunity to precisely and in a straightforward manner tune and control their optical and biochemical properties, which makes them especially applicable to targeting, localization and microenvironment sensing in radiotherapy. In addition, they are very photostable, exhibit narrow characteristic emission peaks,<sup>39, 40</sup> and are an ideal candidate for efficient excitation by the compatibly blue-dominated continuous Cherenkov emission spectrum. Another rationale for investigation into the imaging applications of quantum dots in radiotherapy is the possibility to modify their surface chemistry to incorporate oxygenation status reporters for Cherenkov-stimulated oxygenation sensing and beam modulation during radiotherapy.

### 1.5.3 Thesis organization

The following chapters outline in depth the theory behind each step of this work (Chapter 2), including simulation and experimental techniques and data analysis, the methods and materials employed (Chapter 3), and a detailed presentation and discussion of the results (Chapter 4). This is followed by a summary, conclusions and potential directions for future work (Chapter 5).

## Chapter 2

### RELEVANT THEORY AND BACKGROUND

#### 2.1 Cherenkov radiation

As previously described (Section 1.2), Vavilov-Cherenkov emission, typically called simply Cherenkov emission, is an optical signal resulting from de-excitation of an asymmetrically polarized dielectric medium traversed by a charged particle traveling faster than the phase speed of light in the medium.<sup>16</sup> This condition can be expressed as a threshold expression in terms of the particle's normalized velocity  $\beta$  and the medium's index of refraction  $n$  as shown in Equation 1.2. A straightforward way to explain Cherenkov radiation is through Huygens' principle<sup>17</sup>. Huygens' principle is a mathematical model for light propagation developed by the Dutch physicist Christiaan Huygens in the 17<sup>th</sup> century. It states that every point along the path of a light wave can be viewed as a source of a spherical 'wavelet' and the combination of wavelets from all points along the path reconstructs the total wave at every instance. The coherent Cherenkov signal is created by interference of light emitted at every point along

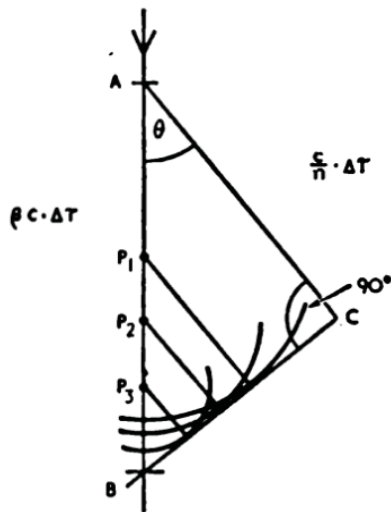


**Figure 2.1:** Huygens' principle description of the Cherenkov effect (adapted from Ref. 16).

the charged particle's trajectory (Figure 2.1). Constructive interference between light waves occurs at a maximum angle  $\theta_{max}$  relative to the particle's trajectory and the signal gradually decreases at larger and smaller angles due to destructive interference. This angle is dependent on the particle speed and the medium refractive index. Given initial and final charged particle positions A and B, a final radius AC of a wavelet emitted at A when the particle has reached B, and a time of travel  $\Delta T$  of both photon and charged particle, the lengths of the segments AC and

AB can be expressed as the product of  $\Delta T$  and the respective photon and charged particle velocities, expressed in terms of the speed of light in vacuum  $c$  and the medium index of refraction  $n$  and normalized particle velocity  $\beta$  respectively. The maximum angle therefore satisfies

$$\cos \theta_{max} = \frac{1}{\beta n}. \quad (2.1)$$

It is seen that  $\theta_{max}$  increases with the particle velocity and with the medium's refractive index. Therefore, Cherenkov is emitted along the surface of a cone, whose axis coincides with the particle trajectory. The Cherenkov radiation power  $\frac{dW}{dt}$  for a particle of charge  $e$  is given by the Frank-Tamm formula<sup>53</sup> (developed in 1937 by Ilya Frank and Igor Tamm) as

$$\frac{dW}{dt} = \frac{e^2}{c^2} \int_{\beta n > 1} \left(1 - \frac{1}{\beta^2 n^2}\right) \omega d\omega, \quad (2.2)$$

where  $\omega$  is the optical photon's angular frequency. The angular frequency  $\omega$  can be represented in terms of photon wavelength  $\lambda$  as<sup>17</sup>

$$\omega = \frac{2\pi c}{\lambda n}. \quad (2.3)$$

From Equations 2.2 and 2.3, it is evident that the Cherenkov emission intensity decreases for larger wavelengths, which explains its blue appearance despite the fact that it is a continuous emission spectrum. In Equation 2.2, it can also be seen that the intensity increases with particle velocity and with index of refraction. A detailed description of the Frank-Tamm formulation is provided in Ref. 16.

## 2.2 Ionization chambers

Ionization chambers are some of the most commonly used radiotherapy dosimeters. They measure the amount of ionization produced by the beam inside their sensitive volume, which can then be related to dose. The main components of an ionization chamber are a cavity (which is usually gas-filled, but can also be liquid-filled for special applications), a polarizing electrode, and a collecting

electrode.<sup>6</sup> A high voltage power supply provides an electric potential across the cavity between the electrodes. When the chamber is placed in a radiation beam, ions are created in the cavity and are attracted to the corresponding electrode. An electrometer attached to the chamber measures the amount of ions collected. The two most common types of ionization chambers are cylindrical (Figure 2.2) and parallel-plate chambers.

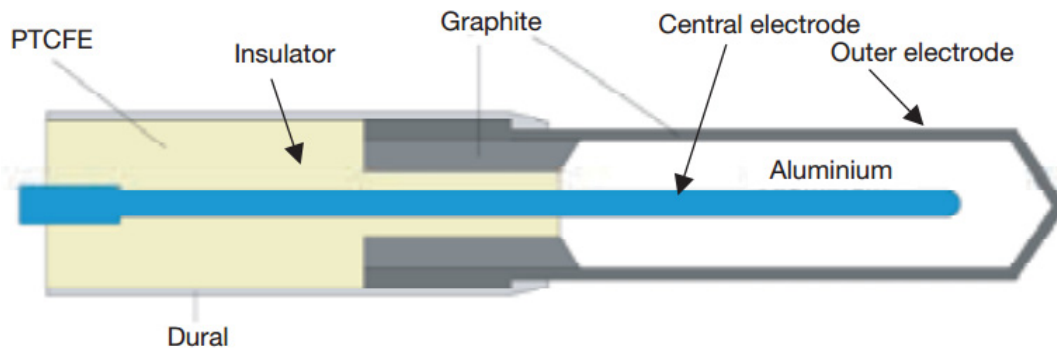


**Figure 2.2:** Basic design of a typical cylindrical ionization chamber for radiation dosimetry (adapted from Ref. 6).

Cylindrical chambers incorporate a central collecting electrode and a cylindrical polarizing electrode. Their sensitive volume, internal diameter and length are on the order of a fraction of a  $\text{cm}^3$ , a millimeter, and a centimeter respectively. Parallel-plate chambers, on the other hand, consist of parallel planar electrodes. Though the collecting electrode of an air-filled cylindrical chamber is along the central axis of the chamber, the effective point of measurement (the point to which the chamber measurement corresponds to) is upstream by a distance equal to the cavity radius multiplied by 0.5 and 0.6, respectively, for electron and photon beams.<sup>6</sup> This is a result of the fluence geometry and also the fact that secondary electrons produced by high-energy radiation beams are predominantly forward-directed and there is reduced attenuation in the cavity, which is filled with (low-density) gas, relative to the surrounding medium, which is usually water or a material of similar density. For parallel-plate chambers, the effective point of measurement is located at the upstream face of the cavity. Parallel plate chambers are generally smaller along the direction of the beam than

cylindrical chambers (i.e. their electrodes are closely spaced), which makes them better suited for measurements closer to the phantom surface. In general, ionization chambers are relatively cheap and energy independent and provide accurate and reproducible charge measurements. Some issues with ionization chambers are the need for application of various correction/conversion factors to their reading in order to account for any variation from the reference conditions in which they were calibrated and for their presence in the beam. In addition, ion chambers suffer from ion recombination issues, which are dose rate dependent, and voltage polarity dependence.

Many beam characteristics can be used to describe dose deposition by a particular beam. One of the most common beam qualifiers is the percent depth dose curve (PDD), which represents the dose behavior as a function of depth in an absorber, such as water. The PDD is a plot of dose versus depth, normalized to 100% at the depth of maximum dose  $z_{max}$ . The shape of the PDD is an important indicator of the relative dose deposition profile of a given beam quality (ex: penetrating versus non-penetrating, broad versus narrow). It is a function of many factors, such as the beam energy, field size, and source-to-surface distance (SSD). Typical PDDs in water for varying nominal beam energies at standard field size and SSD are shown in Figure 2.3. Electron beam PDDs feature (in order of

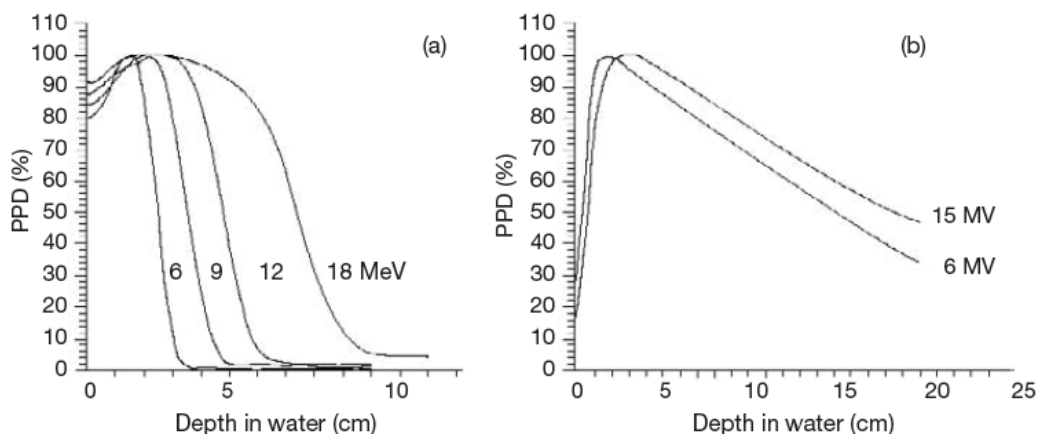


**Figure 2.3:** Typical electron and photon beam PDDs in water for varying nominal beam energies at standard field size and SSD (adapted from Ref. 6).

increasing depth) a surface dose, a region of buildup, a depth of maximum dose, a high negative dose gradient, and a bremsstrahlung tail. PDDs of photon beams produced by clinical linacs exhibit a lower surface dose, a larger buildup gradient, and a much slower dose drop-off following the depth of maximum dose. For this reason, linac-generated electron beams are much more suitable for treating superficial lesions.

### 2.3 Quantum dots

Nanometer-sized probes for biomedical applications have received a great deal of attention, because their biological, chemical and physical properties are unique and can be tuned by varying their characteristics, such as size, shape and impurities.<sup>38</sup> Quantum dots (QDs) are zero-dimensional nanostructures, meaning their size is on the order of nanometers in all three dimensions. QDs are well-suited for excitation by Cherenkov radiation, since both the QD absorption and Cherenkov emission spectra are continuous and increase towards the ultraviolet (UV) region of the electromagnetic spectrum. Special characteristics of QDs, making them attractive for applications in biomedicine, are the fact that they are photostable (i.e. they do not undergo a chemical change upon absorption of electromagnetic radiation), can be attached to important biomolecules for targeting and localization, and possess narrow, and therefore distinctive, emission profiles.<sup>39, 40</sup>

Due to the small size of QDs, electrons are spatially confined within the QD structure, which results in separation of the available energy states (quantum confinement). The valence energy band (range of states) represents the highest energy band in which electrons are still bound to the atom, while the conduction band corresponds to energies higher than the valence band and sufficient to free an electron from an atom and allow it to move freely within the atomic lattice of the material. The energy difference between the valence and conduction bands is the **band gap**. An electron and the positive site (known as a hole) left behind upon excitation from the valence to the conduction band via absorption of a photon form an electron-hole pair. The electron can subsequently de-excite from

the conduction band via emission of a photon. Since photons are absorbed/emitted upon excitation/de-excitation of an electron, the size of the band gap dictates the optical (absorption/emission) properties of a QD.<sup>38</sup> A diagram of the energy levels and band gaps of bulk materials, QDs, and molecules is shown in Figure 2.4. QDs are nanometer-sized in all dimensions and consist of hundreds of thousands of atoms; therefore, their optical properties are between those of bulk materials and single molecules.<sup>54</sup> Electrons of bulk semiconductors are not confined, and

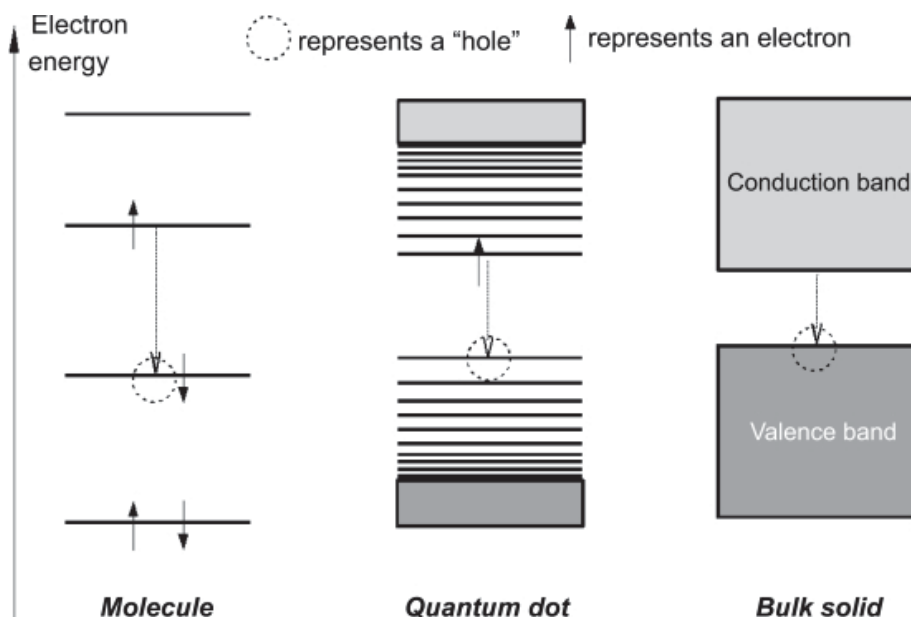


**Figure 2.4:** Energy level diagram of molecules, quantum dots, and bulk semiconductors (adapted from Ref. 54).

therefore their energy bands are continuous. Single molecules/atoms, on the other hand, exhibit fixed discrete energy levels, called orbitals, with a gap defined by the highest occupied molecular orbital and the lowest unoccupied molecular orbital (HOMO-LUMO gap). Due to the small physical size of QDs, QD electrons are confined, which leads to a larger band gap than that of bulk materials and the emergence of discrete energy levels. Since electron confinement, and therefore the band gap size, is governed by QD size and since the band gap determines the optical properties of the QD, the optical properties can be tuned by modifying the QD size. In general, the band gap and therefore the mean emission photon energy increase with decreasing QD size.

The surface chemistry of QDs can be modified based on the desired application (Figure 2.5a). For example, a hydrophilic or hydrophobic ligand may be added to achieve a colloidal suspension or a ligand may be added with specific affinity to a particular atom or molecule of interest, such as oxygen species.<sup>38</sup> Fluorescence occurs via electron excitation by a photon and consequent de-excitation via emission of a photon at a longer wavelength. This is possible because within an energy band, de-excitation can occur via non-radiative pathways, such as vibrational relaxation, lowering the electron's energy. De-excitation from the conduction to the valence band, however, can also occur via non-radiative pathways, decreasing the emission quantum yield. The quantum yield can be improved by growing a shell around the QD of a material with a larger band gap (Figure 2.5b), which passivates the non-radiative recombination states by creating a potential barrier around the core due to the energy band offset and confining the excited electron-hole pair within the core.<sup>38</sup> Shells also serve to

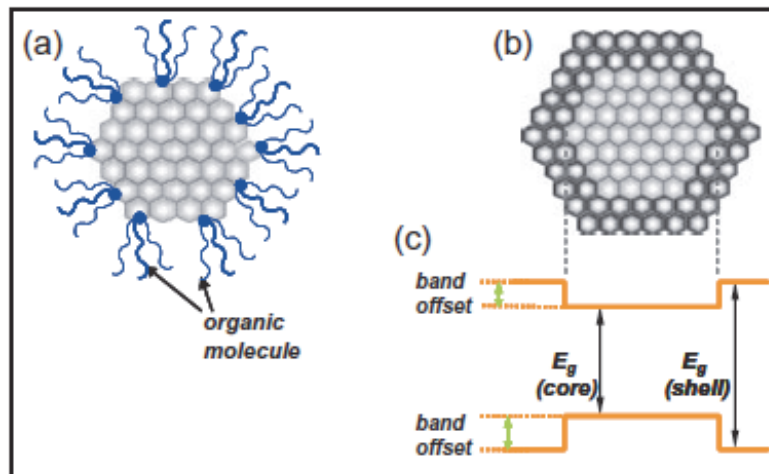


**Figure 2.5:** Simplified drawing of (a) a quantum dot surface-modified with an organic ligand, (b) a typical core-shell quantum dot, and (c) an energy level diagram of a typical core-shell quantum dot (adapted from Ref. 38).

protect QDs and improve their surface modularity. In many cases, core-shell QDs are also surface-modified with an organic ligand to improve solubility and allow for bio-conjugation.

An informative quantitative visual representation of the relationship between band gap and quantum dot size is a diagram of band gap versus lattice constant of known semiconductors (Figure 2.6).<sup>55</sup> The lattice constant is a quantity representing the distance between atoms in a crystal lattice. The colored stripes in Figure 2.6 represent the optical wavelengths corresponding to each band gap that falls in the visible region of the electromagnetic spectrum. The CdSe/ZnS quantum dots used in this work consist of a CdSe core coated with a larger-bandgap ZnS shell. The large band gap difference between ZnS and CdSe provides for very good passivation of non-radiative recombination states. In addition, the relatively small difference between the lattice constants of CdSe and

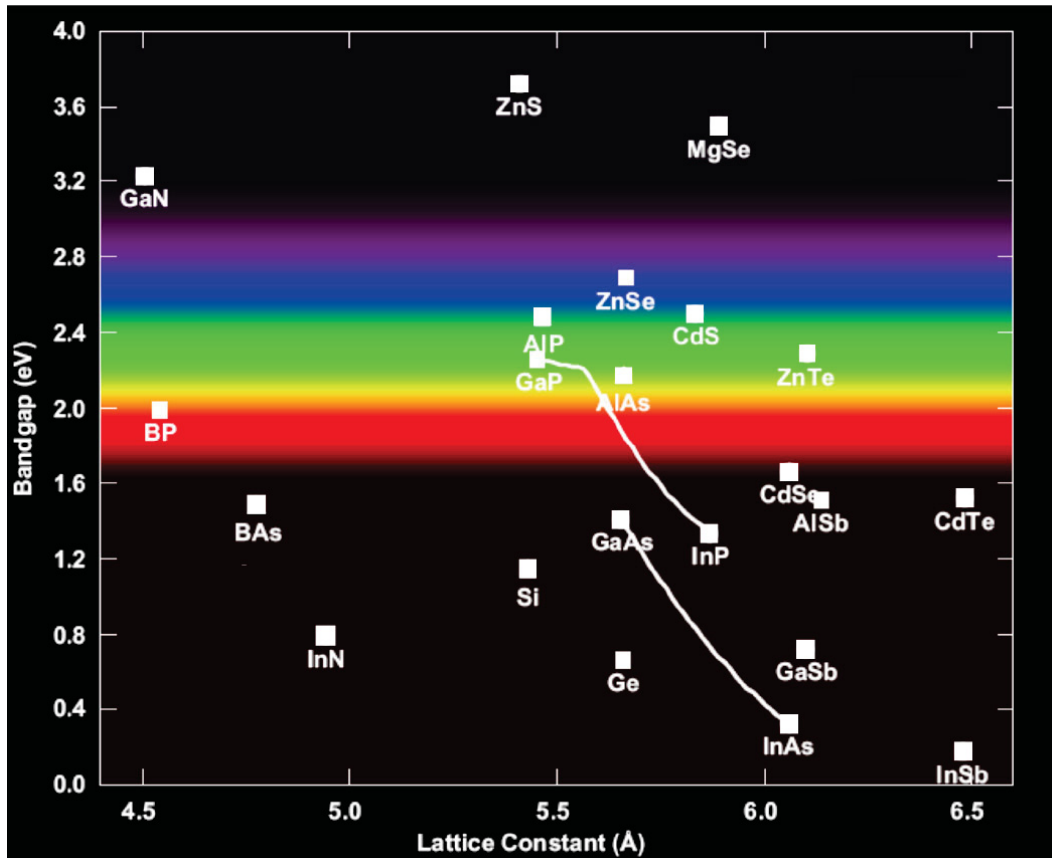


**Figure 2.6:** Diagram of band gap versus lattice constant for a number of semiconductors (adapted from Ref. 55).

ZnS minimizes the effects of core-shell lattice mismatch, which reduces quantum yield by introducing defects at the core-shell interface.

## 2.4 Monte Carlo technique

Monte Carlo (MC) is an exceptionally robust and versatile computational technique used to solve high-dimensional (i.e. involving many coupled degrees of freedom) macroscopic problems in many fields from atomic physics to astronomy to finance. Stochastic physical and mathematical effects are simulated by repeatedly sampling their probability distributions using random numbers.<sup>56, 57</sup> The technique can be applied to modeling radiation transport by quasi-randomly creating particle trajectories based on sampling the probability of occurrence of various physical phenomena (ex: scattering) at each **step** along the particle trajectory and sampling the probabilities of the outcomes of these phenomena (ex: resultant particle direction) in a defined geometry. This sampling can be limited by user-specified criteria, such as inclusion of only particular physical interactions or limits on the step length. High-dimensional physical problems are solved by creating and simulating the trajectories of a large number of primary particles (called **events**). In this way, one can simulate macroscopic effects, such as dose deposited by a radiation field or Cherenkov emission signal collected by a detector, with the result limited by uncertainty based on the number of events (proportional to the inverse square root of the number of events). The MC technique can be implemented in various ways, ranging from general-purpose low- or intermediate-level programming languages, such as C++, to very high-level languages, such as MATLAB®, to software applications, such as Excel.

Over the last few decades, there has been a remarkable increase in the use of MC techniques to simulate macroscopic effects of treatment beams in radiotherapy.<sup>58</sup> MC techniques have found many applications in radiotherapy, including patient treatment planning and ion chamber measurement correction factor calculations. General-purpose MC software packages for the transport of radiation have become widely available and include EGSnrc (Electron Gamma Shower National Research Council),<sup>59, 60</sup> PENELOPE (Penetration and ENergy

LOss of Positrons and Electrons),<sup>61</sup> MCNP (Monte Carlo N-Particle),<sup>62</sup> and Geant4 (GEometry ANd Tracking),<sup>63</sup> with EGSnrc, a radiation transport package developed by the National Research Council of Canada, being the most widely implemented.<sup>58</sup>

The fact that the MC technique is extremely robust and versatile comes at the price of a slow convergence rate (proportional to the inverse square root of the number of simulated events).<sup>56</sup> However, partially owing to the steady increase in computing power, accompanied by a decrease in cost, and partially facilitated by novel computing techniques, such as the concurrent use of many CPUs and the development of fast calculation algorithms, has made MC much more applicable to essential radiotherapy problems, such as patient treatment planning.<sup>58, 64</sup> For a detailed account of MC theory, the reader is referred to Refs. 56 and 57.

For the purposes of this study, the Geant4 simulation toolkit<sup>63</sup> was used to create a Cherenkov emission software simulator for computer analysis of the correlation between radiation dose and Cherenkov emission, optimization of the measurement setup, and prediction of experimental results. Geant4 is a modular toolkit written in C++,<sup>a</sup> meaning it is made of individual modules of structured code that can be pieced together to form a complete program. In addition, the user can add his/her own code to a program. The structure of Geant4 is hierarchical. Geant4 components are grouped into 17 class categories linked by coherent interfaces, some of which include, but are not limited to, Geometry, Material, Particle, Processes, Tracking, Visualization, etc.

When building a Geant4 application, the user must write his/her own main() program and define 3 mandatory user classes. The main() program must instantiate the G4RunManager class, which controls the flow of the program and manages initialization and event loops, and all user-defined classes. The main() program must also pass pointers of the user-defined classes to the G4RunManager object and obtain a pointer to the user interface manager, G4UImanager, to allow

---

<sup>a</sup> Readers unfamiliar with C++ are referred to C++ Primer by Stanley B. Lippman, Josée Lajoie

the user to issue commands to the program from the command line. Other manager classes, such as those for visualization (G4VisManager), can also be instantiated and initialized in the main(). The 3 mandatory user-defined classes are G4VUserDetectorConstruction, in which the simulation geometry and materials are defined, G4VUserPhysicsList, which must include all particles and physics processes to be simulated, and G4VUserPrimaryGeneratorAction, where primary particles and their initial properties are defined. There are 5 optional user action classes, which contain methods whose default implementations (provided by Geant4) can be overridden to allow control over various stages of the simulation. These are G4UserRunAction, G4UserEventAction, G4UserStackingAction, G4UserTrackingAction, and G4UserSteppingAction. A **run** of a simulation consists of a sequence of events. Each **event** represents a primary particle and its effects. A primary particle moves through the simulation geometry in **steps**, whose length is chosen as the smallest of all proposed step lengths by physical processes included in the simulation, based on the interactions they entail, and by the distance to the next volume boundary. Before, during and after each step, secondary particles are generated when applicable. Particles are **tracked** one by one during a simulation. All particles are placed in what is called a **stack** when they are created and they are handled in a 'last in first out' fashion. The G4UserStackingAction class, which is an integral part of the Cherenkov emission simulator designed in this work, can be used to access particles in the stack. As an example of a Geant4 simulation, Figure 2.7 provides an OpenGL visualization of the simulation of 5 18 MeV positrons incident on a  $4 \times 4 \times 4 \text{ cm}^3$  block of water. In Geant4, the default colors for neutral, positively and negatively charged particles are green, blue and red, respectively, and can be changed as desired.

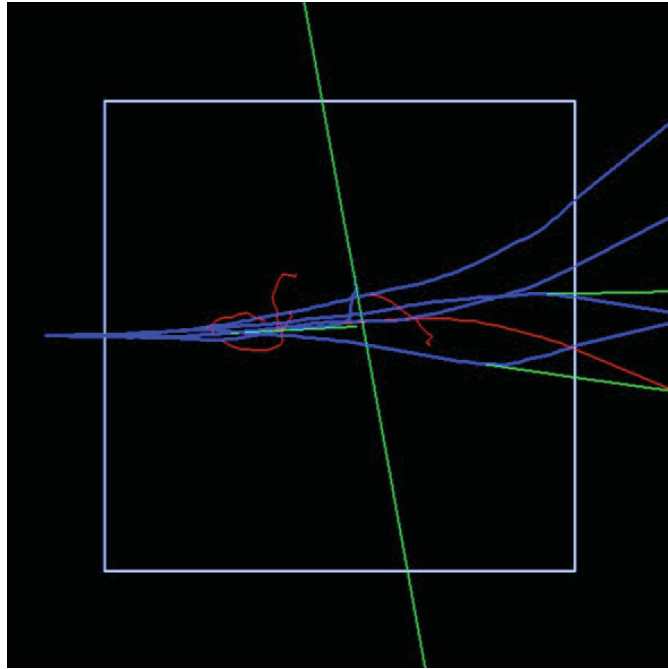


**Figure 2.7:** Geant4 simulation of 5 18 MeV positrons incident on a  $4 \times 4 \times 4 \text{ cm}^3$  block of water. Blue, red and green correspond to positive, negative and neutral particles. The OpenGL driver was used for visualization.

Geant4 provides methods for retrieval and scoring of useful information from a given simulation, although the user must usually add his/her own code to implement these methods. Scoring can be done by (1) calling built-in methods for obtaining track information in a user action class, such as `G4UserStackingAction`, (2) executing built-in commands in the command line during a simulation, (3) accumulating scores in the tracking volume via a user-defined scoring class, and (4) assigning a `G4VSensitiveDetector` object to a volume, through which event/run summaries can be obtained. Only the first two of these scoring methods (user action and command-based) are employed in the current work. User action scoring requires the most coding, but is the most straightforward method of obtaining useful information from a simulation. Methods provided by Geant4, such as `GetMomentum()`, can be called to retrieve simulation information. Command line scoring involves the built-in **scoring mesh** made up of scoring bins in which common physics quantities (such as dose) can be scored by typing appropriate commands into the command line. Since this functionality is still in its

preliminary development stage, it allows for very general and simple scoring geometries and it is relatively slow. Therefore, in this thesis a scoring mesh is used for only the most basic analysis of the Cherenkov effect, while for simulation of the relatively complex experimental setup, scoring is hard-coded in a `G4UserStackingAction` class. Development and implementation of the Cherenkov emission simulator of this thesis is described in detail in Section 3.1.2.

## 2.5 Statistical data analysis

### 2.5.1 Mean, median, mode and standard deviation

Mean, median, mode and standard deviation are important single-value descriptors of frequency distributions of sampled values of a variable.<sup>65</sup> The **mean** is the average value of the distribution, the **median** is the middle value – that is, there is an equal number in the distribution of higher and lower values than the median – and the **mode** is the most frequently occurring value. The **standard deviation**  $\sigma$  of a distribution of sampled values of a variable is a measure of the degree of spread of the values. It is defined as

$$\sigma = \sqrt{\frac{\sum_{i=1}^n (x_i - \bar{x})^2}{n - 1}}, \quad (2.4)$$

where  $n$  is the number of values,  $x_i$  is a particular value and  $\bar{x}$  is the mean of the distribution. A symmetrical distribution has equal mean and median, while a unimodal (meaning it is highest in the middle) symmetrical distribution has equal mean, median and mode. For a skewed distribution (leaning towards one side), on the other hand, the mean, median and mode will generally be all different. In general, the mean and standard deviation are used to represent the tendency and spread of a data set; however, in cases where the data set is not symmetrical, other descriptors may be more appropriate. For example, if the data features outliers (points which are much larger/smaller than the rest), the mean may be swayed towards the outliers and therefore the median or mode may better represent the distribution.

### 2.5.2 The normal probability distribution

The **normal probability distribution** (Figure 2.8), also called the bell curve or Gaussian distribution, is an important statistical function representing a frequency distribution of values of a single variable of interest.<sup>65, 66</sup> The normal distribution is important because it is resembled by distributions of many natural phenomena, many statistical inference procedures for data analysis assume the data set is sampled from a normal distribution, and the normal distribution is often used as a

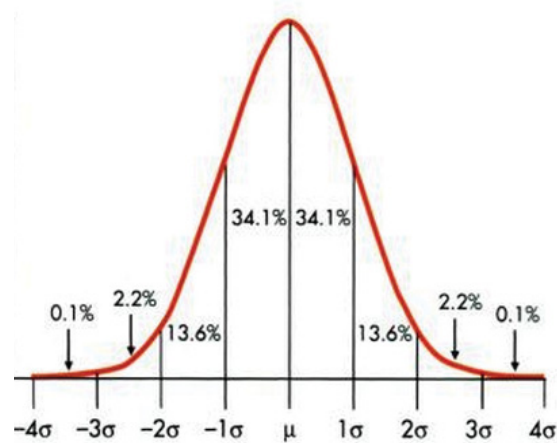


**Figure 2.8:** The normal probability distribution (adapted from Ref. 65).

reference for comparison of other distributions.<sup>65</sup> It is symmetrical, unimodal and asymptotic (it approaches zero towards infinity but never actually reaches it). Another important characteristic of the normal distribution is that, since it is symmetrical, its mean, median and mode are equal. In addition, 68.3%, 95.5% and 99.7% of the area under the normal curve fall within  $\pm 1$ ,  $\pm 2$  and  $\pm 3$  standard deviations from the mean respectively. Dividing the normal distribution into areas based on percentiles and the standard deviation provides a standardized straightforward method for determining in which portion of the curve a value is located and thus what is its approximate probability of occurrence. The normal distribution function  $f(x)$  is<sup>67</sup>

$$f(x) = \frac{1}{\sigma\sqrt{2\pi}} e^{-\frac{(x-\bar{x})^2}{2\sigma^2}}. \quad (2.5)$$

A special standardized case of the general normal distribution is the **standard normal probability distribution**, for which  $\bar{x} = 0$  and  $\sigma = 1$ .<sup>67</sup> An important quantity associated with normal distributions is the  $z$  score of a value in the distributions, which represents the distance of a value from the mean in standard deviation units (i.e. in number of standard deviations). The  $z$  score is defined as

$$z = \frac{x - \bar{x}}{\sigma}. \quad (2.6)$$

The  $z$  score allows to determine in which area of the curve a value is located. For the standard normal distribution, this expression reduces to

$$z = x. \quad (2.7)$$

Therefore, the values and  $z$  scores of the standard normal distribution are equivalent.

### 2.5.3 Quantile-quantile plots

A quantile-quantile plot, or **Q-Q plot**, is a graphical technique used to compare two probability distributions.<sup>68</sup> A **quantile**  $Q(f)$  is a value of a distribution that divides the distribution in two and is specified based on the fraction  $f$  of values of the distribution that are lower than the quantile. For example,  $Q(0.25)$  represents a value below which is 25% of the area of the distribution and above which is 75% of the area. If both distributions have the same number of data points, a Q-Q plot is created by sorting the values of each distribution in ascending/descending order and plotting the resulting ordered distributions against each other. If the plot is linear, the two distributions are of similar shape with the intercept and slope disclosing the difference in position and scale between the distributions respectively. Often, Q-Q plots are used to compare a data set with a theoretical distribution, such as the standard normal probability distribution, in which case they are called normal probability plots. A **normal probability plot** for a data set  $x(i)$  of  $n$  number of values is generated as follows:<sup>69</sup>

1. The values of the data set under study are sorted in ascending order;

2. The quantiles  $q(i)$  (i.e. z scores) corresponding to fractions  $f(i)$  are obtained from the standard normal probability distribution, where

$$f(i) = \frac{i - 0.5}{n}; \text{ and} \quad (2.8)$$

3. The sorted values  $x(i)$  are plotted against  $q(i)$ .

Equation 2.8 divides the standard normal distribution into  $n$  equal areas, assigns each value of the ordered set  $x(i)$  to a corresponding area in ascending order, and assumes that if  $x(i)$  was sampled from the standard normal distribution, each  $x(i)$  divides its corresponding area in half. Therefore, the number of values in the data set is important for adequate Q-Q analysis. A large number is preferable. Normal probability plots are useful for testing normality of a distribution and their shape reveals information about the shape of the distribution being investigated relative to the normal distribution (longer/shorter tails, symmetric/asymmetric, etc.).<sup>68</sup>

#### 2.5.4 Pearson and Spearman correlation coefficients

Numerous methods for examining the correlation between two variables have been developed.<sup>66</sup> Different techniques are suited to different applications based on the type of information sought after. In general, a basic single-value measure of correlation, called a **correlation coefficient**, is sufficient. Two of the most common types of correlation coefficient are the **Pearson product-moment and Spearman rho correlation coefficients**. Values of these coefficients are in the range of -1 to +1, where -1 indicates perfect negative (one variable increases as the other decreases) correlation, 0 indicates no correlation and +1 indicates perfect positive (one variable increases with the other) correlation. The stronger the correlation is, the closer the value of the correlation coefficient will be to -1 or +1, depending on the direction of the correlation. Both data sets must have an equal number of values. The Pearson correlation coefficient  $r$  is used to assess if the relationship between two data sets is linear. It is calculated as<sup>66</sup>

$$r = \frac{\sum_{i=1}^n ((x_i - \bar{x})(y_i - \bar{y}))}{\sqrt{\sum_{i=1}^n (x_i - \bar{x})^2 \sum_{i=1}^n (y_i - \bar{y})^2}}, \quad (2.9)$$

where  $n$  is the number of values in the data sets,  $x_i$  and  $y_i$  are the two data sets, and  $\bar{x}$  and  $\bar{y}$  are the means of the data sets. The Spearman correlation coefficient, on the other hand, relays information about the monotonicity of the variables. A monotonic correlation means the two variables always increase together or one variable always increases as the other decreases. The Spearman correlation coefficient is calculated by first ranking each data set by assigning a rank between 1 and  $n$  to each value based on its magnitude, 1 corresponding to the smallest value and  $n$  corresponding to the largest. In the case of equal values, their rank is the mean of the ranks if they had been ranked sequentially. For example, if the data contains four 5s, which are 1<sup>st</sup>, 2<sup>nd</sup>, 3<sup>rd</sup> and 4<sup>th</sup> in the sorted data, their ranks are all 2.5. The difference  $d$  between ranks of corresponding values is then calculated and the Spearman correlation coefficient  $\rho$  is calculated as<sup>66</sup>

$$\rho = 1 - \frac{6 \sum_{i=1}^n (d_i^2)}{n(n^2 - 1)}. \quad (2.10)$$

The main difference in the application of the two correlation coefficients is that data sets can be monotonic without being linear. Data sets can never be linear without being monotonic, however, and therefore a strong Pearson coefficient always implies a strong Spearman coefficient.

## Chapter 3

### MATERIALS AND METHODS

---

#### 3.1 Computer simulation

##### 3.1.1 Simulations

A Cherenkov emission software simulator was designed in order to perform a preliminary evaluation of the correlation between Cherenkov emission and dose, optimize the acquisition setup, and generate expected results in experimental conditions. The simulator was designed with Geant4 (for GEometry ANd Tracking 4), which is a C++ software simulation toolkit for the passage and interaction of particles with matter, based on the Monte Carlo method (See Section 2.4) and developed and maintained by the Geant4 Collaboration, which includes, but is not limited to, CERN, SLAC, Fermilab, and TRIUMF.<sup>63</sup> Geant4 provides a flexible framework of classes and methods for simulating experimental conditions, such as detection geometry, particle properties, physics processes, etc. A  $10 \times 10 \times 10 \text{ cm}^3$  (for the preliminary analysis) or  $40 \times 40 \times 40 \text{ cm}^3$  (similar to experimental conditions) block of water in air was simulated and all relevant physics processes (including electromagnetic processes and optical processes, such as Cherenkov emission) were included in the simulation. The radiation beam incident on the water comprised high-energy ionizing particles (typically 6-18 MeV electrons). By creating and processing a large number of **events** (individual primary particle trajectories and effects), the stochastic nature of particle interactions combines to simulate the deterministic effect of the beam. Quantities of interest, such as dose deposition and number, location and direction of Cherenkov photons, were scored in the water phantom and recorded for analysis. The main simulations carried out are the following:

1. Dose deposited and number of Cherenkov photons emitted in all voxels of a scoring mesh by an electron beam incident on the water tank;

2. Angular distribution of Cherenkov photons produced in the phantom with a beam incidence angle for which the maximum of Cherenkov emission is horizontal;
3. Number of Cherenkov photons collected by an optical fiber centered with respect to the field, positioned at the edge of the field at increasing depths in water, and parallel to the surface on which the beam is incident; and
4. Variation of signal collected with 1 centered fiber positioned at the edge of the field versus 1 fiber offset laterally (along the edge of the field at the same depth) by 1 cm.

For Simulations 3 and 4, the beam incidence angle was chosen such that the fiber direction was almost equal to the expected direction of maximum Cherenkov emission, respecting experimental setup limitations, such as the need to avoid beam incidence through the side of the water tank, which would perturb the field. The chosen angle between the beam central axis and the incidence surface normal was  $47^\circ$  (see Figure 3.4). This value was chosen based on the aforementioned setup limitations and the Cherenkov angular distribution analysis. As in experiment, the source-to-surface distance (SSD) was set to 110 cm for normal incidence and a field of  $6 \times 6 \text{ cm}^2$  at a distance of 100 cm from the source was used. The beam was assumed to be monoenergetic of energy 5.5, 11.5 or 17.5 MeV at a distance of 10 cm from the surface to account for the contribution of low-energy scatter electrons produced in the gantry head components.<sup>6</sup> The setup parameters used in Simulations 3 and 4 are listed in Table 1.

**Table 1:** Setup parameters used in Simulations 3 and 4.

Beam type	Beam energy at 10 cm from surface	Incidence angle relative to normal	SSD at normal incidence	Field size at SSD = 100 cm	Water tank dimensions
electrons	5.5, 11.5, 17.5 MeV	$47^\circ$	110 cm	$6 \times 6 \text{ cm}^2$	$40 \times 40 \times 40 \text{ cm}^3$

The purpose of Simulation 1 was to carry out a preliminary investigation of the correlation between dose deposition and Cherenkov emission in order to

confirm that an in-depth investigation is justified. Simulation 2 revealed the expected variation of the signal with respect to angle, which is useful for optimization of the measurement setup. Simulation 3 provided an expected signal for comparison with measurements. For experimental measurements, 2 fibers were used in order to maximize the signal-to-noise ratio. One fiber was centered with respect to the field and one was offset laterally by 1 cm along the field edge at the same depth. The aim of Simulation 4 was to ensure that no variation exists in the signal detected with each fiber.

### 3.1.2 Geant4 Cherenkov simulator design

In the design of the Cherenkov emission simulator, implementation details of the main() program, mandatory user-defined classes G4VUserDetectorConstruction, G4VUserPhysicsList and G4VUserPrimaryGeneratorAction, as described in Section 2.4, and the user action class G4UserStackingAction, essential for retrieving scoring information from the simulation, are described below.

#### ***The main() program***

The G4RunManager class and all user-defined initialization and action classes were instantiated in the main() program and a pointer to G4UImanager was created as required by the program. In addition, for cases when visualization was necessary, G4VisManager was instantiated and initialized, and for cases when scoring was to be performed with a scoring mesh, a G4ScoringManager was created. For the preliminary dose versus Cherenkov analysis, a scoring mesh of  $0.5 \times 0.5 \times 0.5 \text{ cm}^3$  bin size was overlaid precisely over the water tank geometry and used to score the dose distribution and the distribution of Cherenkov photons emitted in all directions. Scored radiation dose and Cherenkov photon data were dumped into a text file for subsequent quantitative analysis of the correlation. Visualization was disabled in this case to speed up the simulation, though a representative image of slices of a scoring mesh of  $0.5 \times 0.5 \times 0.5 \text{ cm}^3$  bins, in which dose was deposited by a simulated 18 MeV electron beam (made up of 200

particles) of field size  $6 \times 6 \text{ cm}^2$  at 100 cm SSD, incident on a  $10 \times 10 \times 10 \text{ cm}^3$  block of water, is given in Figure 3.1.

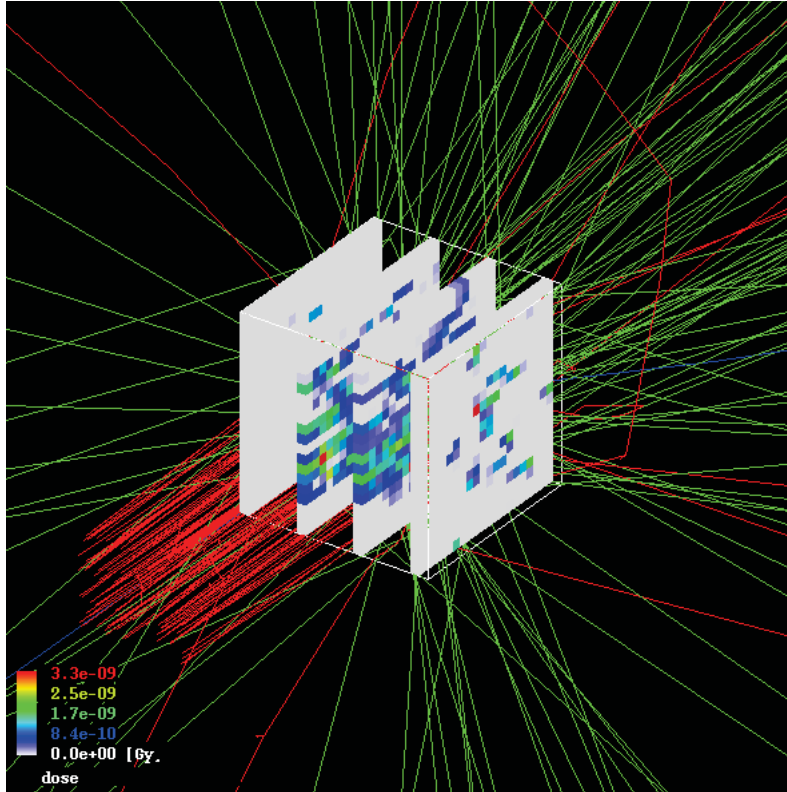


**Figure 3.1:** Slices of dose distribution scored in Geant4 with a  $10 \times 10 \times 10 \text{ cm}^3$  scoring mesh of  $0.5 \times 0.5 \times 0.5 \text{ cm}^3$  bins, deposited by a simulated 18 MeV electron beam (made up of 200 particles) of field size  $6 \times 6 \text{ cm}^2$  at 100 cm SSD, incident on a  $10 \times 10 \times 10 \text{ cm}^3$  block of water. The OpenGL driver was used for visualization.

### ***G4VUserDetectorConstruction***

In the detector construction class, the dimensions and positions of the experimental hall ( $2 \times 2 \times 2 \text{ m}^3$ ) and the water tank ( $40 \times 40 \times 40 \text{ cm}^3$ ) were set, the materials of which they were composed (air and water) were defined, and properties, such as index of refraction and absorption (as discrete functions of photon energy), were input and assigned to their corresponding volume. The coordinate center and coordinate axes of the water tank coincided with those of the experimental hall for ease of design of complex components of the program.

### ***G4UserPhysicsList***

The physics processes defined in the user physics list class include Cherenkov, scintillation, absorption, Rayleigh and Mie scattering, boundary processes, decay processes, and electromagnetic processes, such as Compton scattering. Methods were included for the construction of bosons, leptons, mesons and baryons, all of which were accessed through the G4ParticleDefinition class. Secondary particle production cuts, which are thresholds for secondary particle energy below which particles are no longer produced, were set to the Geant4 default of 0.7 mm. Low-energy thresholds are indispensable in Monte Carlo physics simulations as tracking all particles down to zero energy is impractical.

### ***G4UserPrimaryGeneratorAction***

In the primary generator user action class, a G4GeneralParticleSource object was instantiated, which allows for command-line control of the primary particle properties. The beam could therefore be defined in a macro file (a file of input commands executed together) executed in the main() program. Characteristics of the beam, such as energy, direction, field size, divergence, incidence angle, etc. could be controlled from the command line, allowing for a quasi-realistic simulation of the clinical linac beam used in the experiments. The simulated beam comprised of a  $6 \times 6 \text{ cm}^2$  square source of 5.5, 11.5 or 17.5 MeV mono-energetic electrons with an isotropic angular distribution limited by the calculated beam divergence angle of the experimental beam (see Figure 3.4 below, divergence half angle =  $\sim 2^\circ$  for a field of  $6 \times 6 \text{ cm}^2$  at an SSD of 100 cm). The distance between the square source and the water surface was set to 10 cm for normal incidence to simulate the SSD of 110 cm used in experiments. The beam angle was adjusted by varying the square source rotation and angular distribution direction.

### ***G4UserStackingAction***

The user stacking action class was critical to realization of the objectives of this work. In the stacking action class, integer and floating-point value arrays were initialized to store spectral and angular distribution data of optical photons, fiber

position and number of photons collected by the fiber. The `ClassifyNewTrack()` method of this class is called every time a new particle is created (i.e. every time a particle is placed into the stack). In the implementation of this method in the present work, each time a particle was placed into the stack, it was classified as an optical photon or not. If it was found to be an optical photon, its coordinates in the global coordinate system were used to calculate its position relative to the fiber's acceptance cone. In addition, its momentum direction and magnitude were used to calculate its direction relative to a vector connecting its position to the fiber tip. These calculations were performed for all fiber depths of interest. The output of this simulation was a distribution of fiber counts versus fiber depth, which was compared to experimental results under the same conditions. In addition, photon energies and angles of emission were accessed in order to generate optical wavelength distributions (i.e. optical spectra) and angular photon emission distributions via a simple iteration loop that allowed control over wavelength and angle resolution and range. Results of this simulation were output to a text file for analysis of the emission spectra and emission angular distributions, which were used for optimization of the experimental setup. Analysis of the variation in the signal between 1 and 2-fiber detection, described below, was achieved by adjusting the fiber position in the user stacking action class.

### **3.2 Phantoms**

The phantoms used in the experiments were a  $40 \times 40 \times 30$  cm<sup>3</sup> water tank and a tissue-simulating phantom made of water (for radiological equivalency to tissue) and 0.1% v/v or less Intralipid® (to simulate the scattering properties of tissue) and defibrinated beef blood (to simulate the absorption properties of tissue).<sup>70</sup> A representative photo of a tissue-simulating phantom is shown in Figure 3.2.

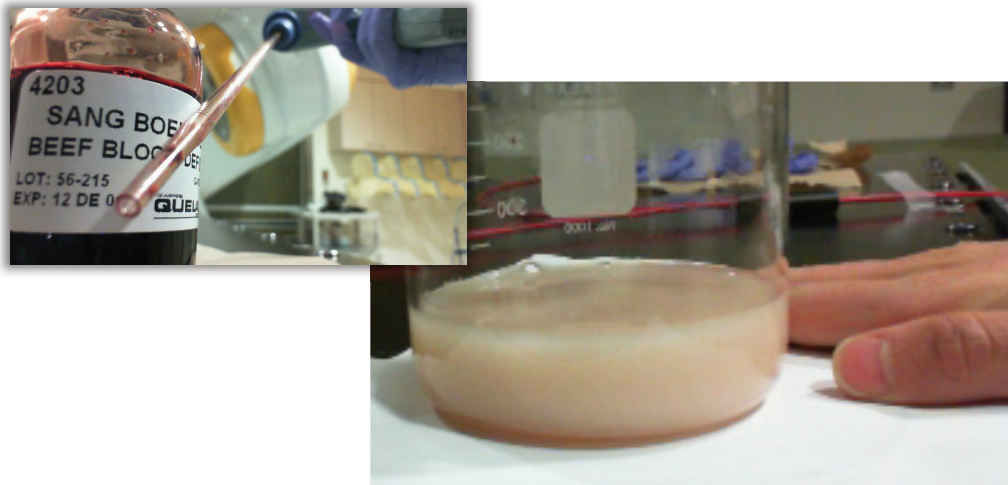


**Figure 3.2:** Jar of beef blood (top left) used in preparation of tissue-simulating phantoms and a representative image of a tissue-simulating phantom used in the Cherenkov NIR shift experiments.

### 3.3 Detector system and setup

All experiments were performed with a Novalis Tx™ linear accelerator, manufactured by Varian Medical Systems, Inc. (Palo Alto, CA, USA) and Brainlab AG (Feldkirchen, Germany), situated in the Department of Radiation Oncology at the Montreal General Hospital, Montreal, Canada. It provides nominal photon beam energies of 6 and 18 MV and nominal electron beam energies of 4, 6, 9, 12, 15, and 18 MeV. Due to the lengthy process involved in experimental measurement of Cherenkov emission, it was only carried out with the 18 MeV electron beam, while dose measurements were carried out for the 6, 12 and 18 MeV electron beams. An electron beam applicator cone was attached to the gantry to reduce beam spread in air due to scatter. The linac gantry was rotated to an angle of  $47^\circ$  with respect to the vertical, such that if the fiber is horizontal, the direction of maximum Cherenkov emission was almost aligned with the axis of the fiber. The reason the alignment was intentionally made slightly offset is that perfect alignment would require a portion of the beam to enter the water through the side of the tank, perturbing it. The tank's dimensions were slightly too small. For the dose versus Cherenkov measurements, the SSD was set to 110 cm at a gantry angle of  $0^\circ$  (vertical beam), which translated to a SSD of 114 cm at the gantry angle of  $47^\circ$  used for the measurements, since the linac **isocenter** (around which the linac rotates) is located at 100 cm from the

source. A square field size of  $6 \times 6 \text{ cm}^2$  at 100 cm from the source was used. The measurement setup parameters are provided in Table 2.

**Table 2:** Experimental setup parameters.

Beam type	Beam nominal energy	Incidence angle relative to normal	SSD at normal incidence	Field size at SSD = 100 cm	Applicator cone
electrons	6, 12 or 18 MeV	$47^\circ$	110 cm	$6 \times 6 \text{ cm}^2$	yes

### 3.3.1 Dose measurement setup

Dose was measured in the water tank with an Exradin A12 waterproof cylindrical ionization chamber (collection volume =  $0.64 \text{ cm}^3$ ) in a holder attached to the water tank and incorporating a manual depth position control knob. The ion chamber was attached to a Keithley Instruments Inc. electrometer, placed outside of the linac room. The ion chamber and electrometer have been calibrated together in accordance with standard protocol. The chamber readings were acquired along the beam axis (at a  $47^\circ$  angle with respect to the vertical), converted to dose measurements according to the procedure outlined in the report of AAPM Task Group 70 on clinical electron beam dosimetry (Gerbi et al. 2009), and normalized to 1 at the position of maximum dose to generate beam-axis PDD curves.

In order to precisely control the chamber position, the *zero* position was first set as follows: The chamber's central axis was first aligned at the water surface by using the position control of the chamber holder to slowly move it upwards from below the surface until its reflection in the surface and its submerged portion seem to make up a chamber of the same proportions. This positioning procedure is necessary in order to avoid meniscus effects, which would be present if the chamber was lowered into the water from above. After rotating the gantry to  $47^\circ$  relative to the vertical, the center of the chamber was aligned at the center of the field, located with the linac's field light and cross hairs, by using the lateral and longitudinal treatment couch position controls. The

couch lateral position displayed on the console and the depth position indicated on the chamber holder display were noted as the zero position.

Readings were taken at 1 cm depth intervals along the beam axis by moving the chamber vertically with the chamber holder control and laterally with the couch lateral position control. Desired positions were calculated relative to the zero position and based on the beam axis angle of  $47^\circ$ .

### 3.3.2 Optical measurement setup

Due to the lengthy process involved in experimental measurements with the optical equipment available for this project, optical measurements were only carried out for the 18 MeV electron beam. The optical signal was acquired with a bifurcated (for higher signal) fused-silica multi-mode step-index fiber optic cable (Delta Photonics, Ottawa, Canada) of core diameter = 400  $\mu\text{m}$ , length = 2 m, and NA = 0.22, resulting in acceptance angle =  $9.5^\circ$  in water if a refractive index of 1.33 is assumed<sup>18</sup> (Equation 1.10). The fiber was attached to an AvaSpec-ULS2048L StarLine single-channel diffraction grating spectrometer (Avantes BV, Apeldoorn, Netherlands), incorporating a linear 2048-pixel CCD array. The wavelength resolution of the spectrometer was approximately 0.6 nm. The spectrometer output was fed through a USB connection to a computer outside of the linac room. The application software provided with this spectrometer was AvaSoft 7.5 (Avantes BV, Apeldoorn, Netherlands). The spectrometer was shielded with blocks of lead and Solid Water<sup>®</sup> in order to minimize the effect of scatter radiation striking the electronics.

#### ***Dose versus Cherenkov studies***

The optical measurement setup in the dose versus Cherenkov studies is shown in Figure 3.3a. The two fiber tips at the photon collection side of the fiber were positioned at the edge of the field and directed roughly along the direction of maximum Cherenkov emission, ensuring no part of the beam entered the water tank through the side (see Section 3.3.3 for details). Since a bifurcated fiber was used in order to increase the SNR, agreement of the signal for 1 versus 2-fiber

detection was verified via simulation (see Section 3.1). 1 fiber tip was positioned along the central plane of the beam (i.e. the rotation plane of the gantry) and the other was placed at a position horizontally offset from the central plane by 1 cm.

### *Spectral shift studies*

The spectral shift studies were carried out in two different ways. One setup, which is described above, is shown in Figure 3.3b. The two fiber tips at the photon collection side of the bifurcated fiber were positioned against the side of the phantom and directed roughly along the direction of maximum Cherenkov emission. The second setup involved acquisition of the optical signal with a 2-fiber (for higher signal) optical fiber bundle of length = 30 m. The bundle was attached to a single-channel diffraction grating spectrometer, composed of an

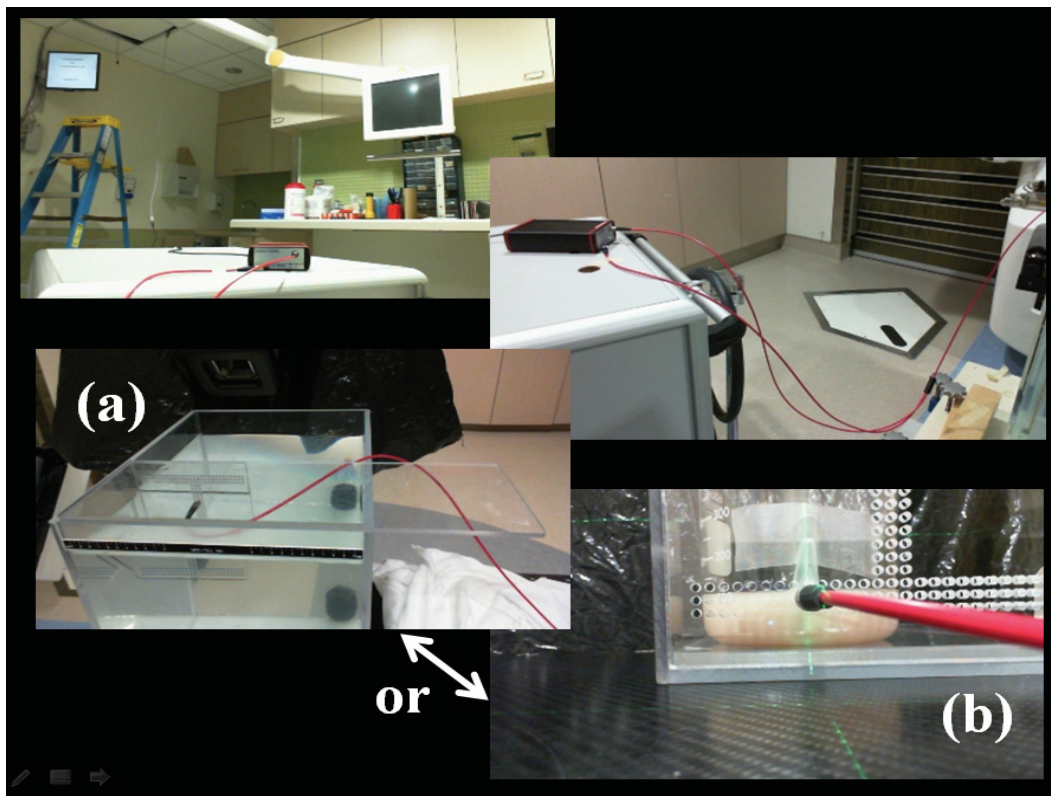


**Figure 3.3:** Optical acquisition setup for (a) dose versus Cherenkov and (b) tissue-simulating phantom experiments. The spectrometer, which is inside (dose-Cherenkov and first part of NIR shift studies) or outside (second part of NIR shift studies) of the treatment room, is connected to a computer on the outside of the room via a USB connection (top left). A fiber optic cable is attached to the spectrometer (top right) and positioned (a) in the water or (b) on the outside of the tissue-simulating phantom.

Acton Series SP 2356 spectrograph, incorporating a 300 ln/mm grating blazed at 1  $\mu\text{m}$ , and a PIXIS: 400B\_eXcelon 1340 $\times$ 400-pixel thermoelectrically cooled CCD camera (Princeton Instruments, Acton, MA/Trenton, NJ). The wavelength resolution of the spectrometer was approximately 0.4 nm. The bundle was long enough to allow positioning of the spectrometer outside the treatment room in order to avoid irradiation of the spectrometer electronics. The spectrometer output was fed through a USB connection to a computer. The application software provided with this spectrometer was LighField® 4.5 (Princeton Instruments, Acton, MA/Trenton, NJ). The fiber was positioned against the side of the phantom and directed roughly along the direction of maximum Cherenkov emission.

### ***Background signal reduction***

In order to reduce background signal during optical acquisition experiments, all ambient lights (with the exception of essential emergency lights) were shut off during signal acquisition and an opaque material was placed outside the water tank/phantom on the side of the beam opposite the fiber/fiber bundle to completely block all remaining light sources in the line of sight of the fiber/fiber bundle.

### **3.3.3 Fiber positioning**

A fiber holder (pictured in Figure 3.3a) was machined with holes for insertion of the fiber tip, hole center-to-center distance of 0.5 cm and both horizontal and vertical rows of holes. The positioning of the fiber for dose versus Cherenkov emission studies and for spectral shift studies is described below.

### ***Dose versus Cherenkov studies***

For the dose versus Cherenkov studies, the fiber holder was placed in the water such that the holes were parallel to the gantry plane of rotation. The two fiber tips were inserted in the holder, one centered and one offset by 1 cm from the central beam plane (as explained in Section 3.3.2), and aligned at the edge of the field.

Measurements were taken at discrete fiber positions at varying depths along the edge of the field.

In order to precisely control the fiber position, the *zero* position was first set as follows: The water level was varied until it was precisely aligned with the center of a row of holes of the fiber holder, so that half of each hole was above and half was below the water. The fibers were then inserted in that row and one fiber was aligned along the central plane of the beam, using the patient positioning lasers available in the treatment room and the treatment couch longitudinal position control. After rotating the gantry to  $47^\circ$  with respect to the vertical, the tips of the fibers were then aligned at the edge of the field, using the linac's field light and the lateral couch position controls. The couch lateral position displayed on the console was noted as the zero position.

Spectra were then recorded at 0.5, 1 or 2 cm depth intervals along the edge of the beam by moving the fibers

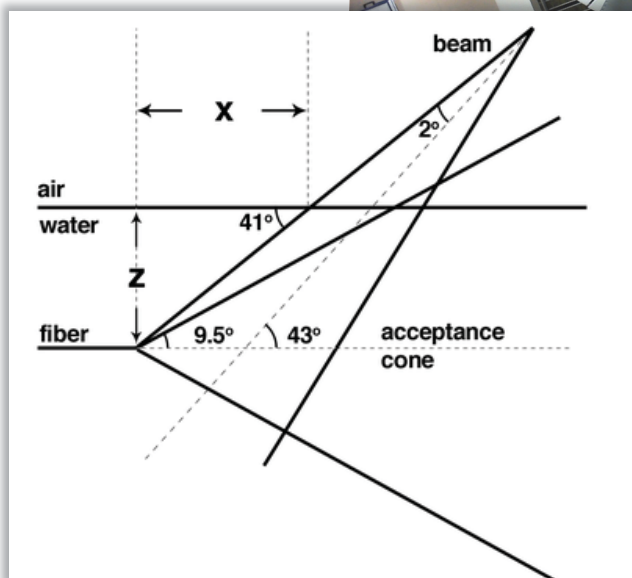
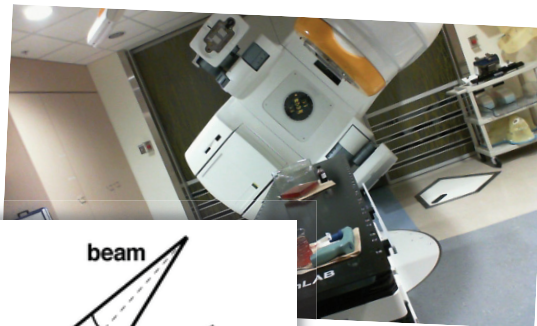


**Figure 3.4:** Diagram of fiber acquisition geometry for dose versus Cherenkov studies. As depth  $z$  was varied, the distance  $x$  from the field edge was adjusted accordingly (based on  $z$  and the beam angle) to ensure the fiber was positioned at the field edge. An image of the angled accelerator is shown to facilitate understanding of the acquisition geometry. Diagram is not drawn to scale.

along the vertical rows of holes of the fiber holder and laterally with the couch lateral position control. Desired positions were calculated relative to the zero position and based on the gantry angle of  $47^\circ$  and beam divergence. In Figure 3.4 is shown a diagram of the fiber and beam alignment and the corresponding depth and lateral displacements.

Since the size of the holes was known, the fibers could be placed at depths other than integer multiples of 0.5 cm by setting the zero position with the water level aligned to the edge of the holes or to the midpoint between holes instead of at the center.

### *Spectral shift studies*

For the quantum dot measurements, the fiber holder was placed against the phantom and the two fiber tips of the fiber bundle were placed horizontally in the holder at 1 cm from each other and at 0.5 cm below the surface of the phantom.

### **3.4 Quantum dots**

CdSe/ZnS core-shell colloidal nanocrystals in water, purchased from NN-Labs, LLC (Fayetteville, AR, USA), were used to demonstrate a shift of the Cherenkov emission spectrum from blue towards red wavelengths. Representative absorption and emission spectra of these quantum dots, provided by NN-Labs, are shown in Figure 3.5. Their absorption spectrum follows a similar trend as the Cherenkov emission spectrum, decreasing at increasing wavelengths, and they possess an

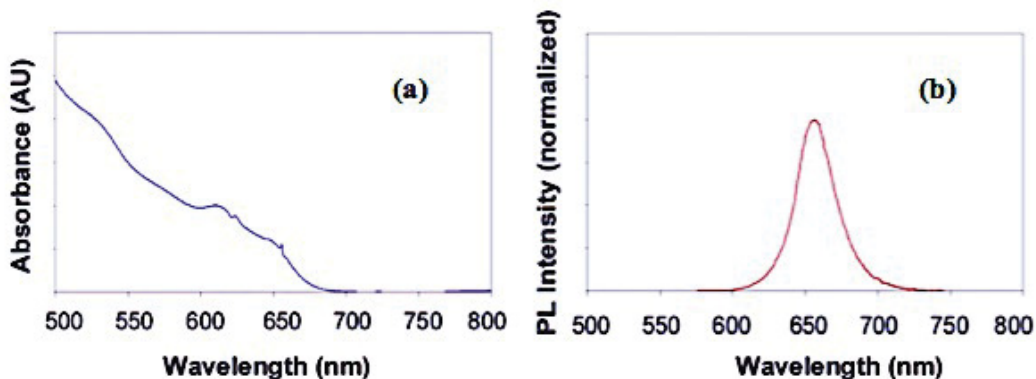


**Figure 3.5:** Representative (a) absorption and (b) emission spectra of CdSe/ZnS core-shell quantum dots in water (courtesy of NN-Labs, LLC).

emission peak at  $(650 \pm 10)$  nm. The fiber bundle was positioned against the phantom container and at a depth of approximately 0.5 cm below the surface of the phantom. Spectra were obtained without and with quantum dots in vials. For the water tank measurements, vials were placed in the water on the inside of the tank wall in front of the fiber. For the tissue phantom measurements, vials were placed inside the phantom at a distance of 0 to 1 cm from the wall in front of the fiber and just covered by the radiation field.

### **3.5 Digital signal processing**

A background signal was obtained with the beam characteristics and setup unchanged and the open end(s) of the fiber covered with an opaque cap. Spectra were processed by background subtraction, smoothing by pixel averaging and denoising with a Wiener filter in MATLAB® with the assumptions that the signal and noise are independent of each other and their individual and combined probability distributions do not vary in time and space.

### **3.6 Noise studies**

Q-Q plot studies (see Section 2.5) of the signal acquired with the Avantes system were carried out with the purpose of analyzing the experimental noise. Q-Q plots were generated for 3 types of data sets:

- Dark spectra acquired with the beam off – to evaluate the noise in the beam-on spectra solely due to the noise characteristics inherent to the spectrometer;
- Dark spectra acquired with the beam off after the beam had been on – to evaluate the noise in the beam-on spectra resulting from the inherent noise of the spectrometer and from residual signal in the spectrometer; and
- Signal distribution for a single pixel (i.e. wavelength) for many (usually 100) acquisitions with the beam on.

This type of analysis allows to infer important information about the tendencies (centered/skewed, narrow/broad) and type (random/systematic) of noise.

In this work, the signal and noise were assumed to be independent of each other and of time and position. In the future, power spectral density analysis, which is more systematic and less stringent than Q-Q plot analysis, will be used for this purpose. Readers unfamiliar with digital signal processing techniques are referred to Digital Signal Processing by John G. Proakis and Dimitris G. Manolakis.

## Chapter 4

# RESULTS AND DISCUSSION

### 4.1 Radiation dose versus Cherenkov emission correlation analysis

#### 4.1.1 Preliminary evaluation

A preliminary investigation of the correlation between radiation dose and Cherenkov emission was first carried out in order to determine if a comprehensive investigation is warranted. Plots of MC simulated depth dose and Cherenkov profiles, normalized to 1 at the position of maximum dose deposition/Cherenkov emission are provided in Figure 4.1. The Pearson correlation coefficient for these

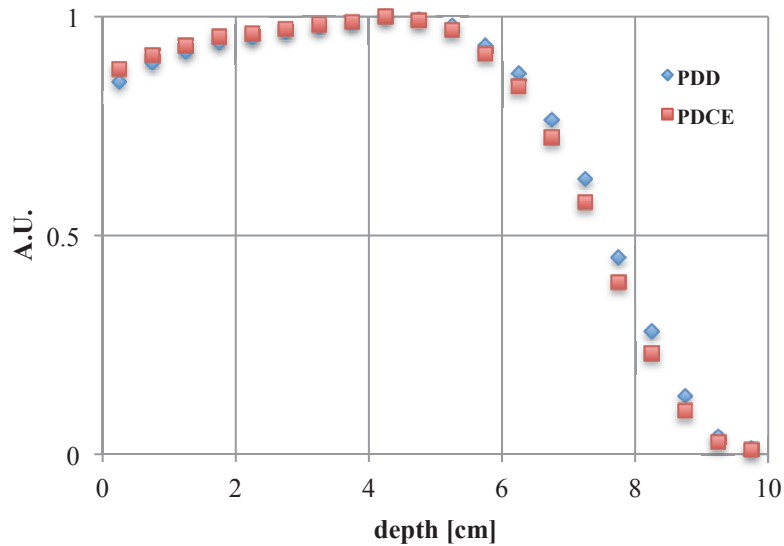


**Figure 4.1:** Percent depth dose (PDD) and percent depth Cherenkov emission (PDCE) photons acquired by simulating 4,000,000 events via Monte Carlo simulation in Geant4 of an 18 MeV electron beam incident on a block of water.

data sets is larger than 0.99. Uncertainty in the data is due to the slow convergence rate of this simulation, necessitating a limited number (4,000,000) of events, i.e. simulated primary particles and their effects, and large voxel size ( $0.5 \times 0.5 \times 0.5 \text{ cm}^3$ ). An image of a wedged 18 MV photon beam incident on a water tank is also shown in Figure 4.2 for a visual demonstration of the relationship. Electrons impacting the camera appear as noise in the image.

**Figure 4.2:** Photo of a wedged 18 MV photon beam incident on a water tank.

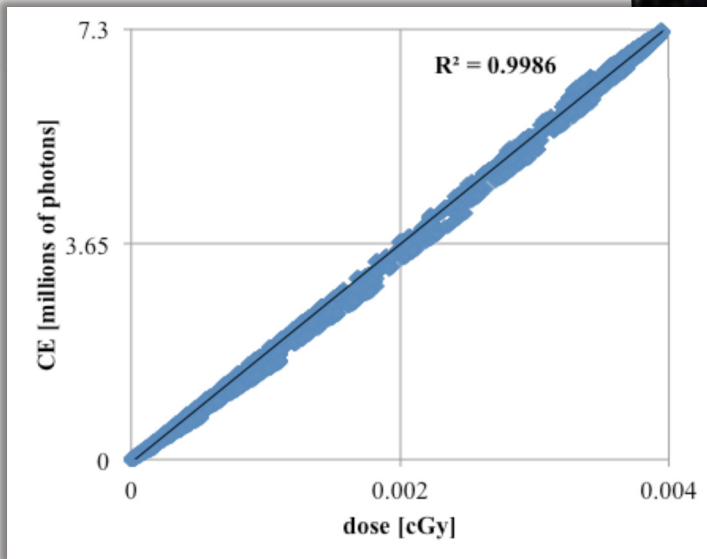
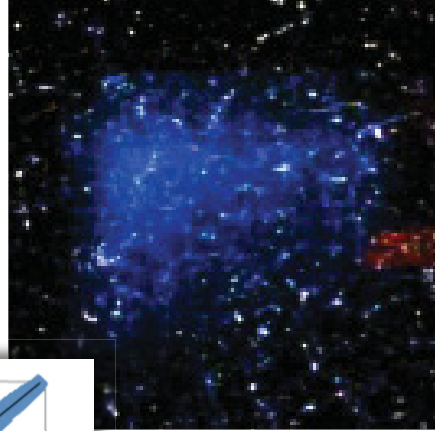


**Figure 4.3:** Simulated Cherenkov emission (CE) versus radiation dose deposited by an 18 MeV electron beam, incident on a  $10 \times 10 \times 10 \text{ cm}^3$  block of water, scored in  $0.5 \times 0.5 \times 0.5 \text{ cm}^3$  voxels. This data represents the simulation of 4,000,000 events in Geant4.

These Figures indicate a strong correlation between radiation dose deposition and number of emitted Cherenkov photons. For a quantitative affirmation, a plot of the simulated Cherenkov emission versus radiation dose is provided in Figure 4.3. Spearman and Pearson correlation coefficients were both larger than 0.99. Therefore, it can be concluded that dose and Cherenkov emission are approximately linearly correlated in space and further investigation of this correlation is justified.

#### 4.1.2 Angular sensitivity analysis

In Figure 4.4 are shown simulation and experimental results for the angular dependence of Cherenkov emission in a water phantom. The two acquisition setups are different, which explains the difference in the distribution of the data. In Figure 4.4a is given a plot of the 3D angular distribution of the number of Cherenkov photons emitted by a beam of 18 MeV electrons incident on a block of

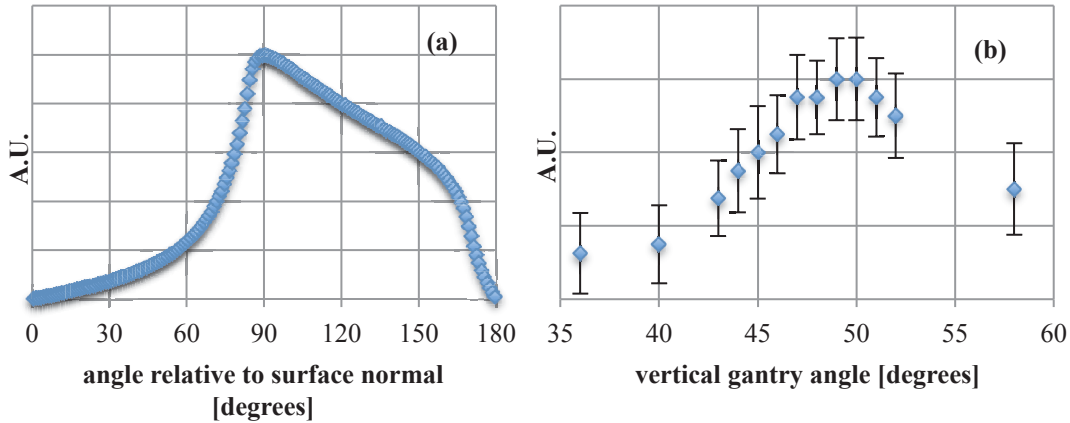


**Figure 4.4:** Angular distribution of (a) simulated (10,000 events) Cherenkov signal by an 18 MeV electron beam incident on a block of water at  $53^\circ$  to the surface normal and (b) Cherenkov signal by an 18 MeV linac electron beam, acquired with a horizontal fiber with varying gantry angle. All angles are defined relative to the surface normal. Error bars designate the 90% confidence interval.

water at  $53^\circ$  to its surface normal – an angle which resulted in a horizontal Cherenkov maximum (i.e. at  $90^\circ$ ). A horizontal Cherenkov maximum is desired in order to maximize the signal collected by a horizontal optical fiber, which would simplify the acquisition geometry. The data for Figure 4.4b, on the other hand, was generated by positioning the fiber horizontally and in the gantry’s plane of rotation and making measurements at discrete gantry angles. The maximum signal is at a gantry angle of  $50^\circ$  with respect to the vertical (i.e.  $40^\circ$  with respect to the fiber axis). For large gantry angles, a large portion of the beam entered the water through the side of the water tank perturbing the beam. For this reason, data points at large gantry angles are not as representative of the true angular distribution of Cherenkov emission in water and are therefore intentionally scarce.

These results indicate that in order to maximize the Cherenkov signal collected by a horizontal optical fiber, the linac gantry must be at an angle of approximately  $50^\circ$  relative to the vertical. An important difference between the two setups is the fact that the fiber detects photons within its collection cone; therefore, a given gantry angle corresponds to a range of detected photon angles. The simulation, on the other hand, only considers photons emitted at a specific angle relative to the normal to the surface on which the beam is incident. It must

be noted that these angular emission distributions result from the collective emission of a large amount of charged particles. Due to its charge and its small size, a single electron is scattered many times as it passes through the water, resulting in many changes in its direction of propagation.<sup>6</sup> This results in a broader angular distribution of emitted Cherenkov photons compared to that of an electron moving in a straight line. However, the average direction of a high-energy electron is along its initial direction. Therefore, the maximum Cherenkov emission angle of a high-energy electron beam is the same as for a single high-energy electron moving in a straight line in the same direction. The effect of the scattering is nevertheless manifested as a broadening of the angular distribution.

For subsequent scans, a gantry angle of  $47^\circ$  with respect to the vertical ( $43^\circ$  with respect to the fiber axis) was adopted in order to ensure that no part of the beam entered through the side of the water tank. This value was settled upon based on a necessary compromise between SNR and scan depth, both of which depend on the gantry angle. Since the beam is angled and the fiber is kept at the edge of the field, there exists a critical depth past which a portion of the fiber protrudes into the field. This depth increases as the beam angle decreases with respect to the vertical. An angle of  $47^\circ$ , for which the signal is stronger than 80% of the maximum (Figure 4.4b), provides a sufficiently high SNR while increasing the scan depth.

#### 4.1.3 Correlation between radiation dose and Cherenkov emission

The correlation between radiation dose and Cherenkov emission detected by a fiber optic cable was investigated via simulation and experimental measurements. Due to the lengthy process involved in experimental measurements with the optical equipment available for this project, optical measurements were only carried out for the 18 MeV electron beam. For all other beams used (6 and 12 MeV), a comparison was made only between the simulated Cherenkov data and the measured dose data. The overall Cherenkov simulation results and experimental dose and Cherenkov measurements for an 18 MeV beam, all normalized to 1 at the point of maximum signal, are provided in Figure 4.5. In

these plots, no correlation is evident between the simulated and measured Cherenkov data and dose scan. In the following sections, the discrepancy between measured and simulated Cherenkov emission will first be discussed, after which the relationship between dose and Cherenkov emission will be examined. Finally, the effect of the fiber cone volume will be considered.

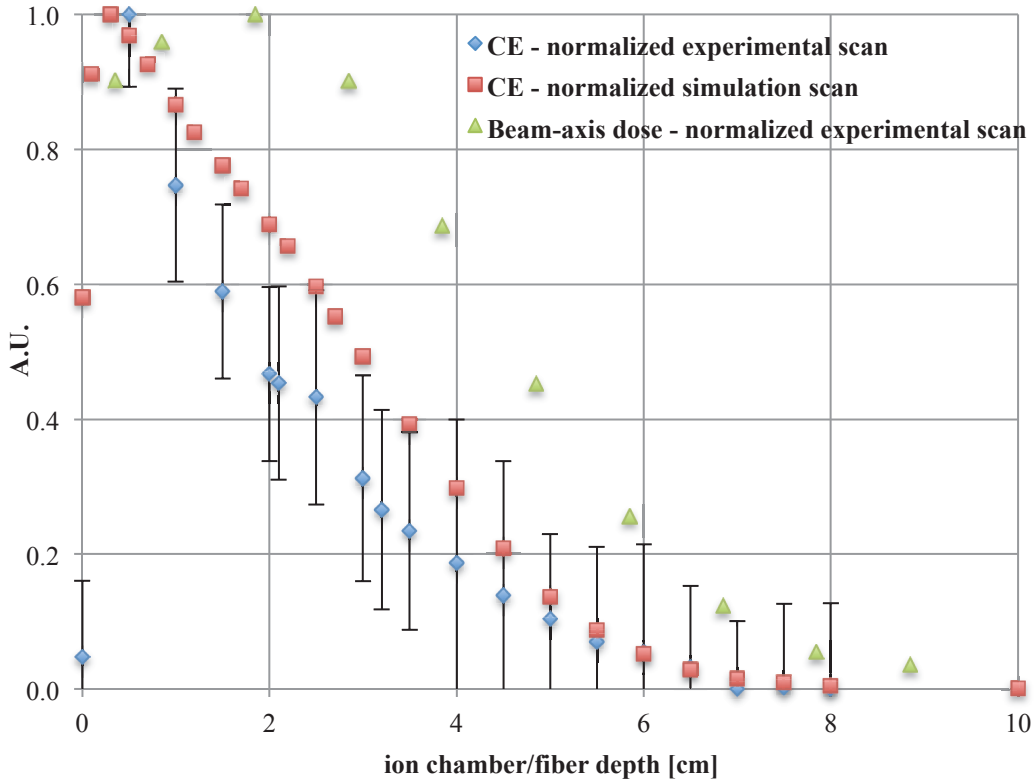


**Figure 4.5:** Cherenkov emission (CE) simulation results (5,000,000 events) and experimental beam-axis dose and CE measurements, all normalized to 1 at the point of maximum signal, acquired with a 18 MeV electron beam and  $47^\circ$  incidence angle. Error bars designate the 90% confidence interval.

### ***Correlation between simulated and experimental Cherenkov emission***

Experimental conditions can never be fully reproduced in computer simulations. Some obvious examples are the non-discrete variation of material properties with temperature and pressure and the presence of impurities. For this reason, computer simulations are idealized cases of experimental conditions and discrepancies may exist between simulated and measured data. In this work, the simulated Cherenkov scan involved scoring of photons based only on their

emission position and initial direction. This ignores physical processes, such as absorption and more importantly, in the case of highly transparent materials such as water, reflection, which may result in a larger or lower number of photons collected by the fiber due to photons being reflected towards or away from the fiber, respectively. Reflection occurs at surface boundaries of materials of different indices of refraction.<sup>17</sup> Since in this setup the angular distribution of Cherenkov emission has a maximum approximately along the fiber axis, which is horizontal, and decreases gradually away from this maximum (see Section 4.1.2), many photons are emitted towards the water surface, especially at small angles relative to the surface. A portion of these photons may be reflected at the surface towards the fiber and collected by the fiber if their incidence angle at the fiber tip (or incidence angle relative to the water surface) is equal to or smaller than the fiber's acceptance angle ( $\sim 9.5^\circ$ ). This effect would result in an increase in the Cherenkov signal at decreasing depths since photons emitted at small angles relative to the water surface are much more likely to reach the surface (as opposed to exiting through the side of the water tank) at shallower depths. In order to test the hypothesis that reflection from the water surface may be the cause of the discrepancy between simulated and measured Cherenkov emission, all data points for which the intersection between the fiber cone of acceptance and the water surface is in the radiation field (see Figure 3.4) were removed from the data set and the results were renormalized with respect to the new maximum position. Therefore, points corresponding to depths less than 2 cm, which is the first data point for which the cone-water surface intersection is just outside of the field, were removed, and the scans were renormalized to the new maximum signal at 2 cm (Figure 4.6). The resultant correlation between corresponding data points of the renormalized plots is strong with a Pearson correlation coefficient larger than 0.99. The correlation was apparent even when readings at depths as low as 1.5 cm were included in the renormalized plots, possibly due to the fact that photons reflected from the water surface towards the fiber at  $9.5^\circ$  or less constitute only a small fraction of the total photons collected by the fiber at that depth. Though this outcome does not conclusively confirm that the discrepancy is mainly due to

exclusion of surface reflected photons from the simulation, it strongly supports this premise.

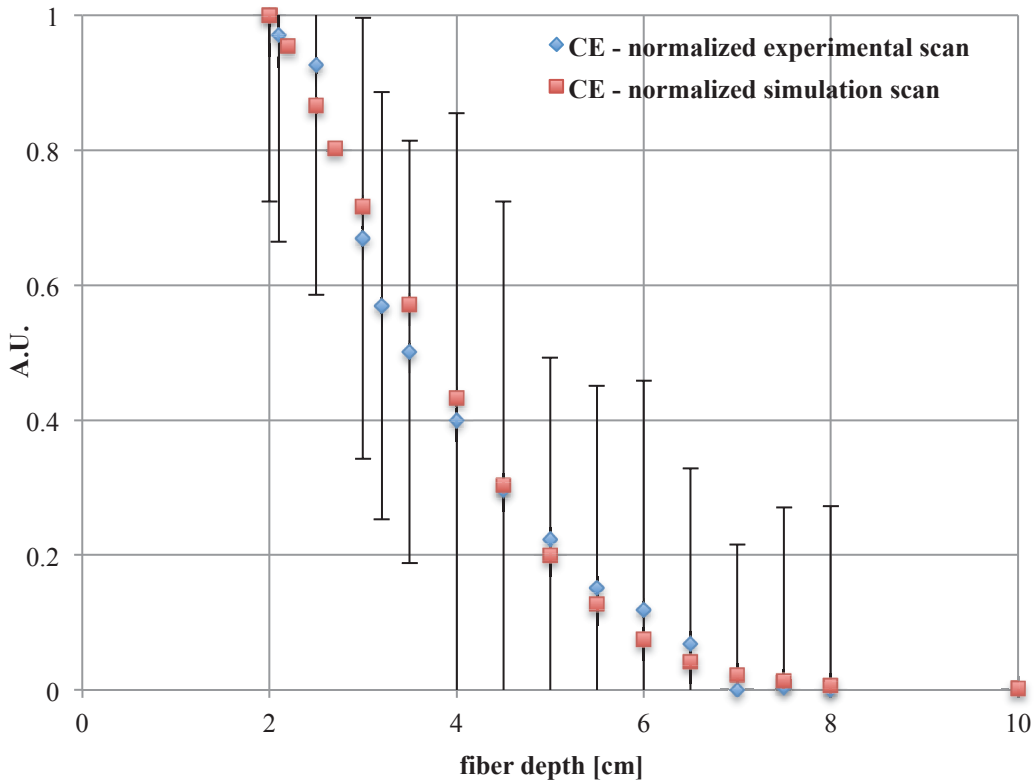


**Figure 4.6:** Cherenkov emission (CE) simulation results (5,000,000 events) and experimental CE measurements, normalized to 1 at a 2 cm depth, acquired with a 18 MeV electron beam and  $47^\circ$  incidence angle. Error bars designate the 90% confidence interval.

### ***Correlation between radiation dose and Cherenkov emission***

A shift of the 18 MeV Cherenkov scan by 1.7 cm away from the surface aligns it almost ideally with the beam-axis dose scan (Figure 4.7), producing a Pearson correlation coefficient larger than 0.99 for the simulated Cherenkov and dose data. Since the correlation between Cherenkov and dose was found to be very strong in the preliminary simulation analysis (see Section 4.1.1), where Cherenkov photons emitted in all directions were scored per voxel, the discrepancy must be related to either the averaging effect of the fiber collection cone (the ion chamber sensitive volume is much smaller than the fiber collection cone) and/or directional selection of photons by the fiber (only photons directed towards the fiber and at an angle lower than the acceptance angle are collected by the fiber). In order to test the

former assertion, a simulation was carried out with no directional selection of the collected photons – photons emitted in any direction, but only in the fiber cone, were collected. The resulting distribution invalidates the first assertion as the only cause of the discrepancy, since in fact a shift in the opposite direction was observed, and points to directional selection as one of the causes.

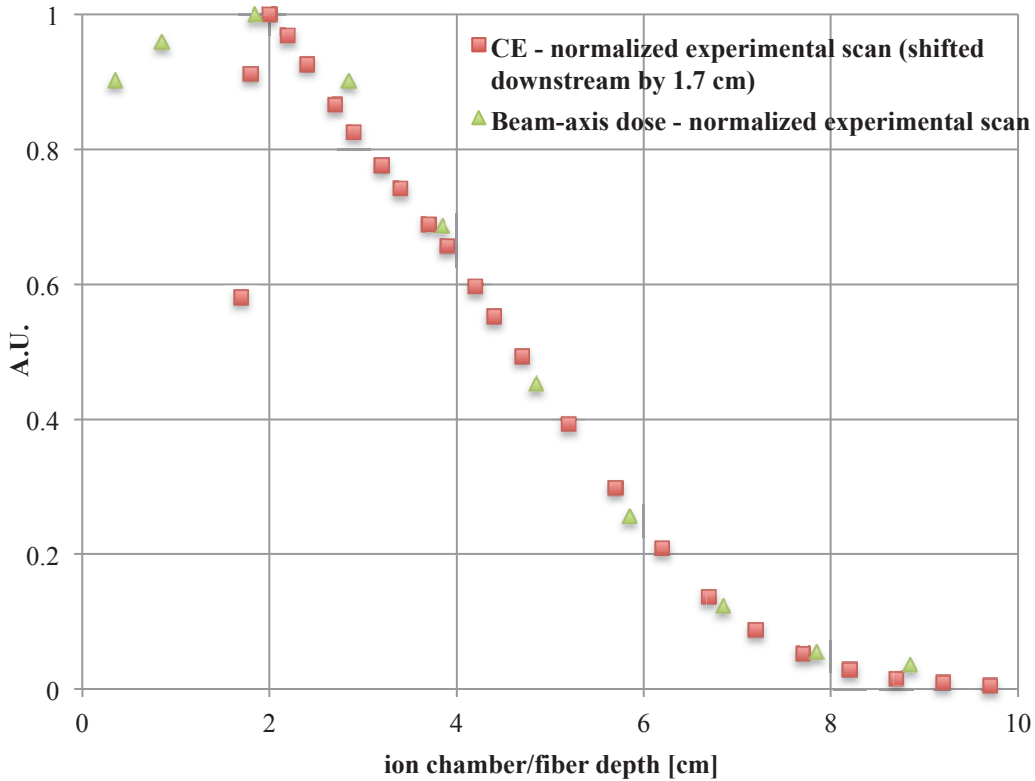


**Figure 4.7:** Cherenkov emission (CE) simulation results (5,000,000 events), shifted downstream by 1.7 cm, and experimental beam-axis dose measurements, all normalized to 1 at the point of maximum signal, acquired with a 18 MeV electron beam and 47° incidence angle.

With electron beam energies of 6 and 12 MeV, different shifts were observed, namely 0.1 cm (Figure 4.8) and 0.8 cm, respectively, indicating that measurement geometry alone is not the sole reason for the shift. Beam energy is a major contributor and, as one might speculate, the shift decreases with decreasing beam energy.

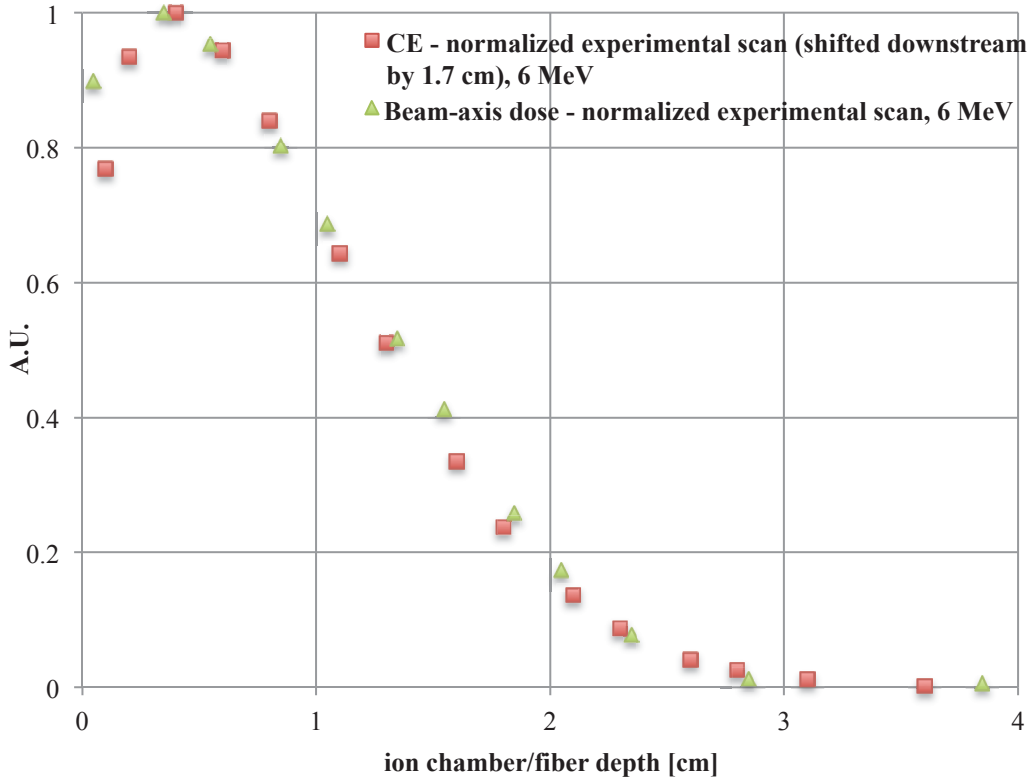


**Figure 4.8:** Cherenkov emission (CE) simulation results (5,000,000 events), shifted downstream by 0.1 cm, and experimental beam-axis dose measurements, all normalized to 1 at the point of maximum signal, acquired with a 6 MeV electron beam and 47° incidence angle.

A possible explanation for these shifts is the fact that, in this setup, Cherenkov photons detected by the fiber are emitted by high-energy electrons, which dominate the deposition of dose and deposit their energy after Cherenkov emission. The angle between the beam axis and fiber axis is 43°, the fiber acceptance angle is approximately 9.5° in water (see Section 3.3.2), and the beam divergence half-angle is approximately 2° (see Figure 3.4), which is calculated from the known field size of 6×6 cm<sup>2</sup> at 100 cm from the source. This means that photons accepted by the fiber are emitted at angles in the range of 31° to 55° (i.e. 43° ± [9.5° + 2°]) with respect to the average electron direction of propagation, corresponding to electron normalized velocities of 0.9c and higher in water, assuming a refractive index of 1.3 (Equation 2.1). Electrons of such high velocities have yet to deposit the bulk of their energy and contribute a great deal more to dose deposition in comparison to low energy electrons. Since the

detection geometry does not change with depth, the angles of detected Cherenkov photons are the same for all fiber depths. Therefore at all fiber depths, it is electrons of the same high energies that contribute to the fiber reading, and thus the distance traveled before these electrons deposit their energy is constant along the scan, explaining the constant downstream shift between Cherenkov emission and dose deposition. A mathematical derivation for this shift is necessary and will be carried out in the future in order to fully understand its origin.

### ***Fiber cone volume effects***

In the optical measurement setup of this work, the volume of the fiber cone that is in the radiation field (called the acceptance or sensitive volume) varies with depth for two reasons: (1) At shallow depths of 2 cm or less, the water surface truncates the fiber acceptance cone in such a way that the cone-water surface intersection is in the field (see Figure 3.4); (2) The beam diverges, and therefore the field size increases, with increasing distance from the source. The former provides a plausible explanation for the shape of the Cherenkov simulation data with an 18 MeV electron beam for depths of 2 cm or less (Figures 4.5 and 4.7). The smooth curvature of the distribution for points up to 2 cm depth is interrupted by an almost linear section for shallower depths and a sharp drop in signal at the surface. The linear section may result from linearity with respect to depth in the volume expression for the section of the cone that is in the field. The sharp drop can be explained by the fact that at zero depth, the acceptance volume is approximately equal to half the volume at depths larger than 2 cm since the fiber cone is horizontal. If truncation of the acceptance cone is taken into account by, for example, calculating the acceptance volume for each fiber position and representing the data in terms of signal per unit volume, values at depths 2 cm or less will increase with respect to values at larger depths, since they correspond to a smaller acceptance volume and since values at larger depths will then be normalized by the now larger value at the depth of maximum signal, namely 0.3 cm. The second reason above causes a less drastic variation in the sensitive volume with depth since it can be shown that the field size along the fiber cone

axis varies by a maximum of 1 cm throughout the entire scan length with a minimum value of 10 cm. The volume effect is less pronounced for plots normalized to 2 cm (see Figure 4.6), since the issue of acceptance cone truncation is eliminated, and for lower energies (see Figure 4.8), since the steeper depth dose gradient overshadows the effects of cone truncation. Future work calls for a thorough quantitative volume effect analysis.

#### 4.1.4 Two-fiber dependence

Data collected with a fiber positioned in the plane of rotation of the gantry and a fiber laterally offset from the plane by 1 cm were compared via simulation in order to justify the use of 2 fibers for experimental detection of the Cherenkov

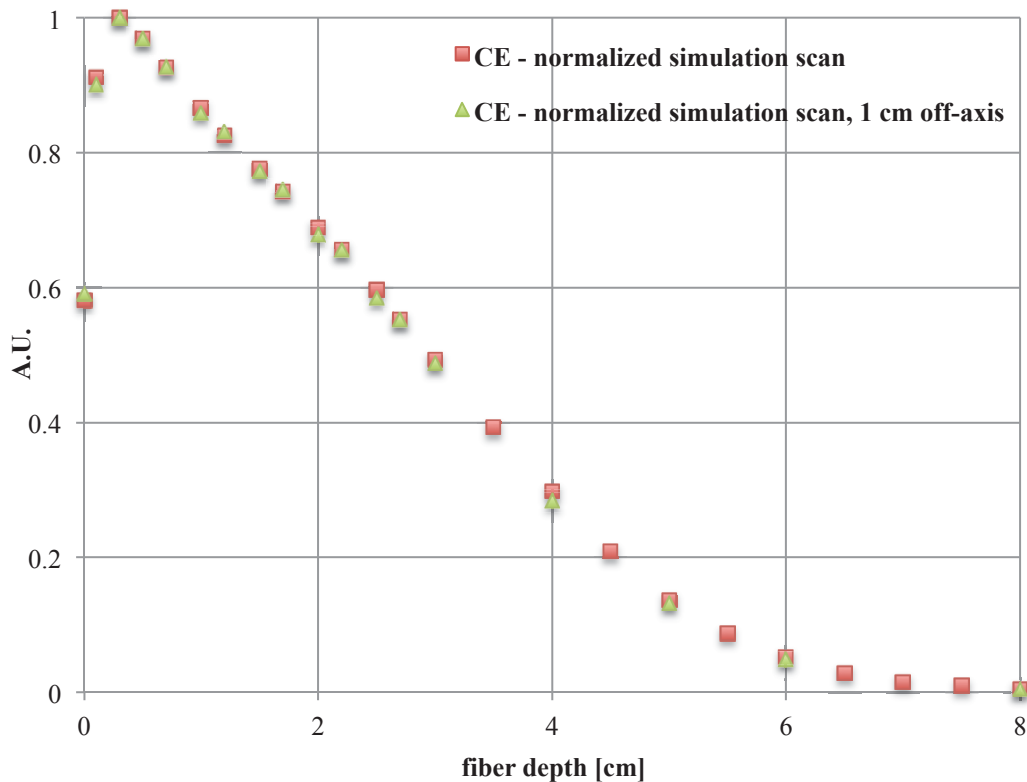


**Figure 4.9:** Cherenkov simulation results normalized to 1 at the point of maximum signal for an 18 MeV beam of incidence angle  $47^\circ$ , detected with a fiber centered or offset by 1 cm relative to the beam axis.

emission with the aim of increasing the signal-to-noise ratio. The main difference that might be expected is due to the slight change in beam angle with respect to

the fiber axis. Laterally offsetting the fiber by 1 cm from the gantry plane of rotation has no significant effect on the signal detected as seen in Figure 4.9. This is the case for different beam energies.

## 4.2 Spectral shift experiments

A shift of the UV-weighted Cherenkov emission by radiotherapy treatment beams towards the NIR window of tissue was successfully demonstrated with the purpose of validating its potential for optical imaging during radiotherapy. The shift was first performed for Cherenkov emission in a water tank in order to evaluate its capacity for stimulating photoluminescence of the CdSe/ZnS quantum dots (QDs), after which it was demonstrated in a tissue-simulating phantom. These experiments were carried out in two different ways using two different acquisition setups/instruments as described in Section 3.3.2.

The water tank spectra with and without QDs in the beam, acquired with the first setup (Avantes spectrometer placed inside the treatment room, see Section 3.3.2), are shown in Figure 4.10 for field sizes of  $5 \times 5 \text{ cm}^2$  and  $5 \times 3 \text{ cm}^2$ . The side of the field that was varied from 5 to 3 cm was the side parallel to the fiber axis (see Figure 3.4). This effectively decreases the volume of the fiber cone that is in the field. The other side (perpendicular to the fiber axis, out of the page in Figure 3.4 above) was kept constant at 5 cm since a variation in one dimension allowed a more straightforward analysis of the change in signal. Decreasing the field size along the fiber axis decreases the volume of the fiber acceptance cone, which should decrease the amount of Cherenkov emission. As expected, a decrease in the blank (no QDs) Cherenkov spectrum is evident with decreasing field size. In addition, there is strong absorption of the blue wavelengths by the QDs, decreasing towards the red, and a signal increase in the region of 650 nm is observed due to QD emission. Perhaps due to saturation of the QD excitation states, there is no observable relative decrease in absorption when the field is changed from  $5 \times 5 \text{ cm}^2$  to  $5 \times 3 \text{ cm}^2$ . An unexpected larger relative spectral shift at 650 nm is evident with the  $5 \times 3 \text{ cm}^2$  field. There are many possible reasons for this, including the fact that the intensity of the blank spectrum at 650 nm is higher

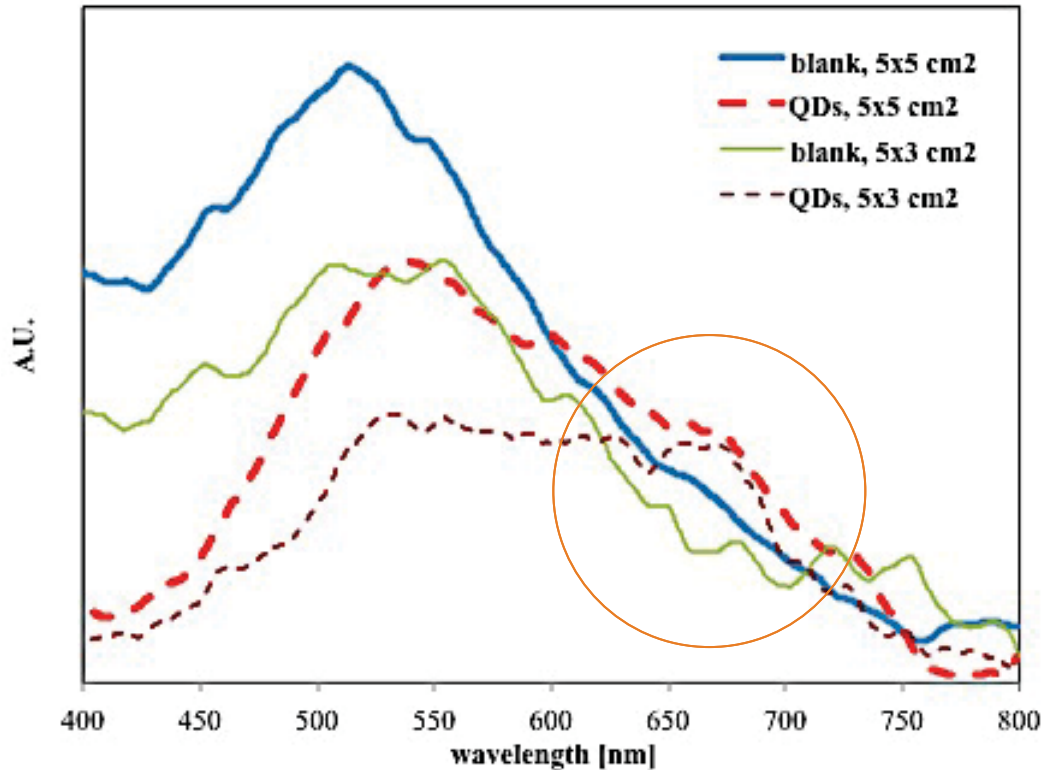


**Figure 4.10:** Water tank Cherenkov spectra acquired with the Avantes setup. Spectra were acquired with an 18 MeV electron beam, with and without CdSe/ZnS core-shell quantum dots (QDs) positioned in front of the fiber in water, with field sizes of  $5 \times 5$  and  $5 \times 3$   $\text{cm}^2$ . Circled area designates the spectral shift region.

for the  $5 \times 5$   $\text{cm}^2$  field, which results in a smaller relative increase. In addition, the larger shift may be a noise artifact resulting from the high amount of noise present with this instrument, which is often difficult to remove by conventional smoothing/filtering. Base on the results of this study, it can be concluded that Cherenkov emission can effectively excite CdSe/ZnS core-shell quantum dots.

Spectra with and without QDs placed at 0 and 10 mm depths in a tissue-simulating phantom, acquired with the Avantes system, are shown in Figure 4.11. A shift of the Cherenkov emission towards 650 nm is evident in this figure. These results substantiate the feasibility of the proposed wavelength-shifting method for imaging during radiotherapy. These spectra are recognizably less smooth than the spectra acquired with a water tank due to a lower SNR stemming from higher attenuation of optical wavelengths by tissue. As expected, the signal is much weaker for a depth of 10 mm, though a prominent shift to 650 nm is still manifest.

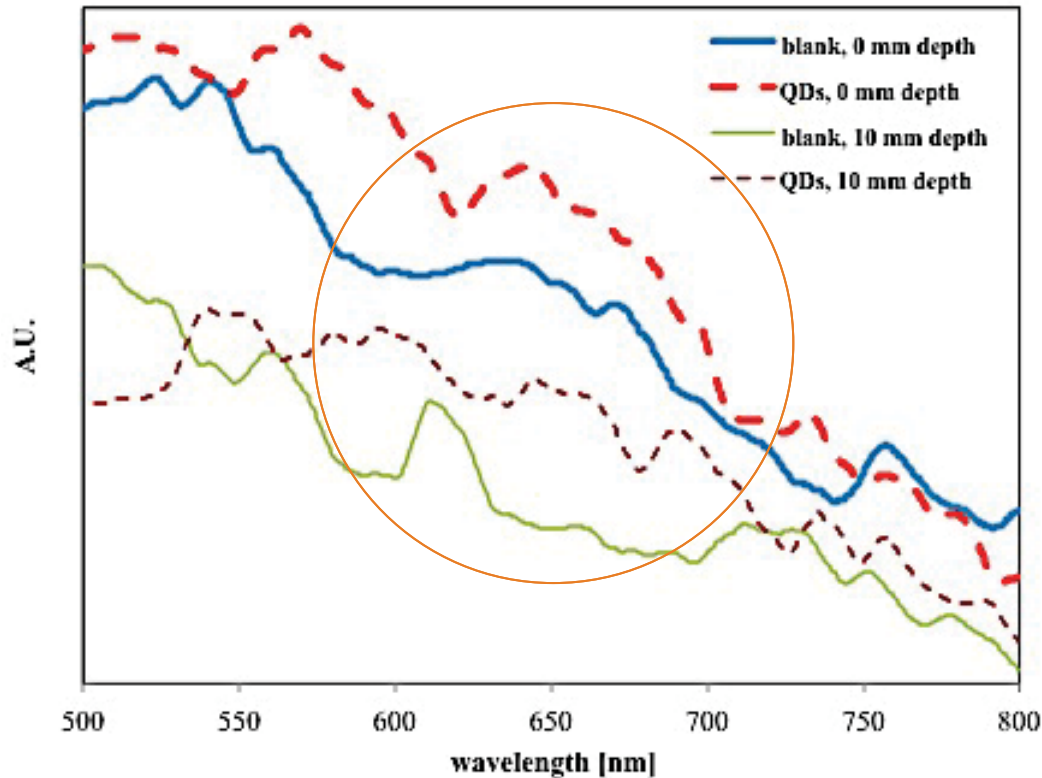


**Figure 4.11:** Tissue phantom Cherenkov spectra acquired with the Avantes setup. Spectra were acquired with an 18 MeV electron beam, with and without CdSe/ZnS core-shell quantum dots placed in front of the fiber in a tissue-simulating phantom at depths of 0 and 1 cm. Circled area designates the spectral shift region.

For signal strength comparison, water tank and tissue phantom blank spectra are plotted together in Figure 4.12. Due to higher SNR, the water tank spectrum is much more intense and noticeably smoother at shorter wavelengths. At longer wavelengths, however, the two spectra are of comparable intensity. In the NIR window ( $\sim 700\text{-}900$  nm), an increase in signal is expected for the tissue-simulating phantom relative to the water tank signal; however, a sharp decrease in signal is observed in the middle. There are a number of likely explanations for this effect. One of the most plausible explanations is that the drop in signal is a noise artifact due to the very low SNR in the NIR window. The water tank and tissue phantom signals are of comparable strengths in that region of the spectrum and are both oscillating in a similar fashion, which is expected since their SNR is comparable. Therefore, this oscillation, resulting in signal drops and peaks, is

present in both spectra and may be caused by noise. Another less likely explanation for the dip is high absorption of NIR wavelengths by the phantom container since the fiber was placed on its exterior. This is a less plausible explanation because the phantom container was a transparent glass beaker and there is no such dip observed in the water tank spectrum, even though the water

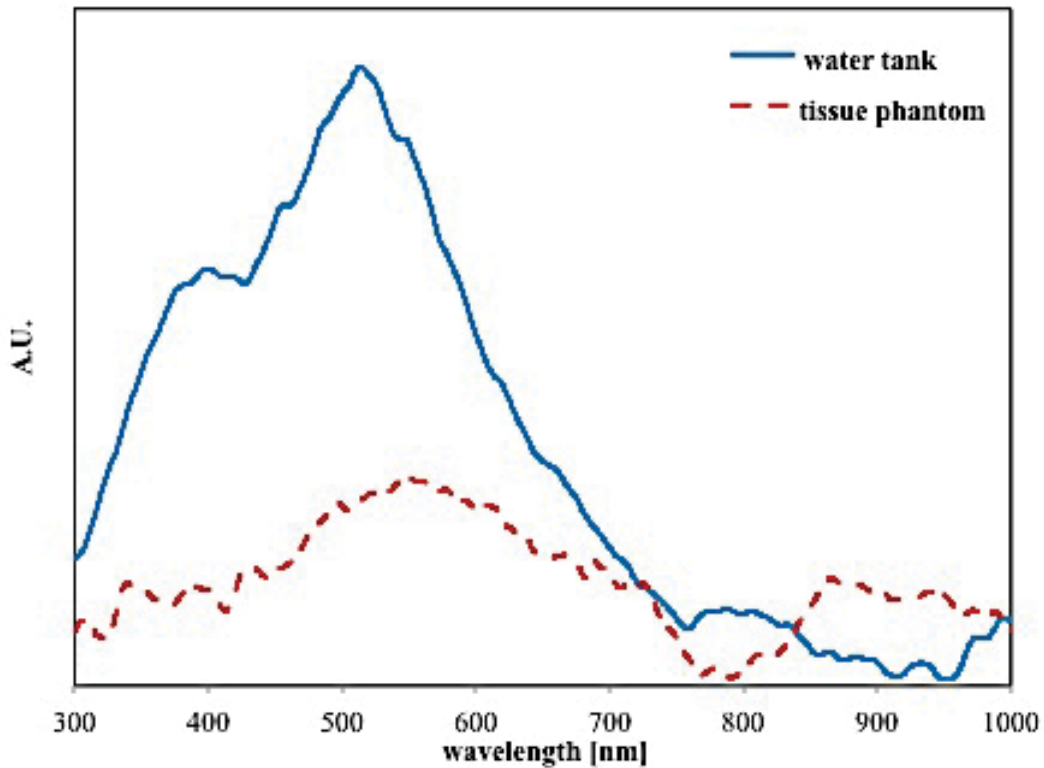


**Figure 4.12:** Cherenkov spectra acquired with an 18 MeV electron beam incident on water or on a tissue-simulating phantom.

tank was made of a similar material. Nevertheless, this issue was not of major concern for this study since primarily the signal intensity at 650 nm (the centre wavelength of the QD emission profile) was of interest.

NIR shift spectra were also acquired with an Acton Series SP 2356 spectrograph and a PIXIS: 400B\_eXcelon CCD camera as described in Section 3.3.2. The resulting water tank and tissue phantom spectra are shown in Figures 4.13 and 4.14. Again, the shift to 650 nm is evident in both figures. The strong absorption by the QDs of wavelengths towards the blue region of the spectrum is manifest in both figures. This effect is much less prominent in the tissue phantom

spectra since tissue is much more absorptive in the blue region than water. The superiority of the Acton-PIXIS setup over the Avantes setup is markedly apparent in these figures. The PIXIS spectra are much less affected by noise than the Avantes spectra. This stems in part from the fact that the PIXIS camera features a deep thermoelectric cooling mechanism and a back-illuminated design to minimize electronic noise and maximize the amount of light detected. In addition, all 400 channels of its 1340×400-pixel CCD array were binned to increase the SNR. Another factor in noise reduction is the fact that the PIXIS system was placed on the outside of the treatment room, and it was therefore not exposed to radiation.

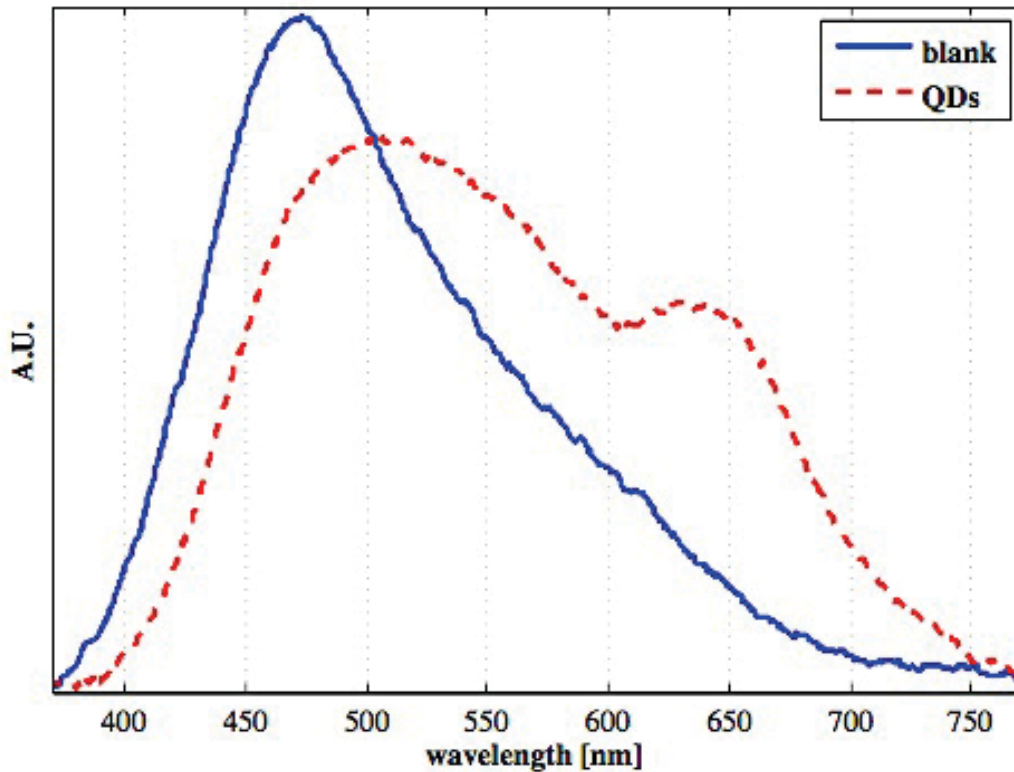


**Figure 4.13:** Water tank Cherenkov spectra acquired with the Acton-PIXIS setup. Spectra were acquired with an 18 MeV electron beam, with and without CdSe/ZnS core-shell quantum dots (QDs) positioned in front of the fiber in water.

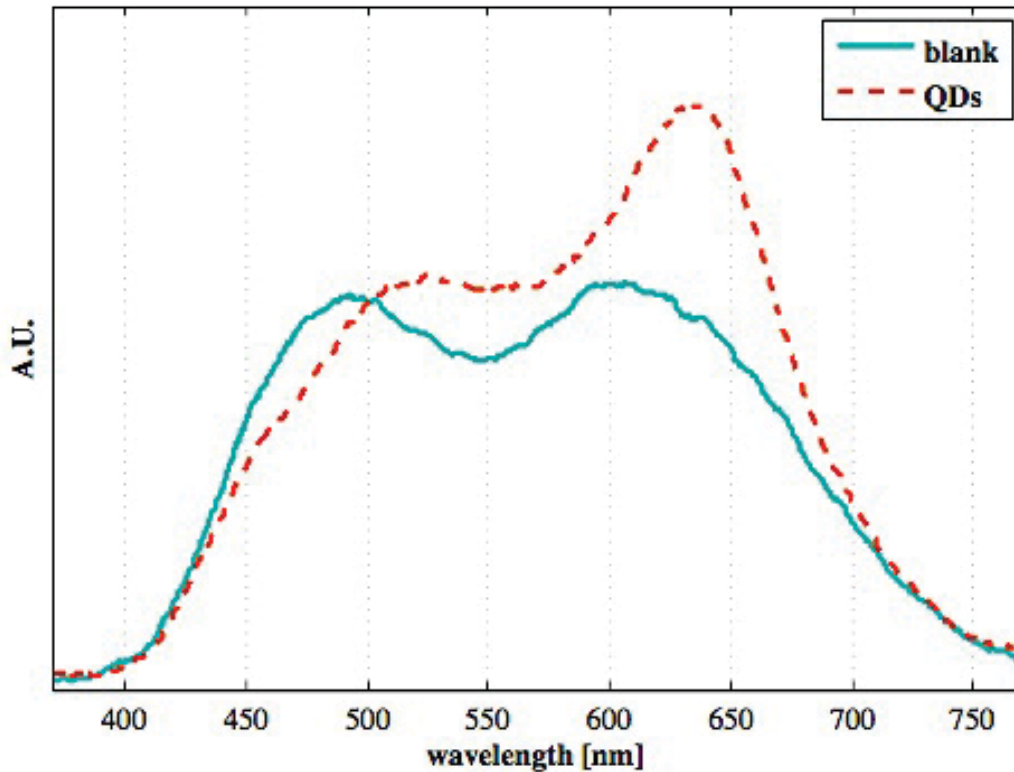


**Figure 4.14:** Tissue phantom Cherenkov spectra acquired with the Acton-PIXIS setup. Spectra were acquired with an 18 MeV electron beam, with and without CdSe/ZnS core-shell quantum dots placed in front of the fiber in a tissue-simulating phantom at a depth of 0.5 cm.

### 4.3 Noise studies

For the purpose of this work, statistical signal and noise pattern studies were performed on results acquired with the Avantes system in the form of Q-Q plot analyses. In addition, a Wiener filter was adopted for spectral noise removal with the following assumptions: the signal and noise are (1) independent of each other and are (2) ergodic processes (wide-sense and jointly wide-sense stationary, i.e. their individual and joint probability distributions do not carry any temporal or spatial dependencies). In subsequent work, more comprehensive less stringent power spectral density analyses will be carried out. For a detailed account of signal processing, including power spectral density analysis techniques, the reader is referred to Digital Signal Processing by John G. Proakis and Dimitris G. Manolakis.

Normal probability Q-Q plots of beam-off and beam-on spectra were generated with the spectral distribution data on the y-axis and the corresponding normal probability distribution quantiles on the x-axis. The following are key observations and analyses of the Q-Q plots:

- No Q-Q plots with the whole data set included are linear; therefore, neither the beam-on single-wavelength distribution nor the beam-off distribution over all wavelengths are normally distributed.
- All Q-Q plots had one area of highest density of points at the center with decreasing density towards the sides (see Figure 4.15). This means that all sampled distributions have one peak, within which a large number of samples are located, and decrease towards high and low values as does the standard normal distribution; they are unimodal.
- No Q-Q plots exhibit a J-shape or inverted J-shape and all are symmetric about their center, which indicates that none of the distributions are skewed. For the beam-off data, it can therefore be inferred that noise in the spectrometer (not due to photon collection) is white with respect to wavelength, meaning it does not vary with wavelength. For the beam-on single-wavelength data, this shows that the noise is not biased towards higher or lower values than the signal. Both pixel position (i.e. wavelength) dependent and count-dependent noise is symmetric about the mean. This is important because it indicates that the SNR is not wavelength-dependent and the signal is not positively/negatively biased by the tendencies of the noise.
- The center portions of all beam-off Q-Q plots (Figure 4.15) – with no beam on at all and after beam on – have an inverted S-shape, the curvature of which is inverted at the ends. This points to a distribution with heavier tails (more values further from the mean than for the normal distribution) that are relatively uniform.

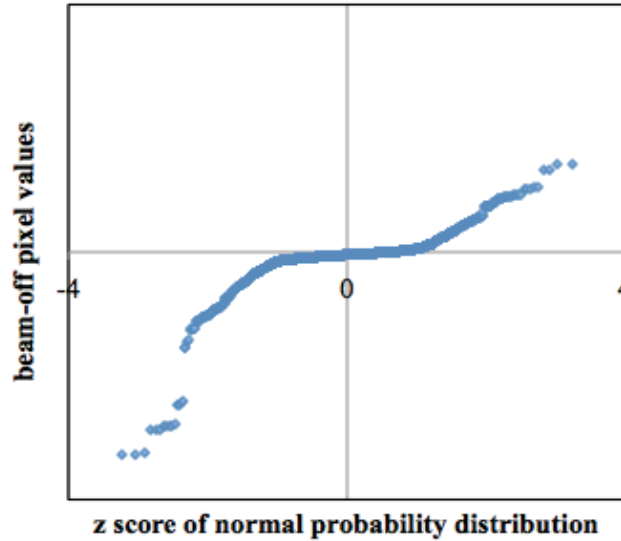


Figure 4.15: Sample Q-Q plot of beam-off distribution of pixel values over all pixels.

- Q-Q plots of only the center few 100 data points of the sorted beam-off distributions (Figure 4.16) have a marked S-shape, which implies that the distribution is much more uniform at the center than the normal distribution and with light tails. Zero noise is desirable in any measurement system. In this case, however, no single value for noise is especially favored; a range of values are fairly equally present.

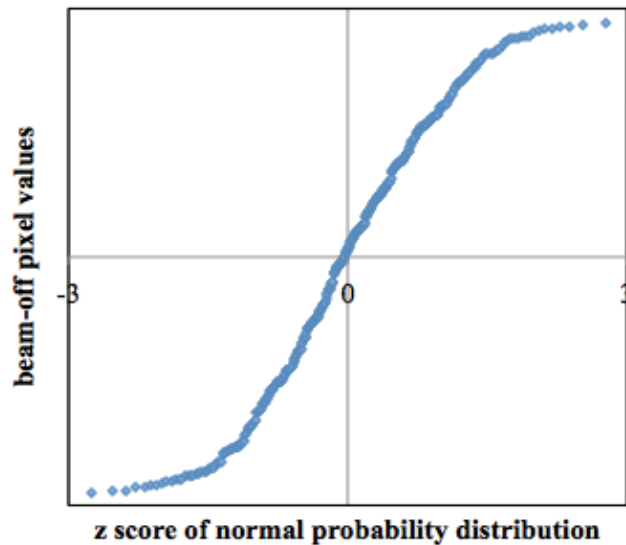


Figure 4.16: Sample Q-Q plot of center few 100 beam-off values from the sorted distribution for all pixels.

- Q-Q plots of the distribution of values of the beam-on signal at a single pixel (Figure 4.17) feature a markedly straight central section curving upwards at high values and downwards at low values. The curved sections consist of much fewer values than the central portion. Excluding a few (~5-10 out of 100) of the lowest and highest values generally results in a nearly straight Q-Q plot. This is the case for pixels with zero and with non-zero signal. These characteristics indicate that the beam-on distribution for each pixel is approximately normal with the exception of a few outliers. Due to the finite acquisition time and the discrete nature of light, a finite number of photons is collected at each acquisition and the distribution of the number of collected photons obeys the Poisson distribution (see Section 1.4.2). The number of photons is large enough so that the Poisson distribution approaches a normal distribution. Therefore, normality of the central range of the sorted pixel values is to be expected. This is also the case for electrons in the CCD, which explains why the signal distribution for pixels whose mean signal is zero is also normal. A possible cause of the outliers in the distribution is radiation impacting the spectrometer. Other than the fact that their number is low and that the

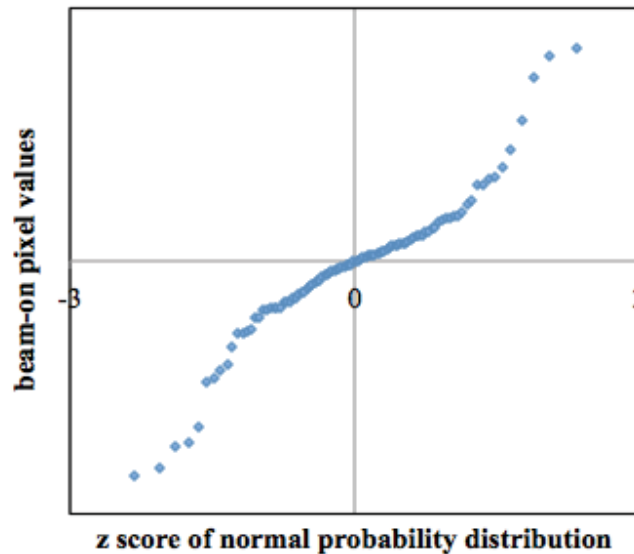


Figure 4.17: Sample Q-Q plot of beam-on signal distribution of one pixel.

distribution is approximately normal upon their exclusion from the Q-Q plot, the consistently higher or lower values than expected (relative to the normal distribution) for outliers on the right and left, respectively, of the Q-Q plot support the explanation that they are the result of impact of radiation on the spectrometer. The spectrometer is an electronic instrument and ionizing radiation incident upon it is expected to cause large variations in its signal. In addition, shielding the spectrometer substantially decreased the noise. Accordingly, the median of the data, and not the mean, was usually used for data processing and analysis in order to reduce the influence of outliers on the signal.

## *Chapter 5*

### **CONCLUSION**

---

The aim of this work was to evaluate the potential of Cherenkov emission by radiotherapy treatment beams for application in radiotherapy dosimetry and online imaging during radiotherapy. This was achieved through (1) computer simulation and experimental analysis of the correlation between dose deposition and Cherenkov emission in water – a standard phantom material used in radiotherapy – and (2) the use of photoluminescent quantum dots to demonstrate a shift in the Cherenkov spectrum towards the near-infrared window of tissue in a tissue-simulating phantom. In addition, a comprehensive noise analysis of the measured signal was carried out in order to investigate its source, determine the best way to process and represent the data, and in general assess the efficacy of the measurement setup. The following points summarize the results of this work and the associated discussion, and present the key conclusions:

- For high-energy radiotherapy treatment beams incident on water, radiation dose and Cherenkov emission exhibit strong spatial correlation (Pearson product-moment correlation coefficient  $\geq 0.99$ ).
- The angular intensity distribution of Cherenkov emission by high-energy radiotherapy treatment beams, incident on water at approximately  $50^\circ$  relative to the surface normal, is relatively broad due to electron scattering, has a horizontal maximum (at an angle of approximately  $40^\circ$  relative to the beam central axis), and gradually decreases away from that angle. The fact that the angular distribution is considerably broad provides flexibility in the optical measurement setup, such as optical fiber positioning relative to the radiation beam.
- With a multi-mode fiber optic cable positioned horizontally in water and with its tip at the field edge, and the gantry rotated such that the maximum of Cherenkov emission in the water is directed approximately along the fiber axis ( $\sim 50^\circ$  in the setup of this work), the fiber's effective point of measurement

along the full scan range for a dose depth scan along the beam central axis with 18, 12 and 6 MeV clinical electron beams is at depths of approximately 1.7, 0.8 and 0.1 cm, respectively, downstream from the fiber axis. This is the case when scan data sets are normalized to 1 at their respective maxima. The Pearson and Spearman correlation coefficients for the Cherenkov and dose data are both larger than 0.99. This result is supported by both simulation and experiment. The likely cause of the shift is directional selection of photons by the collecting fiber due to an acceptance angle in water of approximately  $9.5^\circ$  and the very high energies of electrons emitting detectable photons. Since the magnitude of the shift varies with beam energy, it is an effect attributable to both energy and detection geometry.

- Points less than  $\sim 1.5$  cm from the water surface in the experimental Cherenkov scan had higher values than expected, an effect attributed to reflection (not included in the simulation) from the water surface towards the fiber of a fraction of the emitted photons, resulting in their detection by the fiber. In support of this explanation is the fact that exclusion of these readings from the data set, followed by renormalisation to the new maximum, eliminates this issue and reveals the correlation with the dose scan. Further investigation into the source of this issue is necessary.
- For the simulated Cherenkov distribution, values at depths less than approximately 2 cm were lower than expected, most notably for points on the surface, as a result of variation of the fiber acceptance volume in water due to truncation by the water surface. Renormalizing the distribution to larger depths moderates this issue, but does not remove it entirely as the fiber acceptance volume still varies due to beam divergence. Acceptance volume effects must be taken into account in order to validate the calculated effective point of measurement for points in the build-up region.
- Spectral shift experiments were carried out with a front-illuminated CCD spectrometer, as well as a back-illuminated CCD spectrometer featuring deep thermoelectric cooling. The Cherenkov emission spectrum by an 18 MeV

clinical electron beam was successfully shifted towards the NIR window of tissue in a water tank and in a tissue-simulating phantom, composed of water, Intralipid® and bovine blood, using CdSe/ZnS core-shell quantum dots. These quantum dots are characterized by a continuous absorption spectrum in the blue/green region of the electromagnetic spectrum, decreasing for longer wavelengths, and an emission peak at 650 nm. With the front-illuminated CCD spectrometer, decreasing the field size along the fiber axis in the water tank experiments resulted in lower signal, as expected, no decrease in absorption, possibly due to saturation of the quantum dot absorption states, and a larger relative spectral shift, which is unexpected and may be a noise artifact or a result of the higher Cherenkov intensity in the red in the case of the larger field, yielding a smaller relative increase. Increasing the depth at which the quantum dots were positioned in the tissue-simulating phantom decreased the signal, as expected, though the shift was still discernible for a depth of 1 cm. The tissue phantom spectra were much more affected by noise than the water tank spectra due to higher absorption and scattering coefficients resulting in a lower SNR. With the back-illuminated cooled CCD spectrometer, a prominent shift was also observed in water and in a tissue-simulating phantom and, as is expected, the spectra were much less affected by noise.

- A detailed noise analysis revealed that spectrometer readings are unimodal and symmetric about the mean across all wavelengths and for single-pixel signal distribution, indicating that noise is white with respect to photon frequency and not positively/negatively biased. The distribution of pixel-position dependent beam-off noise is nearly uniform towards the centre and has heavy relatively uniform tails. Analysis of the beam-on noise at each pixel (i.e. wavelength) strongly supports the premise that radiation impacting the spectrometer causes fluctuations in the readings and that the signal is normally distributed if these fluctuations are removed. Shielding of the spectrometer alleviates this problem. Normality of the signal is expected due to the discrete nature of photons and electrons.

Optical detection equipment is readily available, relatively inexpensive and advanced, and optical detection techniques are non-ionizing and have been well characterized. Therefore, as supported by the results of this work, optical dosimetry and imaging procedures employing the Cherenkov effect promise to be highly beneficial in radiotherapy dosimetry and for beam-specific online imaging of dose deposition in tumors during radiation therapy.

The number of opportunities and pathways for future work in this field is endless. In the very near future, variation of the correlation with beam type (photons/electrons), energy, field size, dose rate, and other beam defining parameters can be studied, a lens or single-mode fiber may be incorporated into the setup to reduce the sensitive volume for Cherenkov detection, a quantitative study of the NIR shift of the Cherenkov spectrum can be performed, various wavelength-shifting species and schemes can be designed and optimized, and small-animal experiments can be conducted. In addition, a multi-channel spectrometer may be implemented for simultaneous acquisition of main, reference and background signals. In the more distant future, a permanent phantom can be designed for more robust measurements and the prospect of standardization of quality assurance procedures for Cherenkov dosimetry and imaging. Furthermore, quantitative techniques can be developed for extraction of tumor microenvironment information, such as oxygenation status. Ultimately, the much desired, and perhaps not so forbidden, fruit of this effort is implementation of three-dimensional dose mapping, online Cherenkov imaging and tumor localization, and beam modulation based on tumor molecular environment information as routine practices in clinical radiotherapy with the aim of taking control over one of the most lethal diseases to humankind.

## List of Abbreviations

2D, 3D, 4D – 2-, 3-, 4-dimensional

AAPM – American Association of Physicists in Medicine

CCD – charge coupled device

CE – Cherenkov emission

DNA – deoxyribonucleic acid

FDG – fluorodeoxyglucose

Gy – Gray

IGRT – image-guided radiotherapy

IMRT – intensity-modulated radiotherapy

kV – kilovolt

linac – linear accelerator

MC – Monte Carlo

MeV – mega electron-volt

MU – monitor unit

MV – megavolt

NA – numerical aperture

NIR – near-infrared

NTCP – normal tissue complication probability

PDD – percent depth dose

PET- positron emission tomography

PMMA – polymethyl methacrylate

PtG4 – platinum(II)-G4

Q-Q plots – quantile-quantile plot

QD – quantum dot

SNR – signal-to-noise ratio

SPECT - single-photon emission computed tomography

SRS - stereotactic radiosurgery

SSD – source-to-surface distance

TCP – tumor control probability

TG-51 – Task Group 51

UV – ultraviolet

$z_{\max}$  – depth of maximum dose

## Bibliography

- <sup>1</sup> American Cancer Society, in *The History of Cancer* (American Cancer Society, Atlanta, 2012), Vol. 2013.
- <sup>2</sup> D. Hanahan and R. A. Weinberg, *Cell* **144** (5), 646-674 (2011).
- <sup>3</sup> J. Ferlay, H. R. Shin, F. Bray, D. Forman, C. Mathers and D. M. Parkin, in *IARC CancerBase No. 10* (International Agency for Research on Cancer, Lyon, France, 2010).
- <sup>4</sup> Statistics Canada, in *Analysis Series, 2009 Census* (Statistics Canada, Ottawa, 2012).
- <sup>5</sup> American Cancer Society, in *Treatment Types* (American Cancer Society, Atlanta, 2012).
- <sup>6</sup> E. B. Podgorsak, *Radiation Oncology Physics: A Handbook for Teachers and Students*. (International Atomic Energy Agency, 2005).
- <sup>7</sup> P. J. Russell, *iGenetics: a molecular approach*, 2nd ed. (Pearson/Benjamin Cummings, San Francisco, 2006).
- <sup>8</sup> J. Wondergem, in *Radiation Biology: A Handbook for Teachers and Students* (International Atomic Energy Agency, Vienna, 2010), pp. 13-26.
- <sup>9</sup> J. L. Meyer, *IMRT, IGRT, SBRT: Advances in the Treatment Planning and Delivery of Radiotherapy*. (Karger Verlag, 2011).
- <sup>10</sup> P. R. Almond, P. J. Biggs, B. M. Coursey, W. F. Hanson, S. M. Huq, R. Nath and D. W. O. Rogers, *Med Phys* **26** (9) (1999).
- <sup>11</sup> J. Van Dyk, *The Modern Technology of Radiation Oncology: A Compendium for Medical Physicists and Radiation Oncologists*. (Medical Physics Publishing, Madison, WI, 1999).
- <sup>12</sup> International Commission on Radiation Units and Measurements, *Dose Specification for Reporting External Beam Therapy with Photons and Electrons*. (International Commission on Radiation Units and Measurements, Washington, DC, 1978).
- <sup>13</sup> A. Brahme, *Acta Radiol Oncol* **23** (5), 379-391 (1984).
- <sup>14</sup> R. D. Timmerman and L. Xing, *Image-guided and adaptive radiation therapy*. (Lippincott Williams & Wilkins, Philadelphia, 2010).

- <sup>15</sup> B. M. Bolotovskii, *Phys-Usp* **52** (11), 1161-1173 (2009).
- <sup>16</sup> J. V. Jelley, in *Čerenkov radiation, and its applications* (Pergamon Press, New York, 1958), pp. 1-78.
- <sup>17</sup> E. Hecht, *Optics*, 4th ed. (Addison-Wesley, Reading, MA, 2002).
- <sup>18</sup> P. Schiebener, J. Straub, J. M. H. L. Sengers and J. S. Gallagher, *J Phys Chem Ref Data* **19** (3), 677-717 (1990).
- <sup>19</sup> National Isotope Development Center, (National Isotope Development Center, Oak Ridge, TN), Vol. 2013.
- <sup>20</sup> A. Ruggiero, J. P. Holland and J. S. Lewis, Grimm J., *J Nucl Med* **51** (7), 1123-1130 (2010).
- <sup>21</sup> Bradley J. Beattie, Daniel L. J. Thorek, Charles R. Schmittlein, Keith S. Pentlow, John L. Humm and A. H. Hielscher, *PLoS ONE* **7** (2), e31402 (2012).
- <sup>22</sup> L. Hongguang, R. Gang, M. Zheng, Z. Xiaofen, T. Xiaodong, H. Peizhen, S. G. Sanjiv and C. Zhen, *PLoS ONE* **5** (3) (2010).
- <sup>23</sup> M. N. Wernick and J. N. Aarsvold, *Emission Tomography: The Fundamentals of PET and SPECT*, revised ed. (Elsevier Science, 2004).
- <sup>24</sup> D. L. Thorek, R. Robertson, W. A. Bacchus, J. Hahn, J. Rothberg, B. J. Beattie and J. Grimm, *Am J Nucl Med Mol Imaging* **2** (2), 163-173 (2012).
- <sup>25</sup> J. P. Holland, G. Normand, A. Ruggiero, J. S. Lewis and J. Grimm, *Mol Imaging* **10** (3), 177-186, 171-173 (2011).
- <sup>26</sup> R. S. Dothager, R. J. Goiffon, E. Jackson, S. Harpstrite and D. Piwnica-Worms, *PLoS ONE* **5** (10), e13300 (2010).
- <sup>27</sup> H. Liu, X. Zhang, B. Xing, P. Han, S. S. Gambhir and Z. Cheng, *Small* (Weinheim an der Bergstrasse, Germany) **6** (10), 1087-1091 (2010).
- <sup>28</sup> C. Ran, Z. Zhang, J. Hooker and A. Moore, *Mol Imaging Biol* **14** (2), 156-162 (2012).
- <sup>29</sup> J. Axelsson, S. C. Davis, D. J. Gladstone and B. W. Pogue, *Med Phys* **38** (7), 4127-4132 (2011).
- <sup>30</sup> J. Axelsson, A. K. Glaser, D. J. Gladstone and B. W. Pogue, *Opt Express* **20** (5), 5133-5142 (2012).

- <sup>31</sup> A. K. Glaser, R. Zhang, S. C. Davis, D. J. Gladstone and B. W. Pogue, *Opt Lett* **37** (7), 1193-1195 (2012).
- <sup>32</sup> A. K. Glaser, S. C. Davis, D. M. McClatchy, R. Zhang, B. W. Pogue and D. J. Gladstone, *Med Phys* **40** (1), 012101 (2013).
- <sup>33</sup> A. K. Glaser, S. C. Davis, W. H. Voigt, R. Zhang, B. W. Pogue and D. J. Gladstone, *Phys Med Biol* **58** (3), 601-619 (2013).
- <sup>34</sup> A. K. Glaser, W. H. Voigt, S. C. Davis, R. Zhang, D. J. Gladstone and B. W. Pogue, *Opt Lett* **38** (5), 634-636 (2013).
- <sup>35</sup> R. Zhang, A. Glaser, T. V. Esipova, S. C. Kanick, S. C. Davis, S. Vinogradov, D. Gladstone and B. W. Pogue, *Biomed Opt Express* **3** (10), 2381-2394 (2012).
- <sup>36</sup> R. Zhang, S. C. Davis, J. L. Demers, A. K. Glaser, D. J. Gladstone, T. V. Esipova, S. A. Vinogradov and B. W. Pogue, *J Biomed Opt* **18** (5), 50503 (2013).
- <sup>37</sup> J.-L. Demers, S. C. Davis, R. Zhang, D. J. Gladstone and B. W. Pogue, *Opt Lett* **38** (8), 1364-1366 (2013).
- <sup>38</sup> D. Bera, L. Qian, T.-K. Tseng and P. H. Holloway, *Materials* **3** (4), 2260-2345 (2010).
- <sup>39</sup> M. Bruchez, M. Moronne, P. Gin, S. Weiss and A. P. Alivisatos, *Science* **281** (5385), 2013-2016 (1998).
- <sup>40</sup> W. C. W. Chan and S. Nie, *Science* **281** (5385), 2016-2018 (1998).
- <sup>41</sup> G. S. Mitchell, R. K. Gill, D. L. Boucher, C. Li and S. R. Cherry, *Phil Trans R Soc A* **369** (1955), 4605-4619 (2011).
- <sup>42</sup> C. Balas, *Meas Sci Technol* **20** (10), 104020 (2009).
- <sup>43</sup> S. L. Jacques, *Phys Med Biol* **58** (11), R37 (2013).
- <sup>44</sup> R. Weissleder, *Nat Biotechnol* **19** (4), 316-317 (2001).
- <sup>45</sup> W. L. Wolfe, *Introduction to Imaging Spectrometers*. (SPIE Optical Engineering Press, Bellingham, WA, 1997).
- <sup>46</sup> S. Svanberg, *Atomic and Molecular Spectroscopy: Basic Aspects and Practical Applications*, 4th ed. (Springer Verlag, Heidelberg, Germany, 2004).

- <sup>47</sup> C. Palmer, *Diffraction Grating Handbook*, 6th ed. (Newport Corporation, Rochester, NY, 2005).
- <sup>48</sup> P. Griffiths and J. A. De Haseth, *Fourier Transform Infrared Spectrometry*, 2nd ed. (John Wiley & Sons, Hoboken, NJ, 2007).
- <sup>49</sup> J. R. Janesick, *Scientific Charge-Coupled Devices*. (SPIE Press, Bellingham, WA, 2001).
- <sup>50</sup> B. Dörband, H. Müller and H. Gross, in *Metrology of Optical Components and Systems* (Wiley-VCH, Weinheim, Germany, 2012), pp. 162-163.
- <sup>51</sup> L. Thévenaz, in *Advanced Fiber Optics* (EPFL Press, Boca Raton, FL, 2011), pp. 1-12.
- <sup>52</sup> F. Mitschke, in *Fiber Optics: Physics and Technology* (Springer Berlin Heidelberg, Heidelberg, Germany, 2009), pp. 8.
- <sup>53</sup> I. Frank and I. Tamm, in *Selected Papers*, edited by B. Bolotovskii, V. Frenkel and R. Peierls (Springer, 1991), pp. 29-35.
- <sup>54</sup> N. O'Farrell, A. Houlton and B. R. Horrocks, *Int J Nanomedicine* **1** (4), 451-472 (2006).
- <sup>55</sup> J. F. Geisz and D. J. Friedman, *Semicond Sci Technol* **17** (8), 769-777 (2002).
- <sup>56</sup> R. E. Caflisch, *Acta Numerica* **7**, 1-49 (1998).
- <sup>57</sup> D. E. Raeside, *Phys Med Biol* **21** (2), 181-197 (1976).
- <sup>58</sup> D. W. O. Rogers, *Phys Med Biol* **51** (13), R287 (2006).
- <sup>59</sup> I. Kawrakow, *Med Phys* **27** (3), 485-498 (2000).
- <sup>60</sup> I. Kawrakow, *Med Phys* **27** (3), 499-513 (2000).
- <sup>61</sup> J. Baró, J. Sempau, J. M. Fernández-Varea and F. Salvat, *Nucl Instrum Methods B* **100** (1), 31-46 (1995).
- <sup>62</sup> M. J. T. Goorley, T. Booth, F. Brown, J. Bull, L. J. Cox, J. Durkee, J. Elson, M. Fensin, R. A. Forster, J. Hendricks, H. G. Hughes, R. Johns, B. Kiedrowski, R. Martz, S. Mashnik, G. McKinney, D. Pelowitz, R. Prael, J. Sweezy, L. Waters, T. Wilcox, T. Zukaitis, *Nucl Technol* **180** (3), 298-315 (2012).
- <sup>63</sup> S. Agostinelli, J. Allison, K. Amako, J. Apostolakis, H. Araujo, P. Arce, M. Asai, D. Axen, S. Banerjee, G. Barrand, F. Behner, L. Bellagamba, J.

Boudreau, L. Broglia, A. Brunengo, H. Burkhardt, S. Chauvie, J. Chuma, R. Chytraccek, G. Cooperman, G. Cosmo, P. Degtyarenko, A. Dell'Acqua, G. Depaola, D. Dietrich, R. Enami, A. Feliciello, C. Ferguson, H. Fesefeldt, G. Folger, F. Foppiano, A. Forti, S. Garelli, S. Giani, R. Giannitrapani, D. Gibin, J. J. Gómez Cadenas, I. González, G. Gracia Abril, G. Greeniaus, W. Greiner, V. Grichine, A. Grossheim, S. Guatelli, P. Gumplinger, R. Hamatsu, K. Hashimoto, H. Hasui, A. Heikkinen, A. Howard, V. Ivanchenko, A. Johnson, F. W. Jones, J. Kallenbach, N. Kanaya, M. Kawabata, Y. Kawabata, M. Kawaguti, S. Kelner, P. Kent, A. Kimura, T. Kodama, R. Kokoulin, M. Kossov, H. Kurashige, E. Lamanna, T. Lampén, V. Lara, V. Lefebure, F. Lei, M. Liendl, W. Lockman, F. Longo, S. Magni, M. Maire, E. Medernach, K. Minamimoto, P. Mora de Freitas, Y. Morita, K. Murakami, M. Nagamatu, R. Nartallo, P. Nieminen, T. Nishimura, K. Ohtsubo, M. Okamura, S. O'Neale, Y. Oohata, K. Paech, J. Perl, A. Pfeiffer, M. G. Pia, F. Ranjard, A. Rybin, S. Sadilov, E. Di Salvo, G. Santin, T. Sasaki, N. Savvas, Y. Sawada, S. Scherer, S. Sei, V. Sirotenko, D. Smith, N. Starkov, H. Stoecker, J. Sulkimo, M. Takahata, S. Tanaka, E. Tcherniaev, E. Safai Tehrani, M. Tropeano, P. Truscott, H. Uno, L. Urban, P. Urban, M. Verderi, A. Walkden, W. Wander, H. Weber, J. P. Wellisch, T. Wenaus, D. C. Williams, D. Wright, T. Yamada, H. Yoshida and D. Zschesche, *Nucl Instrum Methods A* **506** (3), 250-303 (2003).

<sup>64</sup> I. J. Chetty, B. Curran, J. E. Cygler, J. J. DeMarco, G. Ezzell, B. A. Faddegon, I. Kawrakow, P. J. Keall, H. Liu, C. M. Ma, D. W. Rogers, J. Seuntjens, D. Sheikh-Bagheri and J. V. Siebers, *Med Phys* **34** (12), 4818-4853 (2007).

<sup>65</sup> G. R. Norman and D. L. Streiner, in *Biostatistics: The Bare Essentials* (B.C. Decker, Hamilton, ON, 2008), pp. 20-25, 31-36.

<sup>66</sup> T. C. Urdan, in *Statistics in Plain English* (Taylor & Francis Group, 2010), pp. 29-32, 79-92.

<sup>67</sup> D. J. Sheskin, in *Handbook of Parametric and Nonparametric Statistical Procedures* (Taylor & Francis, 2003), pp. 42-44.

- <sup>68</sup> I. E. Frank and R. Todeschini, in *The Data Analysis Handbook* (Elsevier Science, Amsterdam, Netherlands, 1994), pp. 262-264.
- <sup>69</sup> R. M. Heiberger and B. Holland, in *Statistical Analysis and Data Display: An Intermediate Course with Examples in S-PLUS, R, and SAS* (Springer, New York, NY, 2004), pp. 110-116.
- <sup>70</sup> B. W. Pogue and M. S. Patterson, *J Biomed Opt* **11** (4), 041102 (2006).